Diploma-Thesis

Combustion Characteristics of Hydrogen- and Hydrocarbon-Air Mixtures in Closed Vessels

Diplomarbeit von
cand.-aer. Oliver Kunz
Matr.Nr.: 1645477

Universität Stuttgart
Fakultät für Luft- und Raumfahrttechnik
Institut für Thermodynamik der Luft- und Raumfahrt
70550 Stuttgart, Germany

Graduate Aeronautical Laboratories
California Institute of Technology
Pasadena, CA 91125, USA

March 1998

Advisors:

Dr.-Ing. U. Pfahl (Caltech)
Prof. Dr. J. E. Shepherd (Caltech)
Prof. Dr.-Ing. D. Brüggemann (Universität Stuttgart)

Explosion Dynamics Laboratory Report FM98-4

Acknowledgments

I would like to thank Prof. Hans Hornung for allowing me to perform my diploma-thesis at the Graduate Aeronautical Laboratories, California Institute of Technology in Pasadena.

Prof. Joseph E. Shepherd as the responsible professor receives my sincere thanks for hosting me at the Explosion Dynamics Laboratory. Despite his busy schedule, his supervision of my work was excellent.

My very particular thanks are dedicated to Dr. Ulrich Pfahl. His supervision of my diploma-thesis was outstanding. I greatly appreciated and enjoyed working together with him. His spontaneous willingness to solve any kind of problem was incredible. His help, tips, and suggestions were countless and always appreciated. His dedication to both experimental work and analysis tremendously influenced the continuous progress of this diploma-thesis.

I want to express my thanks to the whole Explosion Dynamics Group for the good working climate and the support of my work. I very much appreciated working within this group.

Furthermore, I would like to thank the Prof. Dr.-Ing. Erich Müller-Stiftung (Stifterverband für die Deutsche Wissenschaft), the Walther Blohm Stiftung (Daimler-Benz Aerospace Airbus AG), and the Stuttgarter Studentenwerk e.V. for their support and generous financial contributions. Without their funding the realization of this diploma-thesis would not have been possible.

Contents

List of Figures

List of Tables

1 Introduction

This report describes a series of experiments and analyses on combustion characteristics of hydrogen- and hydrocarbon-air mixtures as well as on the flammability of Jet A (aviation kerosene) in air. The experiments are carried out at the Explosion Dynamics Laboratories of the California Institute of Technology. The report is written as an diploma-thesis for the Department of Aeronautics and Space Engineering at the University of Stuttgart, Germany.

It is organized as follows:

The first part deals with combustion pressure analysis of hydrogen-, methane-, ethane- and propane-air mixtures. The objective is to develop a characteristic parameter for closed vessel combustion which enables the prediction of the maximum pressure rise rate.

Vessels with volumes of 1.84, 11.25, 407, and 1180 liters are used for the experiments. The equivalence ratios of the mixtures range from 0.24 to 0.93 for hydrogen and from 0.65 to 1.0 for the hydrocarbon fuels. The mixtures are ignited by an electrical spark. Pressure traces and peak pressures are measured during combustion. The pressure time derivative is used to calculate the pressure rise coefficient K_g. The results are compared to previous work from NFPA68 (1994). Further analyses on the pressure histories are performed and laminar burning velocities are calculated by using a spherical flame model. A dimensionless pressure rise coefficient, K'_g, is defined to characterize the maximum rate of pressure rise during an isochoric combustion process.

The second part of the diploma-thesis deals with ignition energy measurements of various Jet A-air and Jet A simulant-air mixtures under certain initial conditions.

The flammability of a propane/hydrogen fuel, which serves as a Jet A simulant, is examined. Ignition energies of several samples of weathered Jet A are determined and compared to existing data for fresh Jet A. The study supported field tests related to the TWA800 accident investigations and examined the influence of fuel weathering on ignition energy.

2 Fundamental Theory of Gaseous Combustion

2.1 Ideal Gas Relation

The gases studied in this investigation are governed by the ideal gas relation:

$$pV = n\Re T = \frac{m}{M}\Re T = mRT \qquad\qquad R = \frac{\Re}{T} \tag{1}$$

While the volume V and universal gas constant $\Re$ have constant values, the pressure p, the temperature T, and the number of moles n are subject to change during combustion. The chemical reaction can be characterized as an exothermal transformation of the reactants (fuel in liquid or gaseous phase) to the various products, also in liquid or gaseous phase. Assuming a complete combustion, the final pressure can be calculated by using the number of moles after the combustion which is known by the overall reaction balances discussed below.

2.2 Flame Initiation

In order to to start a combustion process, it is necessary to have a fuel and an oxidizer that form a combustible mixture. The complete combustion of methane with air is used to demonstrate one overall reaction model used in this study. Note that one mole of air is approximated as 0.21 O_2 + 0.79 N_2.

$$\alpha\, CH_4 + \beta\, O_2 + 3.76\,\beta\, N_2 \longrightarrow \alpha\, CO_2 + 2\alpha\, H_2O + (\beta - 2\alpha\,)O_2 + 3.76\beta\, N_2 \tag{2}$$

Both reactants are assumed to be in the gaseous phase. If a liquid fuel or oxidizer is present, the process consists of the evaporation of the liquid followed by an exothermic vapor-phase reaction. The time-dependent process of starting with the reactants and evolving in time towards a burning flame is called ignition. This process can be induced by several different ways. The most common ways are spontaneous ignition of a hot mixture and ignition by external means, such as a spark.

Spontaneous Ignition

Intensive studies of the spontaneous ignition phenomena have been carried out since Semenov's seminal studies in the late 1920's (Semenov 1928). The basic idea is that the heat exchange in the reaction system is fast in comparison to the heat exchange with the surrounding boundary. The process of autoignition can be initiated by hot surfaces at the boundaries of the combustible mixture or by an adiabatic compression of the combustible reactants.

Ignition by External Means

External ignition of a flammable mixture can be achieved in a number of ways, e.g., by a spark, a hot wire, or another flame. During the process of ignition a small volume of the mixture is typically brought to a high temperature. A sufficiently high temperature induces reaction in this volume and a flame subsequently begins propagating through the unburned mixture. The minimum energy needed to locally ignite a combustible mixture is called the Minimum Ignition Energy (MIE). At atmospheric pressure, hydrocarbon-air mixtures have MIE's of about 0.2 to 0.3 mJ while hydrogen-air mixtures only require about 0.065 mJ (Lewis and von Elbe 1961). The smallest value of the MIE typically does not occur for the stoichiometric composition but rather for a slightly rich mixture. The larger the molecular mass, the richer the mixture at which the smallest value of MIE is found (Gaydon and Wolfhard 1970). For lean mixtures, the MIE increases with decreasing equivalence ratio (Ronney 1985).

Classical results on ignition energy by Lewis and von Elbe (1961) can be seen in Fig. 1. For the combustion pressure analysis experiments carried out here, ignition energies are much higher than the required minimum. In Chapter 5.2, the ignition energy for several different fuels and initial conditions are presented. Further information on this topic is available in Shepherd et al. (1998).

2.3 Flame Propagation

In general, flames can be separated in two different categories. On the one hand, there are the stationary or steady-state flames such as the Bunsen burner flame. Characteristic values of pressure or temperature do not change with time. On a small scale, the combustion process is mainly determined by the rate of inter-diffusion of fuel and oxidizer. In

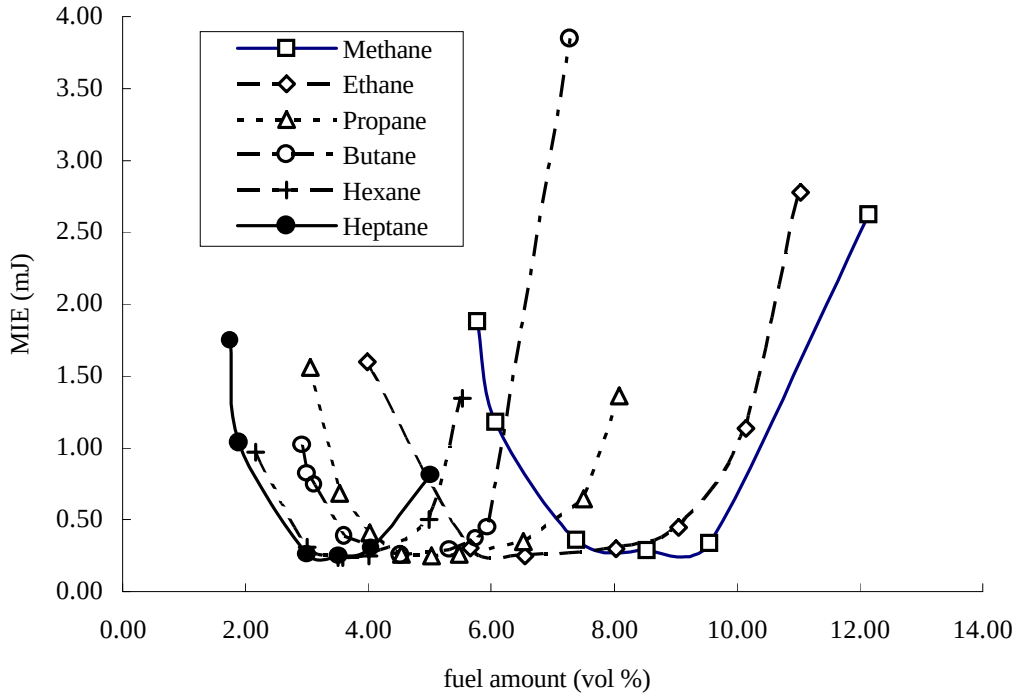

Figure 1: Minimum ignition energies at 1 bar and 295 K, Lewis and von Elbe (1961).

larger flames of this type, mixing is primarily caused due to turbulence and gas motion with diffusion occurring at the smallest scales.

On the other hand, there are the propagating flames or explosions. These flames are nonsteady and are always associated with the movement of gases. The most important application of the closed-vessel explosion is the Otto internal-combustion engine. From the point of ignition in an arbitrary vessel, a flame generally propagates uniformly in every direction. The shape of the flame is thus spherical at early times. Later the flow assumes the shape of the vessel. In the very beginning, the flame proceeds with fairly uniform speed, which is determined by the fundamental burning speed, the flame area, and the expansion ratio of the gas due to the combustion. As the flame proceeds, this gas expansion thrusts the flame forward. With increasing flame speed or distance from the ignition point, turbulence may occur and disturb the spherical flame shape. Turbulence results in an increase of flame front surface and thus in a larger overall reaction rate. Depending on the size of the vessel, the flame may reach very high speeds. In this case, it is possible that the moving burned gas has a piston-like influence on the unburnt part of the gas. A resulting pressure pulse may then sharpen up to a shock wave. If this shock wave is strong enough, the temperature behind the shock front can be high enough

to cause a rapid chemical reaction and a detonation may be formed. A shock wave then propagates ahead of the flame front and can travel at speeds of up to 3000 m/s. Intensive studies in this field have been carried out by Lewis and von Elbe (1961). Early studies of flame propagation in tubes were performed by Mallard and Chatelier (1883) in their pioneer studies on flame and combustion. In the present study, the investigated combustion phenomena never come close to the point where the explosion evolves into a detonation. A discrete combustion wave that travels subsonically is termed a deflagration.

2.3.1 Continuity Equation and Speed Definitions

The continuity equation (mass conservation) is one of the fundamental conservation equations, the others being the conservation of momentum and of energy. The continuity equation is used to relate the velocities before and after the flame. In the following the index 'u' defines the unburned state while 'b' represents the burned state. Although we consider the flame to have a spherical shape, the flame front appears to be planar on a sufficiently small scale. Figure 2 shows a planar flame propagating from the left to the right side. The flame front symbolized by the vertical line travels with the "flame speed" V_f into the unburned gas to its right.

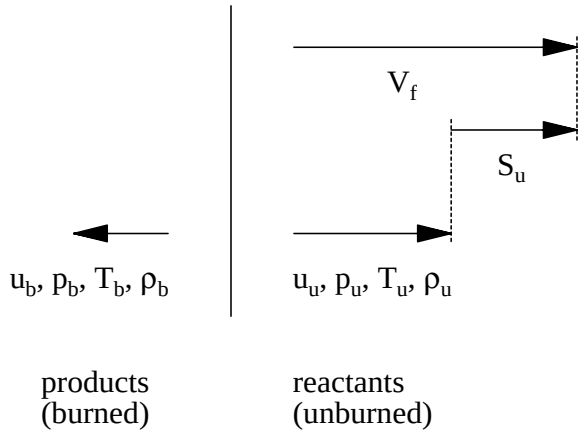

Figure 2: Planar flame front and speed definitions.

The conservation of mass implies the following relation for steady one-dimensional flows:

$$\rho_u(V_f - u_u) = \rho_b(V_f - u_b). \tag{3}$$

The laminar burning speed, S_u, is defined as the difference between the flame speed V_f

and the fluid speed u_u:

$$S_u = V_f - u_u. \tag{4}$$

The flame speed V_f is the speed of the flame front measured by an outside observer. The speed, u_u, of the flow is caused by the expansion of the product gases ($\rho_u > \rho_b$) and motion due to buoyancy. The laminar burning speed, S_u, is the speed at which the reaction zone propagates normal to its surface relative to the unburned gas of the flammable mixture, which is a fundamental property of the gas mixture. The laminar burning speed of a gas primarily depends upon the mixture's thermal diffusivity, reaction mechanism, and heat of combustion. Typical values (assuming atmospheric pressure and room temperature) for S_u range from 10 to 50 cm/s for hydrocarbon-air mixtures and from 5 to 350 cm/s for hydrogen-air mixtures (see Fig. 3). Even lower values are possible for very small equivalence ratios.

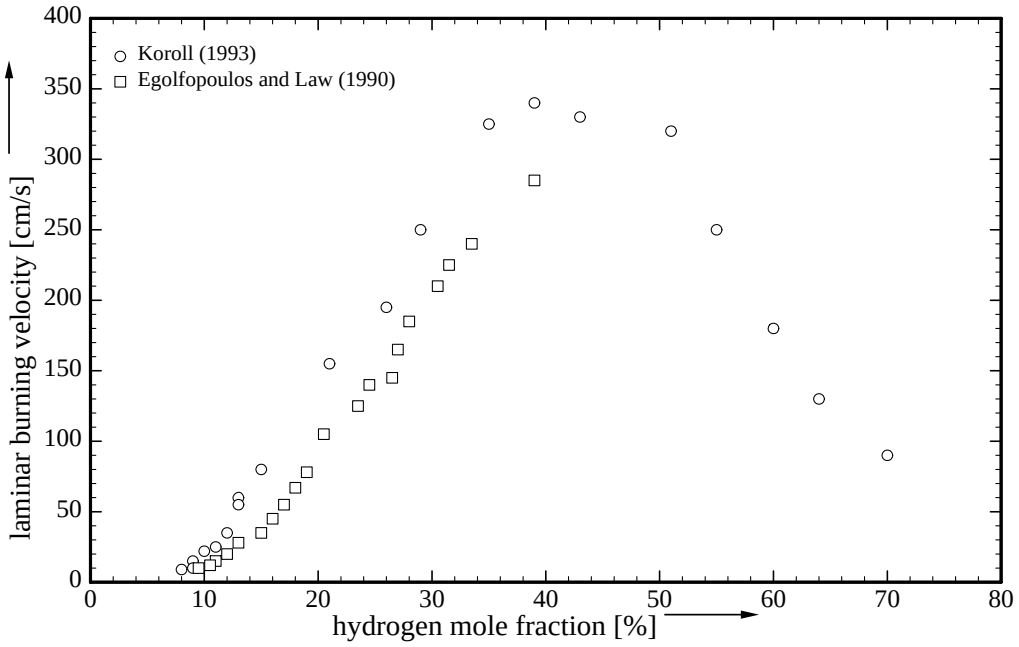

Figure 3: Laminar burning speed S_u for hydrogen air mixtures (Koroll et al. 1993; Egolfopoulos and Law 1990) at initial conditions of 1 bar and 295 K.

Values of S_u have been measured and published for many types of gases, different initial temperatures and pressures, as well as for various vessel volumes: 1.39 liters (Metghalchi and Keck 1980), 11 liters (Raman 1997 and Kwon et al. 1992), 17 liters (Koroll et al. 1993).

2.3.2 Reynolds Number

An important parameter used to describe aerodynamic flows is the dimensionless Reynolds number, Re, which can be used to characterize a flow phenomena as laminar or turbulent. In general, the higher the Reynolds number, the more likely turbulence is to occur. Reynolds number can also be used as a basis to compare flows. The Reynolds number for a propagating flame can be defined as

$$Re = \frac{\rho_u \; S_u \; L}{\mu} = \frac{S_u \; L}{\nu}, \tag{5}$$

where ρ_u, μ, and ν are the density, viscosity, and kinematic viscosity of the reactants, S_u, the laminar burning speed, and L,

In this study, the mean density of the reactants and the mean viscosity of the unburned mixture are calculated with CHEMKIN (see Kee et al. 1989). As far as the speed is concerned, the experimental results for the laminar burning speed S_u are used. Usually the cube root of the vessel volume, V, is chosen as the characteristic length. As the experiments are done not only in vessels of different volumes but also of different geometry, the choice of $V^{\frac{1}{3}}$ as characteristic length is not obvious. Another possible characteristic length is the distance l_{max} from the point of ignition to the farthest corner of the combustion vessel. This choice incorporates some of the differences associated with vessel shapes. To have consistency with other reports, $V^{\frac{1}{3}}$ is chosen as characteristic length in this study and l_{max} is mentioned briefly only to compare results.

Using the different vessels described below, the Reynolds numbers range from about 700 to 2×10^5. With increasing Reynolds number, the flow conditions change from laminar to turbulent. As an example this transition occurs between Re = 2300-3200 for flow in pipes. Although these numbers do not apply to flame propagation, a similar transition is expected to occur.

The flame in a spark-ignited mixture has an approximately spherical shape just after ignition. Within the first phase (length of the period depends strongly on gas composition and initial conditions) of the deflagration, the flame-bubble gains in size homogeneously in all directions. At this time, the Reynolds numbers range from 700 to 10^4 depending on vessel and mixture. After a certain time (between 20 to 50 milliseconds) distortions appear, the flame is no longer spherical and develops into a turbulent flame. As this work primarily deals with the laminar expansion of flames, this transition and turbulent phase are not investigated. Many experimental and computational studies have been carried

out on turbulent flame propagation. Further information on this topic can be found in Kwon et al. (1992) and Koroll et al. (1993).

2.4 Chemical Equilibrium

The reactants in the investigated combustible mixtures are metastable and thus not in a state of chemical equilibrium. The flame causes a rapid transformation from reactants to products. The chemical reaction itself is regarded as a "black box". Only reactants and products exist in this perspective; there are no stages in between. When only a small quantity of gas burns, the pressure changes only slightly, and the equilibrium condition behind the flame is constrained to be at constant enthalpy and pressure. This is known as constant pressure combustion. When an entire volume of gas inside a closed vessel burns, it does so by a sequence of constant-pressure burns at increasing pressure. The final pressure at the end of burning all the gas in the volume can be computed by using the constraint of equilibrium at constant volume and energy. In general, products exist in a state of equilibrium which can be calculated by minimizing the free energy of the mixture under the appropriate constraints.

In this report, all peak pressures during combustion are calculated using the chemical equilibrium program STANJAN. STANJAN was developed by Reynolds (1986) and is based on the JANNAF thermochemistry data and the minimization of Gibbs energy. It calculates maximum pressure, maximum temperature, mean mass densities of reactants and products, and other thermodynamic key data for a given gas mixture and initial conditions. In the mode used for this investigation, energy losses due to radiation, conduction or convection are neglected, constant volume explosion and a complete chemical reaction are assumed. Thus the STANJAN output represents an adiabatic, isochoric, complete combustion (AICC) calculation. Due to these assumptions, the calculated values for pressure and temperature are always higher than the measured experimental peak values.

Energy Losses

Three sources of energy losses have to be considered in vessel explosions:

1. Thermal convection
2. Thermal conduction
3. Thermal radiation

Thermal Convection Due to the transient nature of deflagrations and natural decay of the induced fluid speed, different modes of convective heat transfer are important at different times. Initially, the velocities and turbulent intensities caused by the buoyant rise of the growing fireball and the flame flow field interactions are quite large compared to typical natural convection velocities. Immediately after the burn, the speed begins to decay due to dissipation within the fluid and at the walls. Eventually, the heat transfer process will become dominated by either forced convection (if fans are operating) or natural convection (as in this study). In general, the convective heat flux, q_{conv}, is determined from an engineering correlation for the heat transfer coefficient, h,

$$q_{conv} = h\ (T_g\ -\ T_w), \tag{6}$$

where T_g and T_w are the average gas and wall temperature, respectively. Typical values for h are calculated for each of the different modes of convection and the highest value is used. While this may appear to be arbitrary, it serves to define the crossover time between transient and forced or natural convection. Details on these particular forms of convection can be found in Shepherd and Ratzel (1985).

Thermal Conduction Thermal conduction in a fluid is explained by the transfer of energy due to molecular action between the molecules of different average kinetic energy or temperature. Molecular motion is the main mechanism of energy transfer for diluted gases; intermolecular action is the main mechanism for dense gases and liquids. between the high-temperature combustion products and the cold wall molecules of the combustion tank.

$$q_{cond} = -\ \lambda\ \frac{\partial T}{\partial x_i}, \tag{7}$$

where q_{cond} is the conductive heat flux, λ, the thermal conductivity, and $\frac{\partial T}{\partial x_i}$, the temperature gradient in the direction i. The value of this loss strongly depends on the geometry of the vessel and the ratio of internal surface-to-volume. The smaller this ratio, the smaller the energy loss. Consequently spherical bomb vessels are best to minimize these types of energy loss. In this study, thermal conduction is an important energy loss during the cool-down period of the products.

In addition to the thermal conduction, another energy flux results from the diffusion of various species with different specific enthalpies. Another flux (due to the Dufour effect) arises as a result of the coupled effect between mass and energy transfers. This same coupled effect accounts for the diffusional mass flux due to the temperature gradient (known as thermal diffusion or Sorret effect). This effect has a particular influence on low temperature flames with light fuels (e.g., hydrogen).

Thermal Radiation Radiation is very significant during the cooling process after the explosion for both fast and slow burning flames. Especially for slow burning flames with high temperatures, (e.g., lean hydrocarbon-air mixtures) the energy loss due to radiation is considerable. The radiative heat flux, q_{rad}, follows the Stefan-Bolzmann law:

$$q_{rad} \propto \sigma\ T^4\ =\ 5.67 \times 10^{-12}\ \times\ T^4 \qquad [\text{watts/cm}^2]\ . \tag{8}$$

Slow-burning hydrocarbon flames with temperatures of more than 2000 K consequently have larger radiation loss than comparable hydrogen flames with temperatures of about 1200 K. For further information on energy losses and transport phenomena see Lewis and von Elbe (1961), Hirschfelder et al. (1954), and Shepherd and Ratzel (1985).

Overall Reaction Models

The overall reaction in Eqn. 2 (full consumption of CH_4) corresponds to complete reaction to major products. The equilibrium thermodynamic estimates by STANJAN (Reynolds 1986) use a full set of product species (C, CH, CH_2, CH_2O, CH_2OH, CH_3, CH_3O, CH_4, CO, CO_2, C_2H, C_2H_2, C_2H_6, C_3H_8, C_4H_{10}, C_8H_{16}, H, CHCO, HO, HO_2, H_2,H_2O, H_2O_2, N, NO, NO_2, N_2, O, O_2) and appropriate thermodynamics.

2.5 Pressure Rise

2.5.1 Pressure Trace

The main thermodynamic parameters in closed vessel combustion can be seen in Fig. 4.

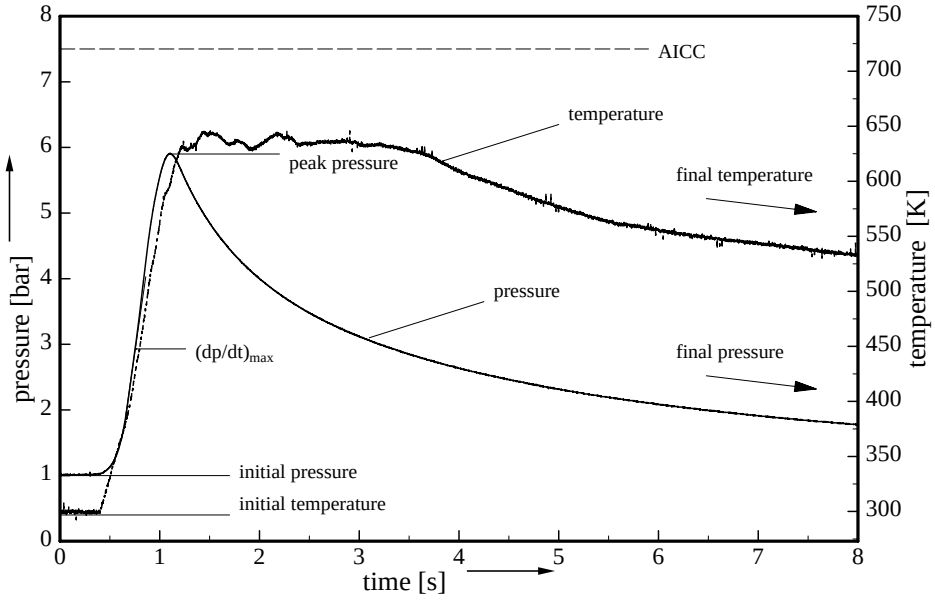

Figure 4: Main thermodynamic parameters in closed vessel combustion.

This figure shows the pressure and temperature history of a methane-air combustion with an equivalence ratio of $\phi = 0.7$ in Convol. Before the combustion takes place, the initial pressure in Fig. 4 is about 1 bar, and the initial temperature is about 295 K.

Since the figure shows only the first eight seconds, the final conditions are not yet reached. Symbolized by the arrows, both temperature and pressure will decrease. The final pressure in many experiments is lower than the initial pressure due to the chemical reaction. This pressure decrease is particularly true for reactions where H_2O is one major product. The final pressure for the combustion described by Fig. 4 is about 10 kPa lower than the initial pressure. The pressure decrease for comparable hydrogen-air mixtures is about 20 kPa. Note that experimental pressure differences are expected to be higher due to the different types of energy losses described in Chapter 2.4.

The maximum pressure during the combustion is termed the experimental peak pressure. Due to the different forms of energy losses (see Chapter 2.4), this pressure is always below the adiabatic, isochoric, complete combustion (AICC) pressure, symbolized by the

dashed line. Differences between the AICC pressure and the peak pressure can be used to roughly determine the amount of energy lost in combustion.

The steepest rate-of-increase of pressure is termed the maximum pressure time derivative, $(dp/dt)_{max}$. The value of this derivative depends on the composition of the gas, the initial conditions, and the vessel.

2.5.2 Pressure Rise Coefficient

A characteristic value to describe closed vessel combustion is the pressure rise coefficient, K_g. This coefficient is a common parameter used to evaluate the explosivity of a mixture (NFPA68 1994) and provides a means to compare the maximum rates of pressure rise for different gases. This classical definition of the pressure rise coefficient is limited by the fact that tests should be performed in vessels of similar geometry and volume, with the same kind of igniter and consistent ignition energy. The maximum rate of pressure rise $(dp/dt)_{max}$ is obtained by numerical differentiation of the combustion pressure trace. K_g is obtained by multiplying this maximum rate of pressure rise with a characteristic length like the cube root of the test vessel volume V. Thus the pressure rise coefficient, K_g, is defined as

$$K_g \equiv \left(\frac{dp}{dt}\right)_{max} V^{\frac{1}{3}} \qquad \text{[bar m/s]} \; . \tag{9}$$

The K_g values of different gases and for a range of vessel volumes have been experimentally investigated and tabulated in NFPA68 (1994). For that report, vessels of 5, 27, 200, 1080, and 38000 liters were used. All vessels have a spherical shape and a centrally-located ignition point.

2.5.3 Evaluation of Pressure Histories

The following section deals with some basic relations for the pressure trace analysis. The text summarizes page 26 to 35 in Shepherd et al. (1997a). A simple model for combustion phenomena in closed vessels is introduced.

The fundamental basis for all simple models is conservation of energy for an adiabatic, constant volume system: E = constant. Energy conservation provides a unique relationship between the average pressure, P, and the amount of burned gas, M_b. For

an ideal gas with a constant ratio of specific heats, γ, and specific heat of combustion, q, this relationship is

$$E = \frac{pV}{\gamma - 1} - M_b q, \tag{10}$$

where V is the total volume of the vessel. The peak pressure, P_m, is obtained when all of the gas is burned $M_b = M_\circ = \rho_\circ V$.

$$\Delta p_{max} = p_{max} - p_\circ = (\gamma - 1)\frac{qM_\circ}{V}. \tag{11}$$

The constancy of the energy E leads to the following ordinary differential equation for pressure:

$$\frac{dp}{dt} = \Delta p_{max}\frac{1}{M_\circ}\frac{dM_b}{dt}. \tag{12}$$

The rate at which gas is being burned can be computed by considering the flame as having an area $A_f(t)$ which is consuming unburned gas of density ρ_u with a laminar burning speed of S_u.

$$\frac{dM_b}{dt} = A_f \rho_u S_u. \tag{13}$$

If the effects of heat transfer during the burn are neglected, the unburned gases are spatially uniform and conditions can be predicted by using the isentropic relationships

$$T_u = T_\circ \left(\frac{p}{p_\circ}\right)^{\frac{\gamma-1}{\gamma}} \qquad \text{and} \qquad \rho_u = \rho_\circ \left(\frac{p}{p_\circ}\right)^{\frac{1}{\gamma}}. \tag{14}$$

For a given fuel concentration, the flame speed is dependent on both temperature and pressure. For the purposes of engineering studies, the dependence is usually taken to be (Gaydon and Wolfhard 1970)

$$S_u = S_u^o \left(\frac{p}{P_\circ}\right)^n \left(\frac{T}{T_\circ}\right)^2, \tag{15}$$

where the parameter n is substance specific.

Flame speed is also known to be a function of the the fluid motion (strain rate) but this is beyond the present considerations. The laminar flame speed at standard conditions is a function of the fuel concentration and must be determined experimentally, along with the exponent n.

Given a suitable expression for flame speed, the key remaining issue is the flame area dependence on time, $A_f(t)$. An expression for flame area requires experimental data or simplifying assumptions about the shape of the flame. However, before considering specific cases, the pressure equation can be reduced to a form that clearly indicates the key parameters:

$$\frac{dp}{dt} = \frac{S_u^\circ \Delta p_{max}}{V^{1/3}} \frac{S_u}{S_u^\circ} \frac{\rho_u}{\rho_\circ} \frac{A_f(t)}{V^{2/3}}. \tag{16}$$

From this equation, we infer that a characteristic value (such as the maximum) of the pressure time derivative must scale as

$$\left(\frac{dp}{dt}\right)_{max} \propto \frac{S_u^\circ \Delta p_{max}}{V^{1/3}}. \tag{17}$$

Based on this notion, the conventional way (NFPA68 1994) to analyze explosion pressure traces is to compute a pressure rise coefficient, K_g, as we will see in 5.1.2.

For simple geometries, the area of the flame can be related to the fraction of burned gas, which in turn can be related to the instantaneous pressure. This relationship between flame area and instantaneous pressure leads to expressions for the scaled area as a function of pressure, and the pressure equation becomes an ordinary differential equation. This assumption is the basis for many approximate solution methods for leads

$$\frac{dp}{dt} = \frac{S_u^\circ \Delta p_{max}}{V^{1/3}} \frac{S_u}{S_u^\circ} \quad F(p/p_\circ, p_{max}/p_\circ, \gamma). \tag{18}$$

The function F depends on the exact geometrical model. The relationship (Eq. 12) between burned gas mass fraction and pressure used is independent from the kind of model chosen. Since the products of combustion are in a spatially nonuniform state, it is easier to work with either the compressed reactants or unburned volume in the computation. Integration of Eq. 12 yields

$$\frac{p - p_\circ}{p_{max} - p_\circ} = \frac{M_b}{M_\circ} = 1 - M_u/M_\circ = 1 - \frac{\rho_u V_u}{\rho_\circ V_\circ}. \tag{19}$$

The relationship of unburned volume to flame surface area has to be determined separately depending on the geometry of both vessel and flame.

Assuming the vessel is a sphere of radius R and at any time the flame is assumed to be a sphere with radius r, the function F for this case can be computed to be

$$F = 3\left(\frac{4\pi}{3}\right)^{1/3}\left(\frac{p}{p_\circ}\right)^{1/\gamma}\left[1-\left(\frac{p_\circ}{p}\right)^{\frac{1}{\gamma}}\left(\frac{p_{max}-p}{p_{max}-p_\circ}\right)\right]^{2/3}. \tag{20}$$

The maximum value of F occurs at the end of the burn and is

$$F_{s,max} = 3\left(\frac{4\pi}{3}\right)^{1/3}\left(\frac{p_{max}}{P_\circ}\right)^{1/\gamma}. \tag{21}$$

Spherical propagation is characteristic of the initial phase of any explosion and can be used to determine the initial pressure history. Integration of the pressure rise equation for early times ($p \leq 2P_\circ$) yields (Nagy et al. 1971) a cubic relationship

$$p(t) \approx p_\circ + \Delta p_{max}\left(\frac{p_{max}}{\gamma\ p_\circ}\right)^2\left(\frac{S_u t}{R}\right)^3 \tag{22}$$

or

$$\left(\frac{p(t)-p_\circ}{\Delta p_{max}}\right)^{\frac{1}{3}} \approx \left(\frac{p_{max}}{\gamma\ p_\circ}\right)^{\frac{2}{3}}\frac{S_u t}{R} = a\ S_u t. \tag{23}$$

Consequently, the slope of $(\Delta p)^{\frac{1}{3}}$ vs. t is proportional to S_u. A numerical fit to this equation is used to get S_u.

Only the initial portion of the pressure trace is used to calculate the laminar burning speed. The period of time is determined by trial and error and inspection of the fit to Eqn. 23. The time interval is entered individually for each evaluation and this choice is subjective to some extent. This initial pressure rise period does not correspond to the same state of flame propagation in vessels of different volumes.

Consider the simple model shown in Fig. 5. Two vessels of different volume symbolized by the cubes are considered. The vessels are filled with the same combustible mixture. When a centered ignition takes place in both vessels at exactly the same time, the flames have nearly the same dimensions after a period Δt. This state can be seen in the figure. (The fact that the pressure is higher in vessel 2 than in vessel 1, when the same mass of gas is burned, results in a higher compression of the gas in vessel 2 and thus in slightly smaller flame in this vessel. This effect is neglected, as only a simple model for the state of the flame propagation in different vessels is under consideration.) At Δt, the ratio of burnt gas to unburnt gas in vessel 2 is much higher than in vessel 1. As this ratio is proportional to the pressure measured by a sensor inside the vessel, this sensor would

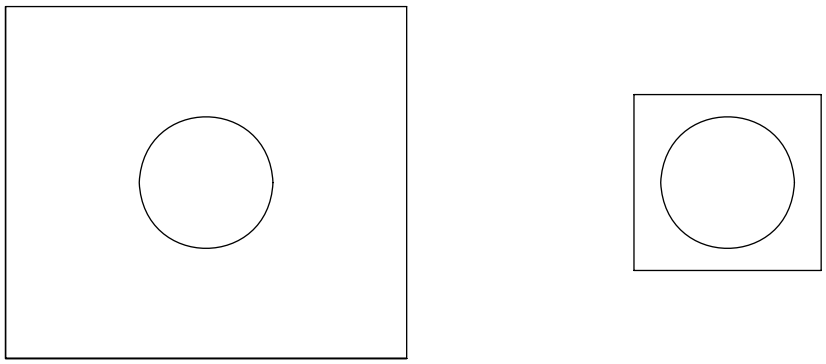

Figure 5: Flame in two vessels of different volume at the same point of time .

indicate a higher pressure for vessel 2 than for vessel 1. Since only data from the very early stage of flame propagation is used to compute S_u, the same increase of pressure is related to laminar flame propagation in one vessel and to an already turbulent flame propagation in a larger vessel. Therefore, results have to be interpreted carefully. The resulting flame speeds are not the laminar burning speed, but some effective burning speed that includes the effect of turbulence, flame instability, and vessel geometry.

2.6 Combustion Limits

For mixtures of fuels with oxidizers, there are certain limits of composition and pressure within which flame propagation may occur, and outside of which it is not possible to have a self-sustaining flame, known as the flammability limits. If an attempt to initiate combustion is made outside the limits, a flame may start but then quickly extinguishes. Flammability limits can be classified according to their propagation mode, upward or downward. Upward limits include buoyancy effects and represent the maximum flammability hazard. In downward propagating flames, buoyancy effects decrease the flame propagation speed as the vectors of burning speed and buoyancy have opposite directions. In addition to the buoyancy, differences in the molecular diffusivity between the fuel and the oxidizer cause the often observed wide variations between these limits. Flammability limits are strongly influenced by heat losses to vessel walls and propagation can become impossible at some quenching diameter. Only lean and stoichiometric mixtures were investigated in this study so that only the lower limits for upward propagating

flames are of interest. The flammability limits for upward propagation in air at initial conditions of T = 298 K and P = 1 bar are listed in Table 1 for the fuels of interest.

Table 1: Upward propagating flammability limits at 298 K and 1 bar.

Fuel	Oxidizer	Lower Limit [% Fuel]	Upper Limit [% Fuel]
Hydrogen	Air	4.0	75
Methane	Air	5.0	15
Ethane	Air	3.0	12.4
Propane	Air	2.1	9.5

If the flammability limits of the components are known, limits for a mixture of fuels (of similar type) can be predicted from Le Chatelier's law (Chatelier and Boudouard 1898). The specific form of this law for the lower limit of mixtures in air is

$$L = \frac{100}{\frac{P_1}{L_1} + \frac{P_2}{L_2} + ... + \frac{P_i}{L_i}}, \tag{24}$$

where P_1, P_2,... are the percentage proportions of each combustible in the mixture and L_1, L_2,... are the lower limits of each combustible gas in the mixture (also in percent). L then represents the lower flammability limit of the mixture in percent volume.

So far the fuels are restricted to be in the gaseous phase. When liquid fuels are involved, the vapor pressure of the mixture has to be considered. Both flammability limit and vapor pressure strongly depend on the temperature of the mixture. Mixtures of a combustible liquid-air system can consist of mists (droplets + saturated vapor + air), saturated vapor-air mixtures, or neat vapor-air mixtures. The temperature range over which the liquid can form a flammable vapor concentration is defined by the temperature limits of flammability. The lower temperature limit is of particular interest in this study as it defines the minimum temperature to which a combustible liquid must be heated to form a flammable vapor-air mixture. For simple mixtures, this temperature corresponds approximately to the flashpoint of the combustible.

3 Apparatus

3.1 Combustion Vessels

The experiments are performed in four different vessels with volumes varying from 1.84 liters to 1180 liters and geometries ranging from approximately rectangular to cylindrical in shape. The key parameters of each combustion vessel are discussed in the following paragraphs.

3.1.1 1.84 l Combustion Vessel with Heating Facilities (IGGY)

The 1.84-liter combustion vessel is primarily designed to measure ignition energies of vapors in equilibrium with liquid fuels. The approximately cubic interior has dimensions of about 140 mm × 140 mm × 100 mm. The walls are made of aluminum; the front and back wall contain circular windows to enable optical measurements, which consist of recording color Schlieren pictures of the combustion process with a video camera. From the two side walls, electrodes protrude into the vessel and form a spark gap in the center of the chamber. The electrodes are made of 3.2 mm diameter stainless steel rods with rounded tips. The gap between the electrodes can be adjusted with a micrometer screw. On the bottom of the vessel, a magnetic stirring rod provides a means to mix the liquid fuel. The turning speed of the mixer can be controlled electrically. The characteristic length is $l_{char} = V^{\frac{1}{3}} = 123$ mm. Another length used for comparisons is l_{max}, which is determined by assuming a cubic interior and a point shape ignition source in the center of the vessel. l_{max} then represents the length from the center of the vessel to one of the corners and is equal to 121 mm. The pressure history is recorded by a Kulite semiconductor pressure gauge model XMTE-190-250A. The pressure gauge is mounted in one of the side walls of the vessel. To monitor the initial pressure of the reactants and the final pressure of the products, a HEISE (model 901A) digital pressure indicator is used. The temperature history is recorded by an Omega K-type thermocouple located near the center of the vessel just above the spark gap. The vessel can be heated up with OMEGALUX (model SRT051-041) heating pads attached to the outside surface of the vessel. The power to the heating pads is controlled by a temperature controller unit which monitors the vessel temperature at different spots. Thermocouples are fixed on the top and bottom surfaces of the vessel as well as inside the vessel approximately 2 cm from the side wall. The vessel is placed in an insulating box and all remaining openings and the top of the vessel are covered with insulation.

3.1.2 11.25 l Combustion Vessel (MiniConvol)

The inside of the 11.25-liter constant volume combustion vessel has a rectangular shape with the interior dimensions of 190 mm × 203 mm × 305 mm. The walls are made of steel slabs, front and back wall are equipped with 25 mm thick BK-7 glass windows of 117 mm diameter to allow observation by a color Schlieren video-system. The electrodes used for spark ignition are inserted into opposite side walls so that a spark gap of variable width is formed in the center of the vessel. The electrodes are made of the same material as the ones in the 1.84-liter combustion vessel and the tips are also rounded. The gap width can be changed by sliding one of the electrodes and then fixing it with a set screw. The homogeneity of the combustible gas is insured by a single, two-blade mixing fan near the ceiling of the vessel. The characteristic length $l_{char} = V^{\frac{1}{3}}$ is 224 mm. The distance l_{max} from the centered point of ignition to the farthest corner of the vessel is 206 mm. The pressure and temperature history are recorded with the same Kulite semiconductor pressure gauge and Omega thermocouple, respectively, as used in the 1.84-liter vessel described above. The static pressure measurements were performed with the same Heise digital pressure indicator described above.

3.1.3 407 l Combustion Vessel (Convol)

The 407-liter Convol combustion vessel has a nearly cylindrical shape with an exterior length of 1235 mm and an inside diameter of 711 mm. The walls are constructed of SA-212-B carbon steel. Four penetrations lead into the vessel. The ignition system enters the tank from the left base, while the gas handling system enters from the right side. Two 25-mm-thick, 117-mm-diameter clear aperture BK-7 glass windows allow observation of the combustion phenomena with a Schlieren video system. The spark ignition system is centered in the middle of the tank and consists of two electrodes forming a gap with a manually adjustable width. The electrodes are made of stainless steel rods with rounded tips. The homogeneity of the mixture is assured by a two-blade mixing fan in the upper right part of the vessel. The mixer is typically run at about 250 rpm. The characteristic length $l_{char} = V^{\frac{1}{3}}$ is 741 mm. Assuming an interior length of 1025 mm, a diameter of 711 mm, and a centrally located ignition source, l_{max} is 624 mm. To measure static pressure, pressure history, and temperature history, the same instrumentation is used as in the other vessels .

3.1.4 1180 l Combustion Vessel (Hyjet)

The HYJET experimental facility consists of two pressure vessels, a driver, and a receiver, as shown in Fig. 6.

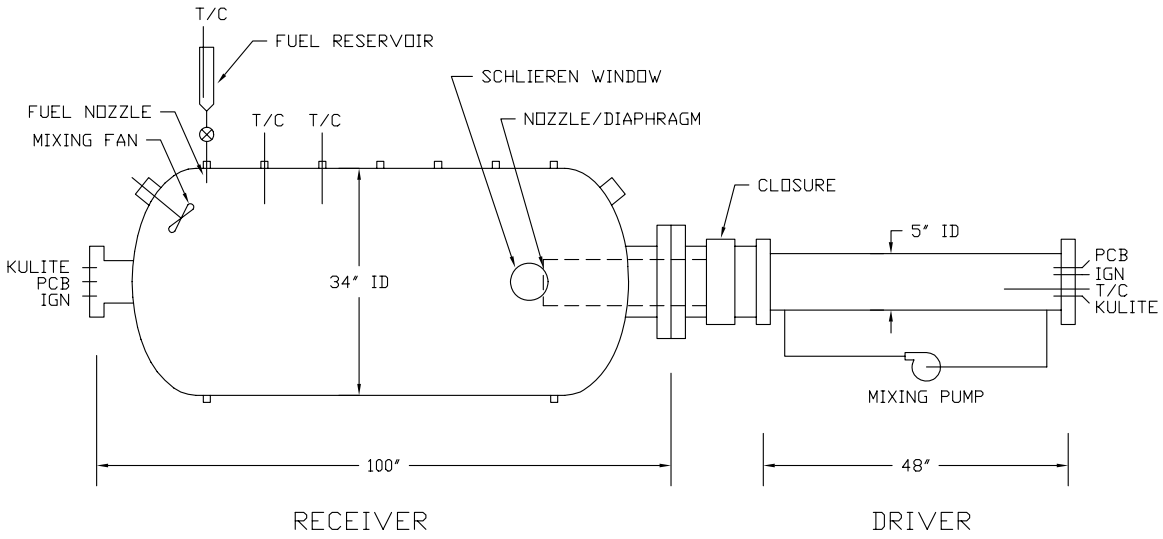

Figure 6: Schematic of the 1180 liter HYJET facility.

The smaller 28-liter driver is used for jet ignition of the combustible mixture in the receiver. Since spark ignition is used in the experiments performed for this report, only the larger receiver vessel on the left side is used. This combustion tank has a cylindrical shape and semi-elliptical heads. The internal dimensions are 860 mm in diameter and about 1600 mm in length between the head seams, which results in a volume of 1180 liters. The vessel is of a heavy steel construction that can withstand internal pressures of up to 70 bar. The nozzle adapter/diaphragm holder is replaced by a spark ignition system with manually adjustable gap width. When the facility is closed, the end of the driver is positioned in a way that the point of ignition can be observed by a Schlieren system through 118 mm diameter windows in the side of the tank. The vessel is instrumented with Kulite strain gauge pressure transducers and K-type thermocouples. The characteristic length l_{char} of Hyjet is 1057 mm, the length $l_{max} = 1616$ mm. Table 2 summarizes the characteristic lengths as well as the maximum lengths used in this report.

Table 2: Characteristic lengths.

Vessel	Volume V [l]	$V^{\frac{1}{3}}$ $[m]$	l_{max} $[m]$
Hyjet	1180	1.057	1.616
Convol	407	0.741	0.624
MiniConvol	11.25	0.224	0.206
IGGY	1.84	0.123	0.121

3.2 Gas Handling and Vacuum System

A schematic of the laboratory is shown in Fig. 7.

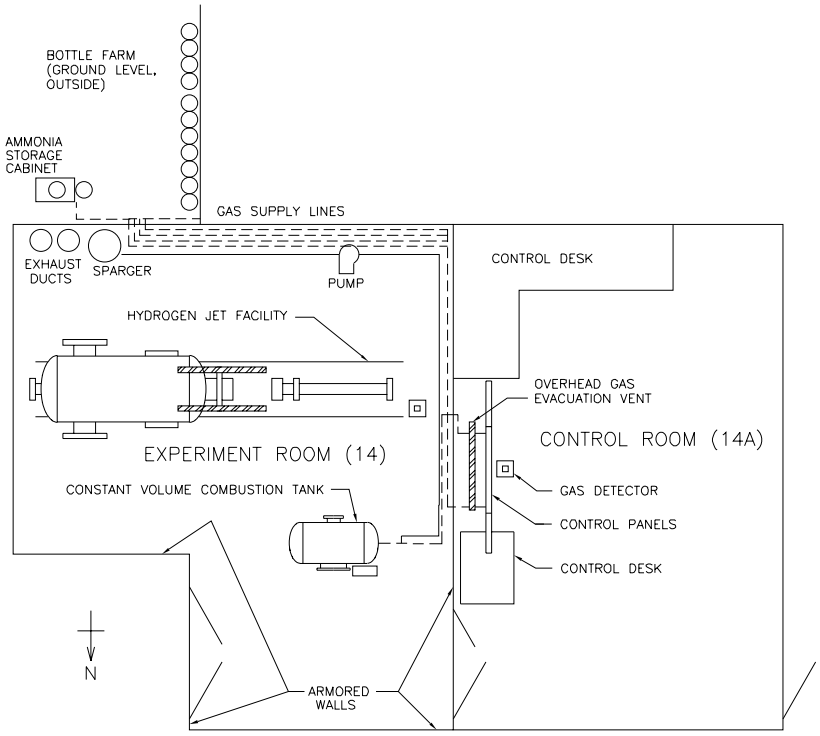

Figure 7: Explosion Dynamics Laboratory and experimental facility.

The fuel bottles are stored outside the building in a bottle farm to minimize the risk to building occupants as well as to ensure the safety of the operator. All bottles are secured with seismic restraints. All tubing is thick-wall stainless steel, connected by stainless steel Swagelok fittings. The bottles are fitted with two-stage regulators. Accidental dispensing of the gases in the laboratory is prevented by an electro-pneumatic valve actuated by a pushbutton switch on each line.

Security is assured by two gas detectors which ensure that the fuel concentration levels present in the laboratory stay below 1/100 of the LFL. In the event of a release that sets off the detectors, the emergency ventilation system is automatically activated and air is exhausted through the overhead evacuation vents. More detailed information on the safety and emergency system can be found in Ross and Shepherd (1996). All vessels are filled and evacuated from the control room. The gas supply system is designed for safe metering of the gases into the pressure vessels. The supply lines are thick-walled stainless-steel tubing, again connected with Swagelock fittings. Each line is protected by check valves; position indicators on the electro-pneumatic valves are interlocked through a logic control circuit to prevent accidental release of gas into the experimental area. The tanks are manually filled using partial pressures of the different components as filling criteria.

All experiments are carried out at an initial pressure of 100 kPa and consequently one percent of fuel or oxidizer in the vessel corresponds to the pressure of 1 kPa. For IGGY, MiniConvol, and Convol, this static pressure is measured by the Heise digital pressure indicator. The HYJET combustion facility filling is controlled by a precision Heise mechanical analog pressure indicator. As IGGY, MiniConvol, and Convol use the same plumbing system, only one of these vessels can be connected to the gas system and be operated at a time. The exhaust and vacuum system for all vessels is similar. During operation, the exhaust gases from the experiment are pumped out the main exhaust vent on the roof level. All plumbing used in the system is CPVC, except for the stainless steel valves and nipples near the vacuum pump. The gasroute for the three smaller vessels is shown in Fig. 8. The tank in the picture thus represents IGGY, MiniConvol, and Convol.

A Sargent-Welch 1397 vacuum pump with a capacity of about 500 liters per minute is used for evacuating IGGY, MiniConvol, and Convol. A Kinney KTC-112 vacuum pump with a capacity of about 3000 liters per minute is used for evacuating the HYJET facility. Depending on vessel size and temperature, the complete evacuation takes from 2 to 30 minutes. The vacuum typically achieved by the pumps has a residual pressure of 0.001 kPa, lower than the 0.01 kPa accuracy of the instrumentation.

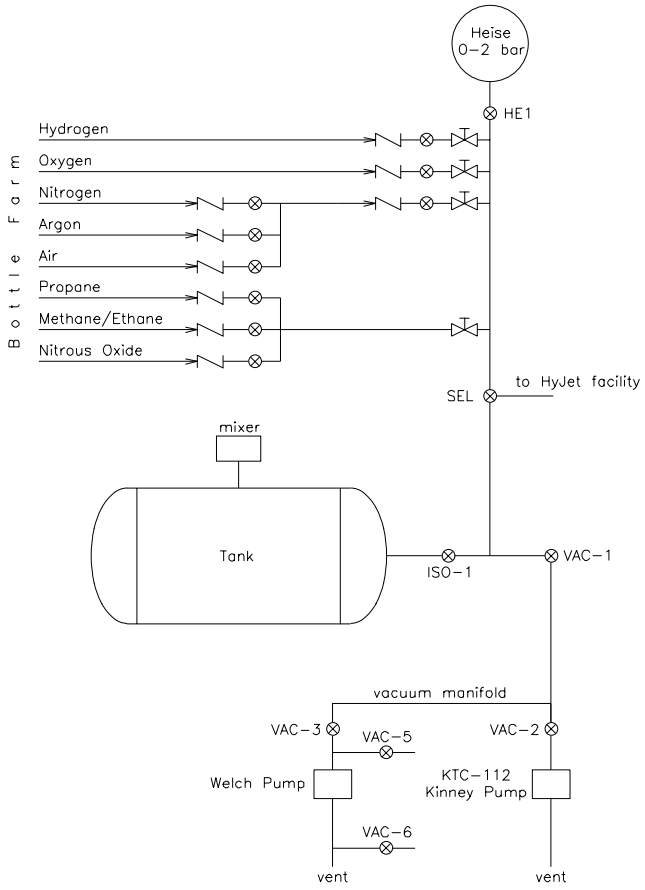

Figure 8: Gasroute for Convol, MiniConvol and IGGY vessel.

The fuels can be filled with an accuracy of about 0.05 kPa in IGGY. The filling error is defined as the ratio of maximum filling inaccuray, which is 0.05 kPa for IGGY, and the filling pressure of the fuel. For the leanest hydrogen mixture (9%), this results in a filling error of $0.05/9.0 \approx 0.56\%$. The same calculation is done for the other fuels and concentrations. The filling error for the richest hydrogen mixture is 0.018%. Methane has a filling error of 0.8% for the leanest mixture and about 0.5% for the stoichiometric composition. The leanest propane mixture has a filling error 1.6%. For mixtures near the stoichiometric point, propane has a filling error of about 1.3%. The smaller the amount of gas added to the vessel, the larger is the influence of the filling error. Another source of errors concerning the gas composition is residual fuel in the plumbing system. To minimize these errors, the plumbing system is evacuated between the fuel and air filling steps.

3.3 Instrumentation

Similar instrumentation is used for all combustion vessels. Signals for the pressure history are obtained from a Kulite semiconductor pressure gauge (model XMTE-190-250A). This piezoresistive transducer has a combined nonlinearity, hysteresis, and repeatability of 2.5 kPa. Signals from this pressure gauge are used to check the accuracy of the other pressure indicators during the filling of the tanks.

A Heise digital pressure indicator (model 901A) is used to meter the initial pressure of the reactants and the final pressure of the products in the 1.84, 11.25, and 407 liter vessels. This indicator has a range from 0 to 250 kPa absolute, and an accuracy of $\pm$ 0.18 kPa. As the sensor is very fragile and can not stand temperatures above about 300 K, it is switched off and separated from the vessel by a valve before ignition.

The initial, filling, and final pressure in the Hyjet combustion facility are controlled by a precision Heise mechanical analog pressure indicator with a range from 0 to 200 kPa. To protect it from damage, a valve is used to separate the indicator from the system before the ignition.

In all vessels, the temperature is measured by Omega K-type thermocouples. To convert the thermocouple output to temperature, an electronic cold-junction (Omega, model DP462) and temperature readout is used.

3.4 Ignition System

Two different methods are used to ignite the gaseous mixtures in the combustion vessels: sparks and hot filaments.

3.4.1 Spark Ignition

All vessels except for the 1180-liter tank (Hyjet) have the ignition source centered in the tank. As seen in Fig. 6, the position of the electrodes in Hyjet is at the end of the driver, protruding about 630 mm into the receiver. In all vessels, the electrodes are made of stainless steel rods with a 3.2 mm diameter and rounded tips. The gap width can be adjusted manually by means of micrometer or regular screws. The electrodes are insulated with Teflon plugs and removable silicon paste to ensure that the ignition spark is located between the electrodes and not between the anode and the chamber wall. The power for the spark is provided by a capacitor discharge system, which consists of an

EG&G TM-11A trigger module and a 0.5 μF capacitor charged by a Hipotronics (15 KV max) power supply. The discharge across the gap is initiated by a 30 KV low-energy pulse ($\approx$ 40 mJ) when the TM-11 is triggered. The energy of the spark can be calculated by assuming that it is equal to the energy stored in the capacitor

$$E = \frac{1}{2}\, C\, V^2, \tag{25}$$

where E is the spark energy, C, the capacitance in farads, and V, the charging voltage in volts. According to Eqn. 25, the ignition energy can be varied by adjusting the Hipotronics output voltage to the desired level or by varying the capacitance. A constant voltage of 6 KV resulting in an ignition energy of about 9 Joules is chosen for the pressure analysis experiments.

A hand switch is used instead of the TM-11 for most of the ignition energy experiments. Capacitances from 0.032 nF to 1300 μF are charged with voltages ranging from 4.5 KV to 15 KV. The resulting ignition energies have minimum values of 0.001 J and maximum values of about 27 J.

The determination of the exact amount of energy released in the spark is difficult due to dissipative and radiative electromagnetic losses in the circuit as well as energy remaining in the capacitor after discharge . However, this energy is far above the Minimum Ignition Energy (MIE) of the fuel-air mixtures examined in this study so that these losses have no influence on the experiment. The circuit is similar to the design described in Ronney (1985).

No capacitor is used in Hyjet; the 30 KV pulse from TM-11 creates the ignition spark. This pulse is equal to an ignition energy of about 0.04 J. More detailed information about spark ignition and the related ignition energies can be found in Shepherd et al. (1998).

3.4.2 Filament Ignition

A hot filament is used for ignition in selected tests. A commercial 12.5-Volt Phillips miniature light bulb (model Ph1156) is used with glass bulb removed. The electrodes are connected by means of a wire soldered to the bulb and to the electrode. The bulb is positioned so that the filament is visible in the center of the observation window of the vessel. The light bulb ignition system circuit diagram is shown in Fig. 9.

The operation of the circuit begins by closing switch S_1 to charge the 1300 μF capacitor to about 150 V. This charge corresponds to a stored energy (Eqn. 25) of about 15 J.

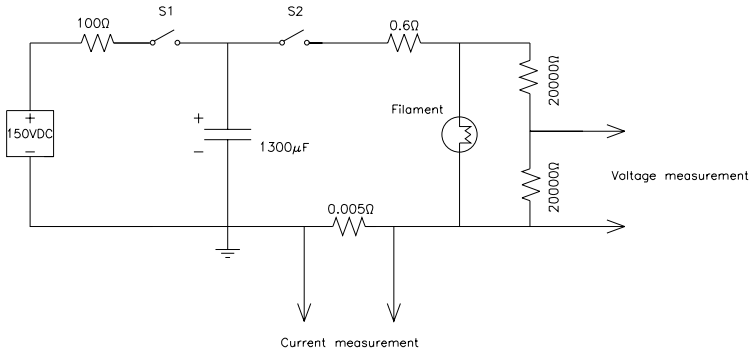

Figure 9: Electrical circuit for filament ignition.

Switch S_2 is then closed to discharge the stored energy into the filament, which rapidly heats up and ignites the surrounding gas. The filament has a cold resistance of about 0.6 Ω so that the the temperature increases very quickly and there is only a short delay between closing S_2 and ignition.

3.5 Optical System

The optical system is similar for all types of vessels and consists of a light source, two converging lenses, a collecting lens, two turning mirrors, a collimating mirror, a focusing mirror, a RGY filter, and a CCD camera. A schematic diagram of the optical system is shown in Fig. 10. An Oriel continuous filament lamp is used as light source, except in the Hyjet facility, where a continuous arc-lamp provides the light. Light rays pass through a pair of converging lenses to focus on a pinhole, producing a spherically-diverging beam. This beam reflects off a collimating mirror producing parallel light rays that pass into the test section. The individual light rays are reflected by different amounts due to the index-of-refraction gradient caused by the flame. For gases, this index-of-refraction gradient is proportional to the density gradient. After passing through the test section,

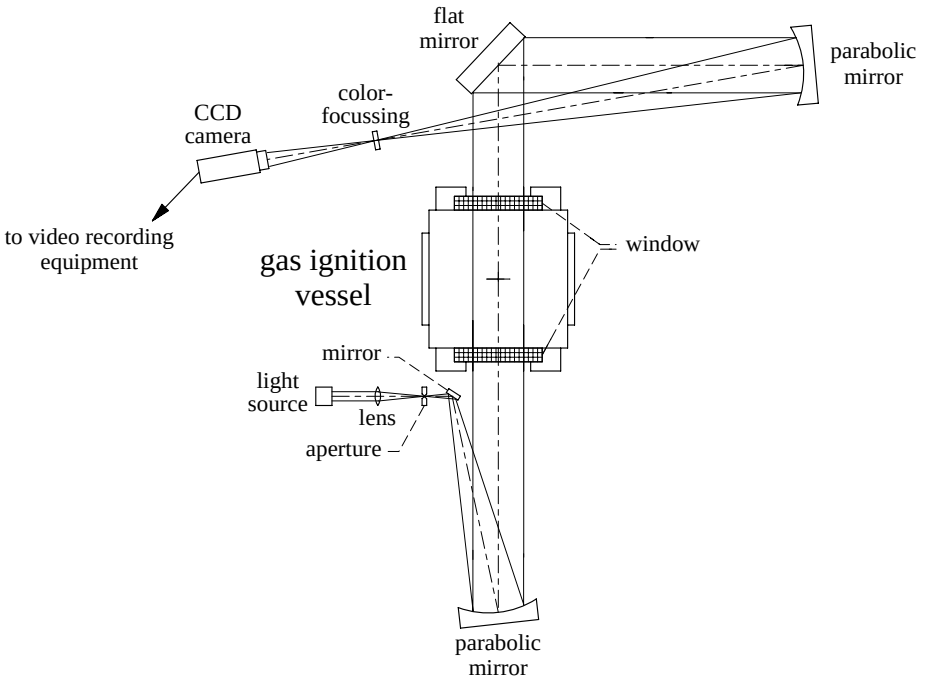

Figure 10: Schematic diagram of the color schlieren video system.

the light beam is turned and focused on a three-color red-blue-yellow filter (RBY). The optical system is aligned so that undeflected light passes through the center of the RBY-filter while deflected light rays pass through one of the colored sections according to the direction of the deflection. The CCD camera located after the filter shows the interior of the vessel and the flame when combustion occurs. The pictures are monitored on a TV-screen and taped by a video recorder.

When a large fraction of the light passes through one of the colored sections of the filter, this color is dominant on the picture and indicates the direction of the light rays. Regions of the test section where the density gradient is large appear as high contrast on the Schlieren photograph, while regions with a smaller density gradient appear as low contrast regions on the photograph. For this reason the color-schlieren picture is a picture of the density gradient field within the examined section of the vessel where the contrast represents the magnitude and the color represents the direction. For the experiments in Hyjet, a knife edge instead of the color filter is used, which is equally appropriate as only the magnitude of the density gradient is needed for the experiments. A Sony CCD camera (model DXC-107A) is used for the IGGY, MiniConvol, and Convol vessels. The framing rate is a 2:1 interlace, 30 frames/sec, which translates into a frame every 16.67 ms. The camera is equipped with an electronic shutter; the exposure times

of 1/2000 s and 1/4000 s are used for this study. The lens of the camera is a Fujinon model C6X18G-1 television zoom lens with a 6× zoom ratio and a 108 mm focal length. For the Hyjet facility a Pullnix TM-9700 CCD camera with a Fujinon model C6X17.5B lens is used. The framing rate is equal to that of the Sony camera.

3.6 Data Acquisition

The pressure and temperature signals are recorded by Labview data acquisition software running on a Gateway P5-100 personal computer for the experiments in IGGY, Mini-Convol, Convol, and by the same software on a Gateway P5-133 for the shots in Hyjet. Temperature and pressure signals are amplified by signal amplifiers and digitized by a National Instruments AT-MIO-64E-3 multi-purpose board sampling at a rate of 1000 Hz. The data acquisition system is triggered by the fire button for the spark ignition. The data acquisition period is limited to 8 seconds for the smaller test vessels and to 4 seconds for Hyjet.

4 Experimental Procedure

Hydrogen-air, methane-air, ethane-air, and propane-air mixtures are investigated in each vessel. Only stoichiometric and leaner fuel-air mixtures are examined, since low burning speeds are the main interest of this study. The exact composition of the mixtures, the combustion vessels used in the experiments, and the laminar burning speed from literature, $S_{u,lit.}$, are shown in Table 3. The laminar burning speeds for hydrogen are from Koroll et al. (1993), the values for the hydrocarbons are from Kuchta (1985).

All experiments are carried out under the same initial conditions. The vessels are evacuated to a pressure of about 0.01 kPa and then filled to an initial pressure of 100.0 kPa. The initial temperature is 295 K. Due to the heat release during the experiments, the initial temperature increases 5-10 K after some tests. The frequency of runs is mainly determined by the cool-down time of the vessels. The mixing fan/stirrer is turned off before ignition, so that initial conditions are quiescent.

4.1 Procedure in Combustion Pressure Experiments

The experimental procedure is similar for all combustion pressure experiments. The mixtures are prepared with the method of partial pressure. Checklists are used to ensure that startup, operation, and shutdown tasks are completed. The operator first selects the composition of the mixture and computes the corresponding partial pressures of each component. The experiment begins by evacuating the system and zeroing the pressure transducer. First, the gas supply plumbing is evacuated and the Heise gauge is set to zero. Second, the tank is evacuated until the pressure approaches 0.01 kPa. Then the dynamic pressure transducer is zeroed. The vessel is separated from the vacuum pump. Now the filling of the individual components begins. When the filling of the fuel is done, the lines are evacuated to prevent remaining fuel from spoiling the composition of the mixture. The tank is filled with air until the desired initial pressure is attained. The tank is then disconnected from the supply system; the Heise pressure gauge is also separated from the tank by a valve and turned off. All supply valves are also closed. The mixer is then switched on for a duration of 3-4 minutes. Just prior to ignition the mixer is switched off and the initial tank temperature is recorded. The next step is to arm the spark system. After arming the data acquisition system (which is triggered by the firing circuit), and starting the video recorder, the fire button is pressed to create the spark. If the reactants ignite, the system is disarmed. If the reactants do not ignite, the data

Table 3: Investigated mixtures and used vessels.

Hydrogen [%]	Air [%]	Equivalence ratio	$S_{u,lit.}$ [cm/s]	combustion vessel used
9.0	91.0	0.24	20	Hyjet, CV, MCV, IGGY
10.0	90.0	0.26	30	Hyjet, CV, MCV, IGGY
12.0	88.0	0.32	40	Hyjet, CV, MCV, IGGY
14.0	86.0	0.39	60	Hyjet, CV, MCV, IGGY
20.0	80.0	0.60	140	Hyjet, CV, MCV, IGGY
28.0	72.0	0.93	240	Hyjet, CV, MCV, IGGY
Methane [%]	Air [%]	Equivalence ratio	$S_{u,lit.}$ [cm/s]	combustion vessel used
5.93	94.07	0.60	15	Hyjet, CV, MCV, IGGY
6.85	93.15	0.70	20	Hyjet, CV, MCV, IGGY
7.76	92.24	0.80	30	Hyjet, CV, MCV, IGGY
9.03	90.97	0.94	40	Hyjet, CV, MCV, IGGY
9.51	90.49	1.00	45	Hyjet, CV, MCV, IGGY
Ethane [%]	Air [%]	Equivalence ratio	$S_{u,lit.}$ [cm/s]	combustion vessel used
3.75	96.25	0.69	25	Hyjet, CV, MCV
4.03	95.97	0.74	30	Hyjet, CV, MCV
4.58	95.42	0.85	35	Hyjet, CV, MCV
5.12	94.88	0.95	40	Hyjet, CV, MCV
5.66	94.34	1.000	45	Hyjet, CV, MCV
Propane [%]	Air [%]	Equivalence ratio	$S_{u,lit.}$ [cm/s]	combustion vessel used
3.05	96.95	0.750	25	Hyjet, CV, MCV, IGGY
3.35	96.65	0.83	30	Hyjet, CV, MCV, IGGY
3.47	96.53	0.86	40	Hyjet, CV, MCV, IGGY
3.84	96.16	0.95	45	Hyjet, CV, MCV, IGGY

acquisition and video systems are reset and the fire button pressed again. If after several trys no burn is observed, the mixture is inerted with nitrogen and pumped out through the exhaust system. In case of proper ignition, the mixer is turned on after the video recording is terminated to cool down the products. Once the temperature decreases to $\sim 30°C$, the valve to the Heise gauge is opened. After the final pressure and temperature are recorded, the vacuum system is opened. The products are removed from the tank and vented through the exhaust system. Depending on the energy released in the reaction,

the tank has to cool down for up to four hours (depending on the vessel) before the next experiment can start.

4.2 Procedure in Ignition Energy Measurement Experiments

The ignition energy measurements are mainly carried out in the 1.84-liter vessel. The evacuation and filling processes are similar to the ones described above. The major difference is that liquid fuels are used instead of gases, except for some Jet A simulant tests. Furthermore, in some experiments the vessel is heated to temperatures of 40, 50, or 60°C.

The fuel is injected using a hypodermic needle through a septum on top of the vessel or through an opened window, which is immediately closed after the fuel is added to the tank. The windows are preheated with a heatgun to prevent the fuel from condensing at the window surface. The pressure is then decreased to the initial experimental pressure by using the same vacuum system as mentioned above. When the desired pressure is reached, all valves are closed and the Heise pressure gauge is turned off. The tank is then heated up to the initial experiment temperature with the heat pads described in Chapter 3.1.1. Top, bottom, and inside temperature are monitored. The stirrer on the bottom of the vessel is turned on to increase the evaporation of the fuel. During the heating period the windows are covered with insulating material. The connection to the vacuum system is also heated with a heatgun to avoid condensation. Once the system reaches a thermal equilibrium at the chosen temperature, the stirrer is turned off and the insulation is removed from the windows. The experiment is carried out at quiescent conditions. Finally, the video, data acquisition, and ignition system are armed and the fire button is pressed. If there is no ignition, all systems are reset, the ignition energy is increased and a new attempt to initiate the mixture is made. When combustion occurs, the ignition systems is disarmed and the video is stopped after 20 seconds. After the cool-down period, the final pressure is measured and the tank is evacuated. The vessel has to be cleaned thoroughly after every shot to remove the residual fuel, even when combustion takes place.

5 Results

The principal results of 75 experiments for combustion pressure analysis and 30 experiments for ignition energy measurements are summarized in this Chapter. A full listing of all experiments and key data is given in Appendix A and B.

5.1 Combustion Pressure Analysis

5.1.1 Raw Pressure Data

The data obtained from the pressure gauge represent an instantaneous pressure measured at the locations mentioned in Chapter 3.1. As pressure changes propagate with the speed of sound, this pressure is representative for the whole vessel. Typical pressure traces for the first 4 seconds of the combustion are shown in Figs. 11 and 12. Figure 11

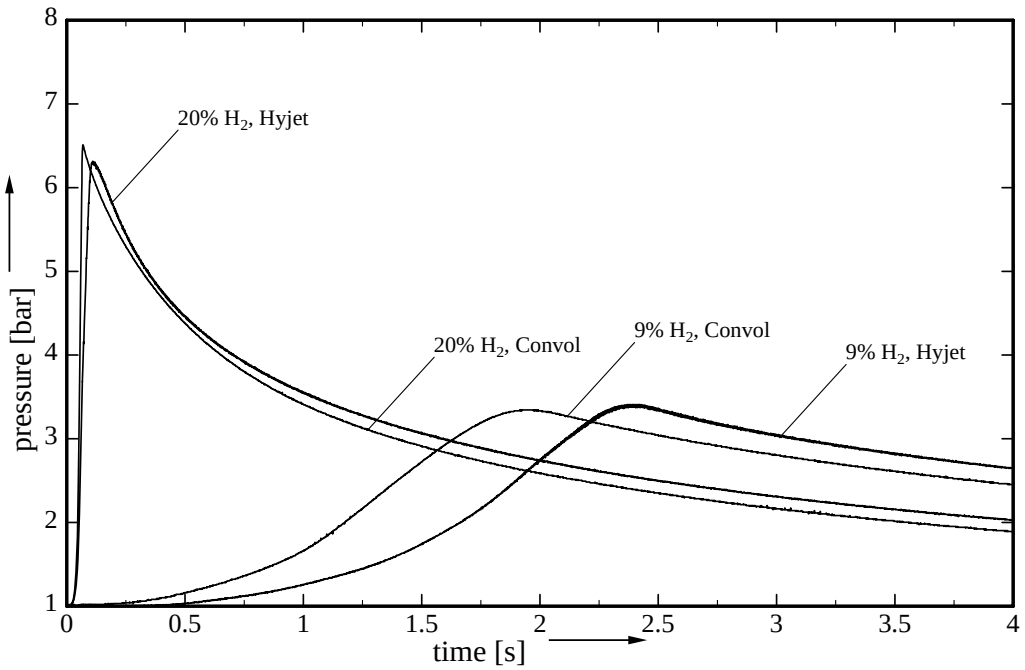

Figure 11: Pressure trace of hydrogen-air mixtures in Hyjet and Convol; initial conditions p = 1 bar, T = 295 K.

shows the pressure history of a 9% and a 20% hydrogen-air mixture, which corresponds to an equivalence ratio of $\phi = 0.24$ and $\phi = 0.60$, respectively. Figure 12 shows the pressure history of a 5.93% and a 9.51% methane -air mixture, which corresponds to an

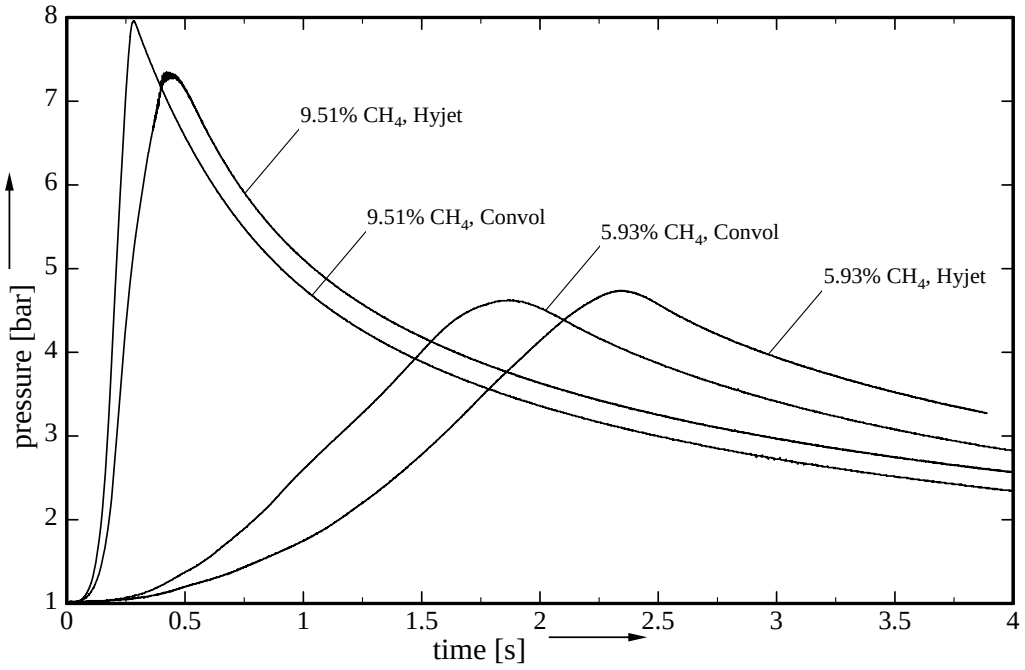

Figure 12: Pressure trace of methane-air mixtures in Hyjet and Convol; initial conditions p = 1 bar, T = 295 K.

equivalence ratio of $\phi = 0.6$ and $\phi = 1.0$, respectively. The pressure traces can all be separated in two phases: pressure rise phase and a pressure decreasing phase. The peak pressure, p_{max}, is located in between these two phases and marks the turning point where the pressure time derivative is zero. Note that the different plots may vary in up to three of the following parameters: type of fuel, equivalence ratio, type of vessel.

The pressure histories show four characteristic aspects of lean fuel-air mixtures:

1. The peak pressure increases with increasing amount of fuel.
2. For higher equivalence ratios, the pressure rise is steeper than for lower equivalence ratios.
3. For the same mixture composition, the pressure rise in smaller vessels is steeper than the pressure rise in larger vessels.
4. The onset of the pressure rise depends on the equivalence ratio. The higher the equivalence ratio, the earlier the pressure rise can be observed.

Characteristics 1, 2, and 4 can be explained by the chemistry, but item 3 is different. The pressure measured by the pressure gauge represents the mean pressure in the combustion vessel.

Assuming equal initial conditions, at the same point of time the ratio of burned to unburned gas in a small vessel is higher than in a large vessel. This is true until the gas in one of the vessels is completely burned. Consequently the pressure rise is steeper in smaller vessels.

Figures 13 through 16 show peak pressures vs. the equivalence ratio ϕ for all mixtures. The same symbols are used for each vessel in different plots. The 407-liter is abbreviated CV and the 11.25-liter vessel is abbreviated MCV. The AICC pressure computed by STANJAN is also shown. All connecting lines are 2nd-order least-squares fits to the data.

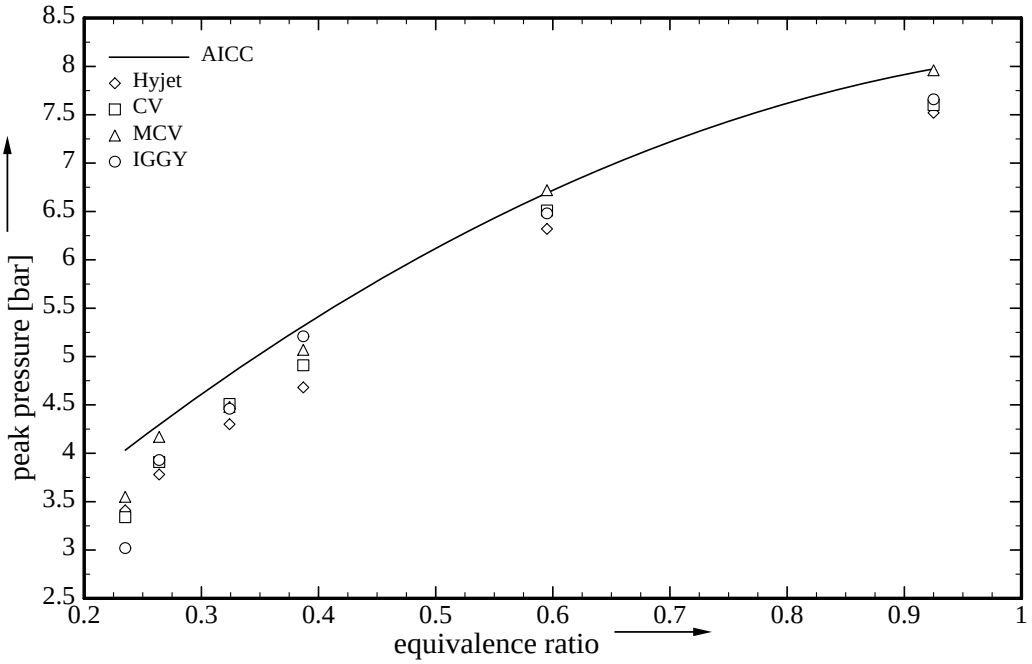

Figure 13: Peak pressures of hydrogen-air mixtures; initial conditions p = 1 bar, T = 295 K.

The AICC pressure is calculated by assuming a complete combustion and represents the maximum attainable peak pressure. Due to the various energy losses (see Chapter 2.4), all experimental pressures fall below the AICC values. The energy loss is represented by the peak pressure difference $\Delta p = p_{AICC} - p_{exp}$. The wider the gap between AICC pressure and experimental peak pressure, the higher the energy loss dur-

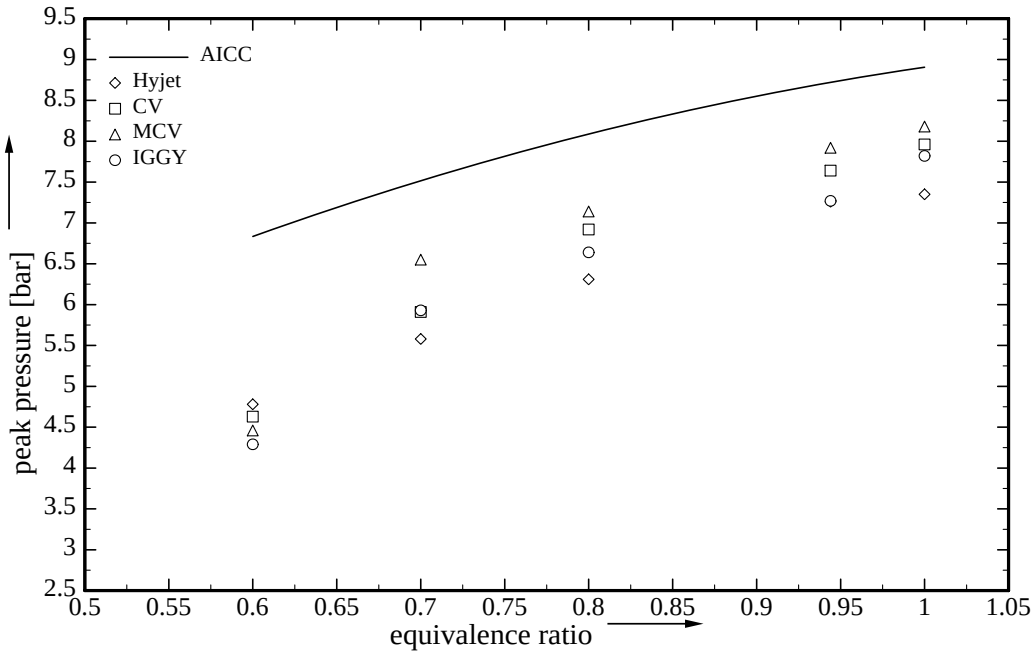

Figure 14: Peak pressures of methane-air mixtures; initial conditions p = 1 bar, T = 295 K.

ing the burn.

The peak pressures for the hydrogen-air mixtures range from 3.0-3.5 bar for very lean mixtures to about 7.5-8.0 bar for nearly stoichiometric mixtures (see Table 6 in Appendix A). The pressure difference Δp between the AICC pressure and the experimental pressure never exceeds 0.9 bar; in most cases the difference is even under 0.5 bar. Thus it can be concluded that the energy losses are relatively small (compared to other fuels). A major reason for the small losses is the high burning speed of hydrogen. Another reason is that radiation losses from the combustion products (water) are much smaller for hydrogen-air mixtures than for hydrocarbon-air mixtures, which have carbon dioxide-water mixtures in the products. Losses increase with increasing vessel volume for experiments with equal equivalence ratio.

The peak pressures for methane-air mixtures range from 4.25-4.75 bar for lean to 7.25-8.25 bar for stoichiometric mixtures. The pressure differences Δp between AICC and experimental pressure range from 0.75 to 2.5 bar. Energy losses are larger than in the hydrogen-air case. For all vessels, the losses increase with decreasing equivalence ratio. Neglecting the results for the IGGY vessel (small volume) and for the experiment with $\phi = 0.6$ (uncertain filling accuracy), it can be stated that for the same equivalence

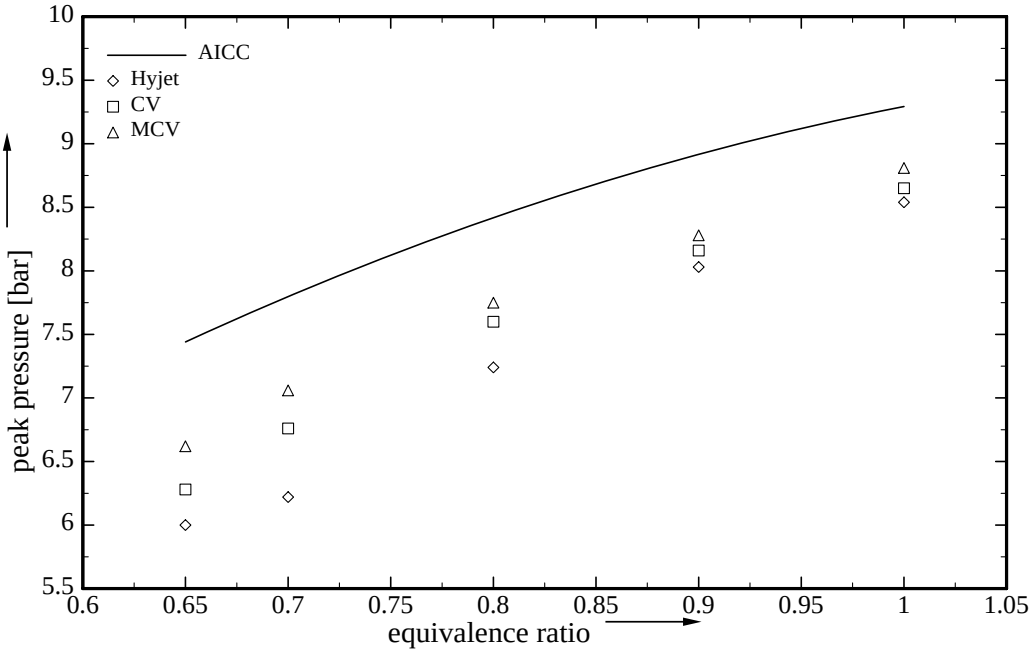

Figure 15: Peak pressures of ethane-air mixtures; initial conditions p = 1 bar, T = 295 K.

ratio, the losses increase with the vessel size.

The peak pressures for ethane-air mixtures range from 6.0-6.6 bar for lean to 8.5-8.75 bar for stoichiometric mixtures. The pressure differences Δp between the AICC pressure and the experimental pressure range from 0.5 to 2.0 bar. Energy losses increase for decreasing equivalence ratios.

The peak pressures for propane-air mixtures range from 6.25-7.0 bar for lean to 8.0-8.25 bar for nearly stoichiometric mixtures. The differences between the AICC pressure and the experimental pressure range from 1.0 to 2.0 bar. The energy losses increase for all vessels with decreasing equivalence ratio. The pressure in different vessels at equal equivalence ratios varies from 0.1 to 0.9 bar. Taking into account all four figures, it can be observed that, as expected, the experimental pressure is always below the AICC pressure.

Figures 17 and 18 show the peak pressure differences $\Delta p = p_{AICC} - p_{exp}$ of all experiments performed in the 407-liter and 11.25-liter vessels vs. the equivalence ratios. As mentioned, the difference between the AICC pressure and the experimental peak pressure can be used to compare the different amounts of energy lost in the combustion. It is obvious that energy losses for all hydrocarbon-air mixtures are much higher than

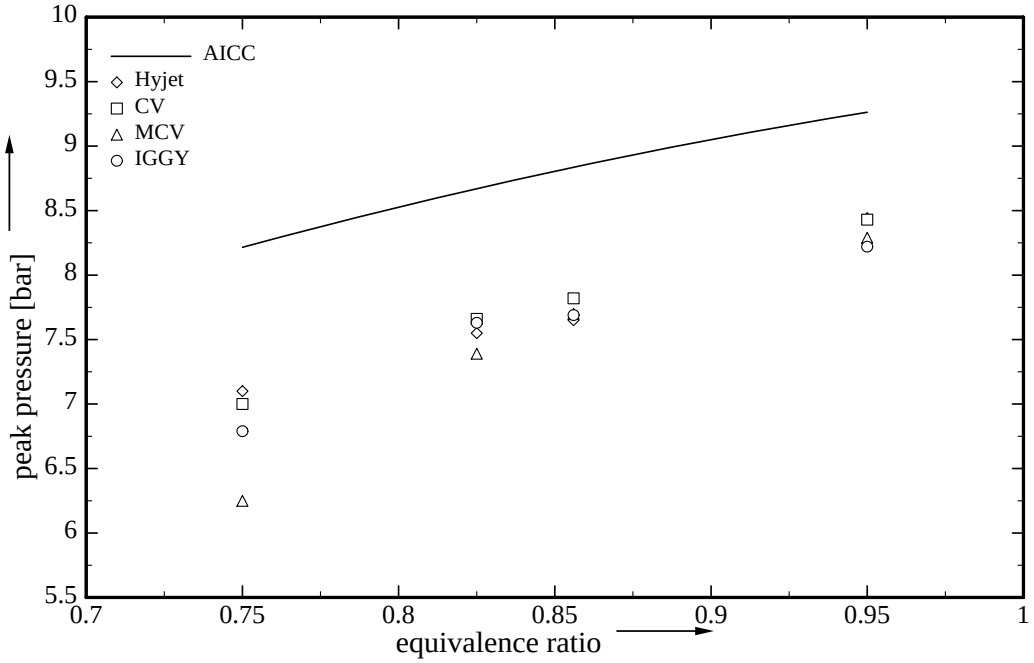

Figure 16: Peak pressures of propane-air mixtures; initial conditions p = 1 bar, T = 295 K.

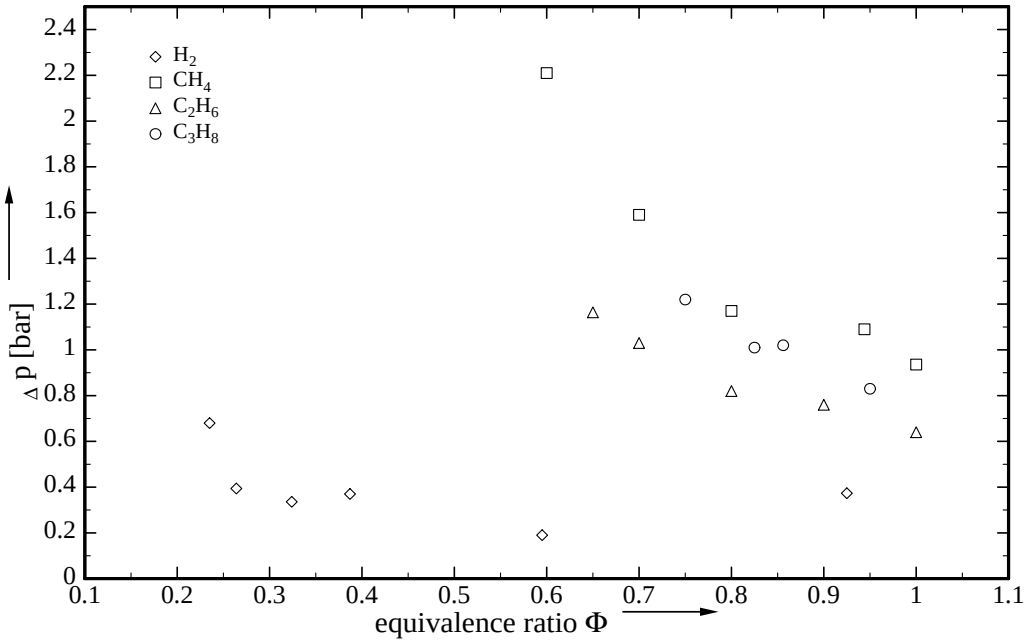

Figure 17: Peak pressure differences for all fuels in Convol; initial conditions p = 1 bar, T = 295 K.

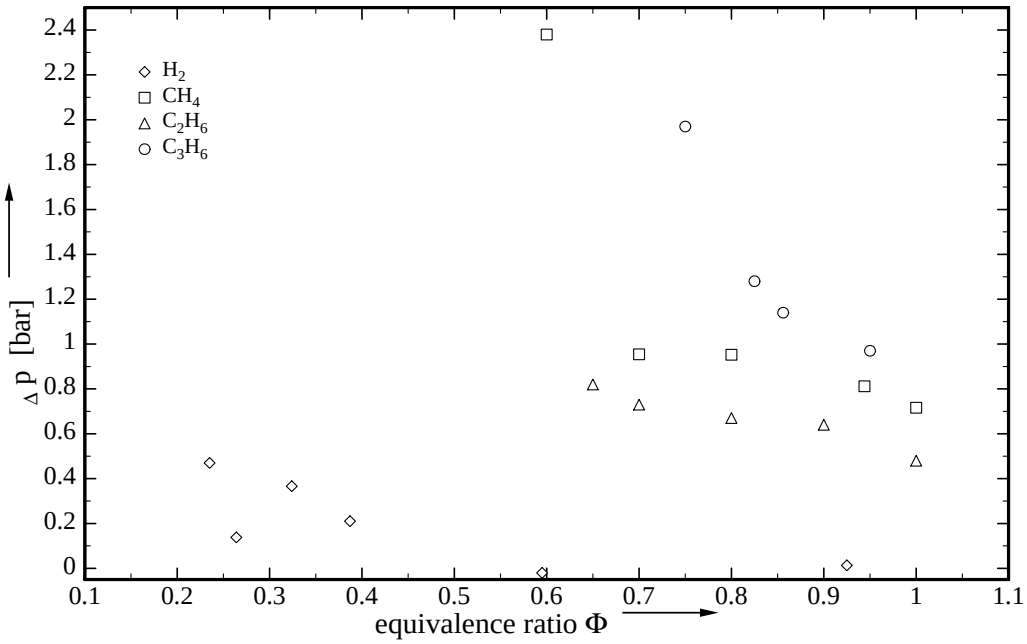

Figure 18: Peak pressure differences for all fuels in MiniConvol; initial conditions p = 1 bar, T = 295 K.

for the hydrogen-air mixtures. It can be observed that these losses are higher for small equivalence ratios than for equivalence ratios near the stoichiometric composition.

Several factors are expected to have an influence on the amount of energy lost during the combustion. The major parameters are the type of fuel, the equivalence ratio of the mixture, and the size and geometry of the vessel. Directly related to the choice of the fuel type and the equivalence ratio are the influence of the laminar burning speed and the flame temperature.

Figures 40 to 43 indicate that laminar burning speeds for hydrogen-air mixtures are much higher than for comparable hydrocarbon-air mixtures. Within one type of fuel, the laminar burning speed increases with increasing equivalence ratio as far as lean mixtures are concerned. In the following figures, energy losses are made clearer by the dimensionless ratio:

$$\frac{\Delta p}{p_{AICC}} = \frac{p_{AICC} - p_{max}}{p_{AICC}}, \tag{26}$$

where p_{max} is the experimental peak pressure and p_{AICC} is the computed AICC pressure. The smaller the ratio, the smaller are the energy losses.

The dependence of the energy losses on the laminar burning speed (literature values) in the 407-liter and 11.25-liter vessels are shown in Figs. 19 and 20. Generally, it can

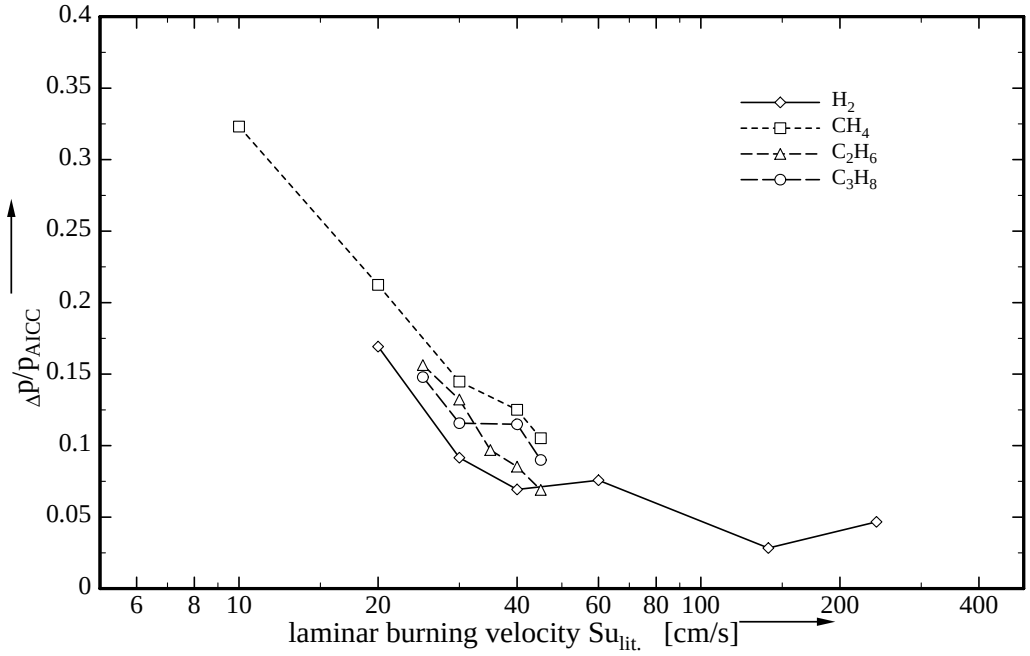

Figure 19: $\Delta p/p_{AICC}$ vs. $S_{u,lit.}$ for all fuels in Convol; initial conditions p = 1 bar, T = 295 K.

be stated that energy losses are smaller for fast burning flames, than for slow burning flames. This may be explained by the fact that there is less time for heat tranfer during the burn for fast flames than for slow flames. Another parameter to keep in mind is the flame temperature.

As seen in Chapter 2.4 the radiation losses are strongly related to the maximum flame temperature. Temperature trace analysis is not used in this investigation as the instrumentation does not determine accurate temperatures. For the purpose of estimation, the AICC temperatures are used to examine the influence of the flame temperature on heat transfer during the burn. Figures 21 and 22 show the energy loss parameter $\Delta p/p_{AICC}$ vs. the AICC temperature. All fuels in the 407-liter and 11.25-liter vessels are shown. Though it could be expected that higher flame temperatures lead to greater losses, this trend cannot be observed. It can be concluded that high flow speeds have a stronger impact on the energy losses during the burn than high temperatures.

The ratio of inside vessel surface to vessel volume may also influence the energy losses. The higher this ratio, the more energy loss is expected due to thermal conduction. Large

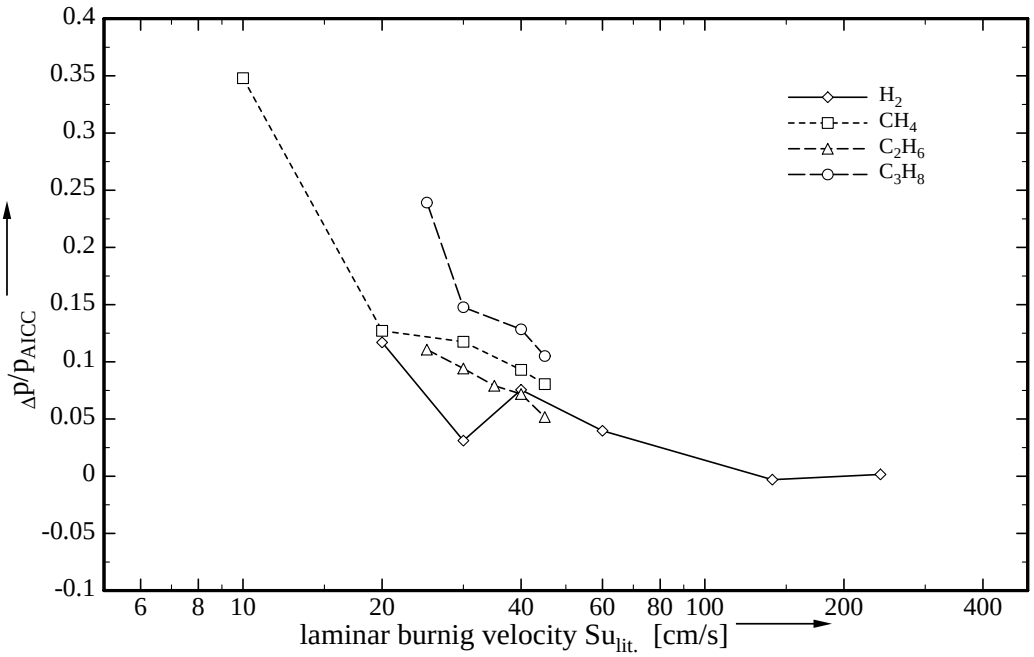

Figure 20: $\Delta p/p_{AICC}$ vs. $S_{u,lit.}$ for all fuels in MiniConvol; initial conditions p = 1 bar, T = 295 K.

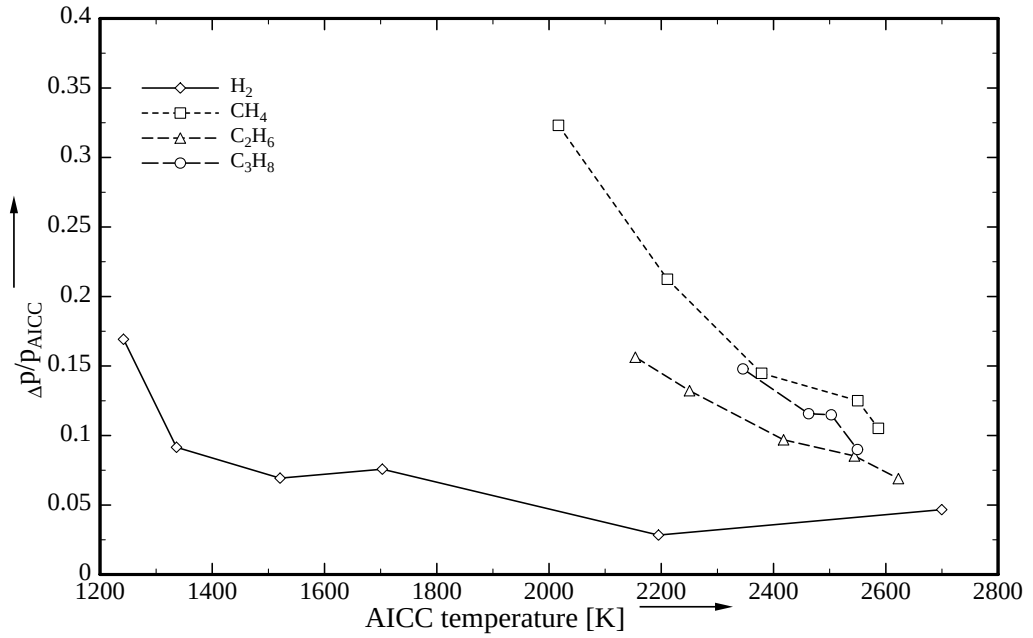

Figure 21: $\Delta p/p_{AICC}$ vs. T_{AICC} for all fuels in Convol; initial conditions p = 1 bar, T = 295 K.

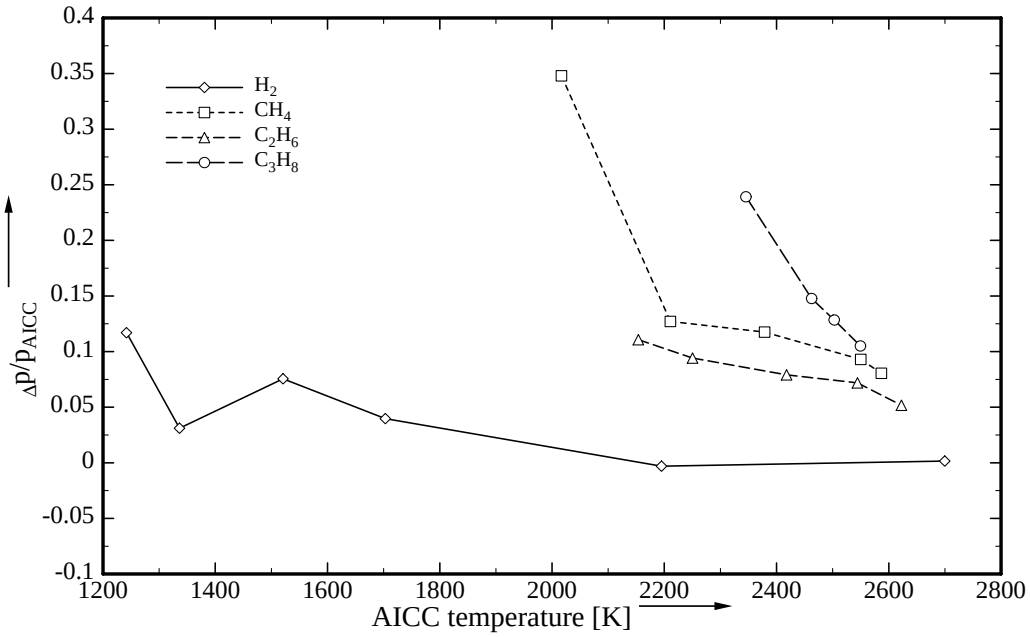

Figure 22: $\Delta p/p_{AICC}$ vs. T_{AICC} for all fuels in MiniConvol; initial conditions p = 1 bar, T = 295 K.

vessels (of spherical shape in particular) will minimize energy losses.

The dependence of energy losses on the vessel volume is shown in Figs. 23 and 24 for hydrogen and methane. It could be expected that, the larger the vessel, the longer the combustion takes, and thus the more energy lost due to thermal convection and conduction. This expectation cannot be clearly certified by the two figures. For many equivalence ratios, a trend can be seen, however the error bars for all experiments are uncertain and further conclusions would be speculative. The experiments have to be repeated to determine errors.

5.1.2 Pressure Rise Coefficient K_g

As mentioned in Chapter 2.5, the pressure rise coefficient, K_g, is one common parameter to describe closed-vessel combustion. K_g is defined as the product of the maximum pressure rise $(dp/dt)_{max}$ during the combustion and a characteristic length. The maximum pressure rise is calculated from the pressure history. In order to compute $(dp/dt)_{max}$, the experimentally measured pressure signals are numerically differentiated. Since differentiating amplifies any noise present in the signal, an averaging process is applied before the differentiation is carried out. A symmetric triangular weighting function is used to

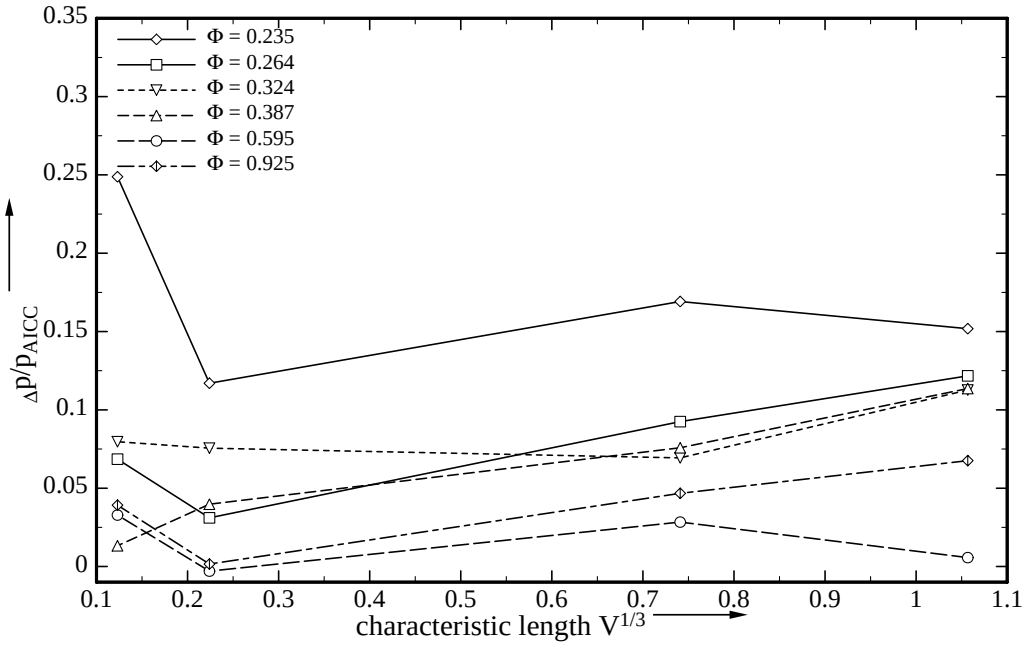

Figure 23: $\Delta p/p_{AICC}$ vs. characteristic length $V^{\frac{1}{3}}$ for hydrogen-air mixtures; initial conditions p = 1 bar, T = 295 K.

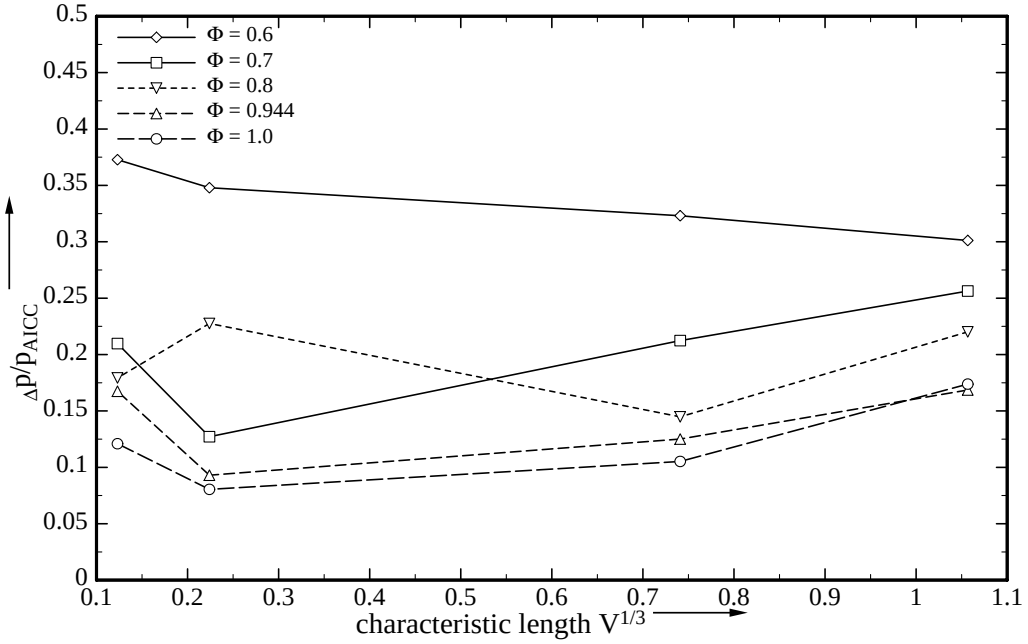

Figure 24: $\Delta p/p_{AICC}$ vs. characteristic length $V^{\frac{1}{3}}$ for methane-air mixtures; initial conditions p = 1 bar, T = 295 K.

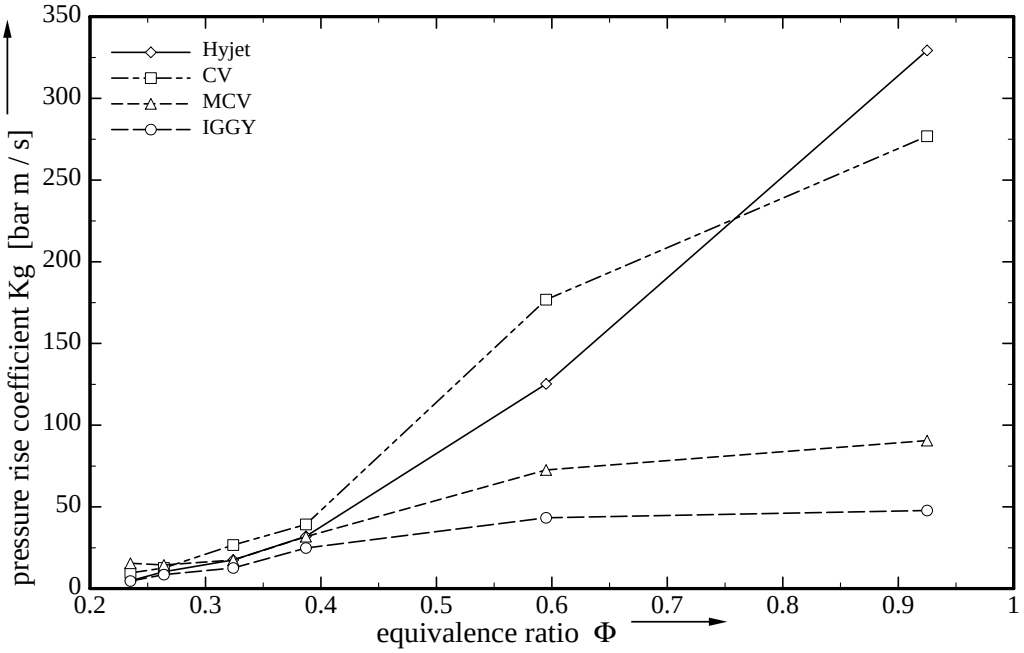

Figure 25: Pressure rise coefficient K_g for hydrogen-air mixtures; initial conditions p = 1 bar, T = 295 K.

average over a time window of 10 ms. The data samples are spread 1 ms apart. A simple first-order forward difference is then used to approximate the derivative.

The cube root of the vessel volume $V^{\frac{1}{3}}$ is chosen as characteristic length. The numerical values used can be found in Table 2. Several different methodes of presentation are used. Figures 25 through 28 catalogue K_g traces vs. the equivalence ratio ϕ. Each figure shows the result for one fuel. The same symbols are used for a given vessel in each plot. Data points of the same vessel are connected with the same type of line. The K_g-values increase with increasing equivalence ratio. The spread in K_g-values with vessel size increases with increasing equivalence ratio. Except for the experiments in IGGY, the K_g-values increase (same composition of the mixture assumed) with the vessel volume. The unexpected high K_g-values in the two small vessels (IGGY, MiniConvol) may result from inaccuracy in the filling process. The smaller the vessel and the smaller the amount of gas added to the vessel, the greater the uncertainties.

For the hydrogen-air mixtures in Fig. 25, the the K_g-values range from about 5 bar m/s for very lean mixtures to 330 bar m/s for nearly stoichiometric mixtures. For ϕ = 0.235 to ϕ = 0.387, the values are gathered together and only vary for up to 15 bar m/s. For a composition of ϕ = 0.925, these differences measure up to 352 bar m/s. The

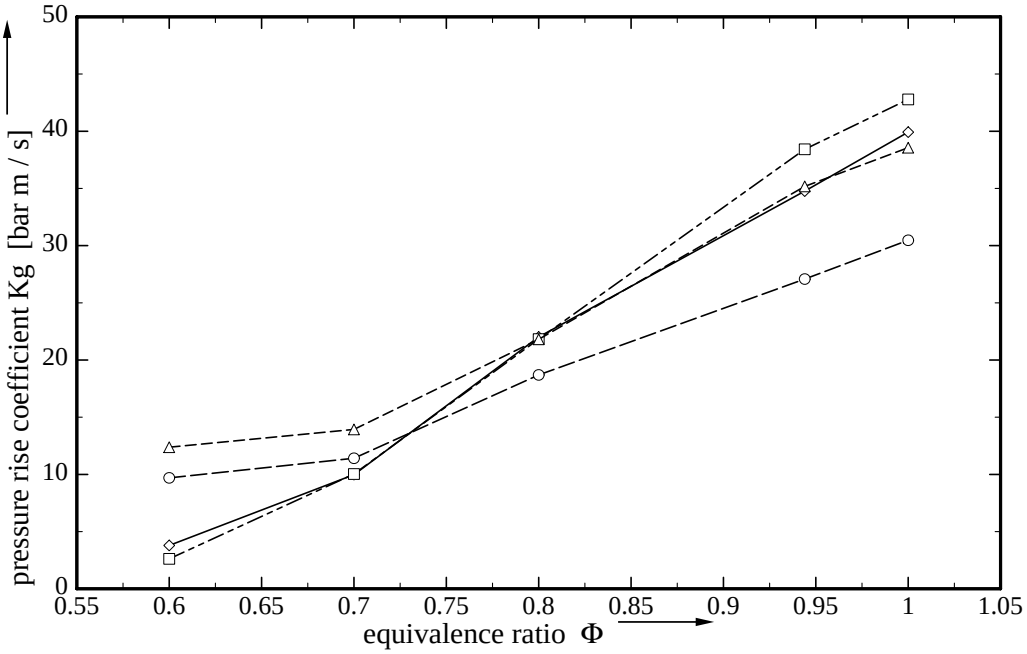

Figure 26: Pressure rise coefficient K_g for methane-air mixtures; initial conditions p = 1 bar, T = 295 K.

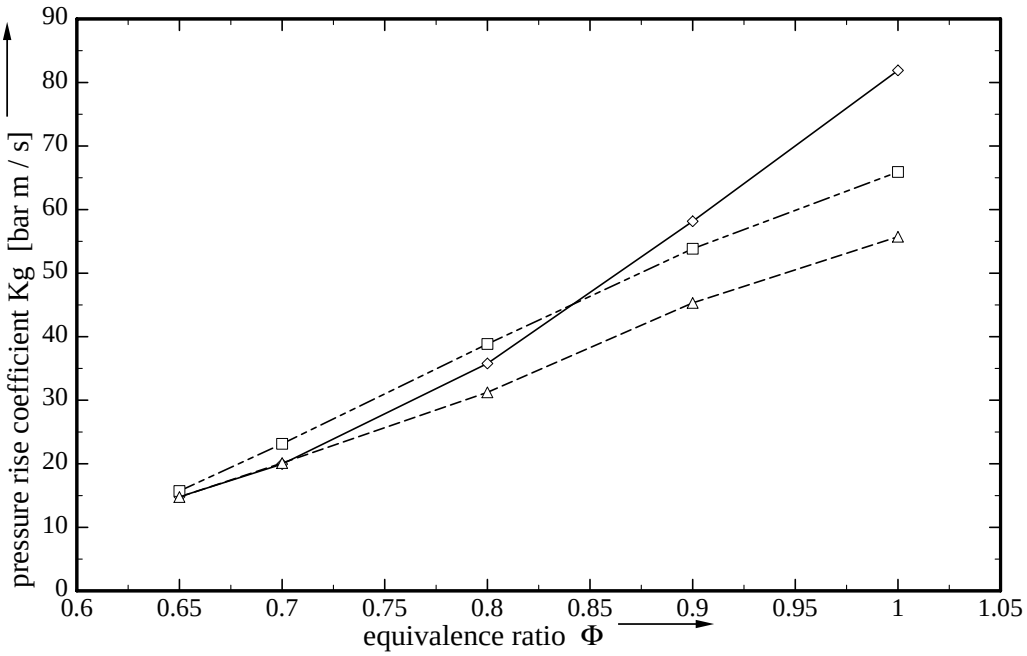

Figure 27: Pressure rise coefficient K_g for ethane-air mixtures; initial conditions p = 1 bar, T = 295 K.

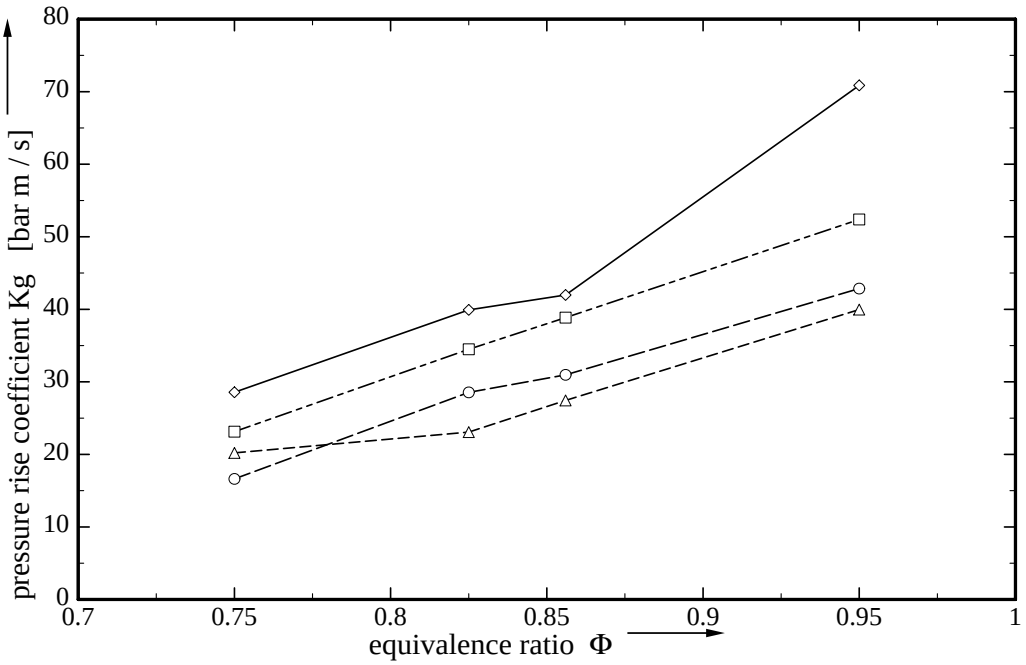

Figure 28: Pressure rise coefficient K_g for propane-air mixtures; initial conditions p = 1 bar, T = 295 K.

K_g-values for the methane-air mixture in Fig. 26 range from about 3-12 bar m/s for an equivalence ratio of $\phi = 0.6$ to about 30-43 bar m/s for stoichiometric mixtures. The K_g-values for ethane-air combustion in Fig. 27 range from about 15 bar m/s for $\phi = 0.69$ to 56-82 bar m/s for stoichiometric mixtures. The K_g-values for the propane-air mixtures in Fig. 28 range from about 16-28 bar m/s for $\phi = 0.75$ to about 40-71 bar m/s for $\phi = 0.95$.

Some adjustments are needed in order to compare these results with existing data from NFPA68 (1994). The vessels used in that report have a spherical shape and a centrally-located point of ignition. The characteristic length was the cube root of the vessel volume. Slightly rich (ϕ = 1.05-1.15) mixtures were used to get the largest possible value of K_g. To compensate for the differences in vessel shape, the characteristic length $V^{\frac{1}{3}}$ is replaced by the length l_{max} for computing K_g for the present study. This characteristic length l_{max} is defined as the distance from the point of ignition to the farthest point on wall of the vessel. For a spherical vessel, this length corresponds to the radius of the vessel. In tanks with other shapes, the distance can be calculated by simple trigonometric relations. The values of l_{max} for the different vessels are listed in Table 2. The 1180 l Hyjet vessel is affected most by this change due to the location of the ignition point.

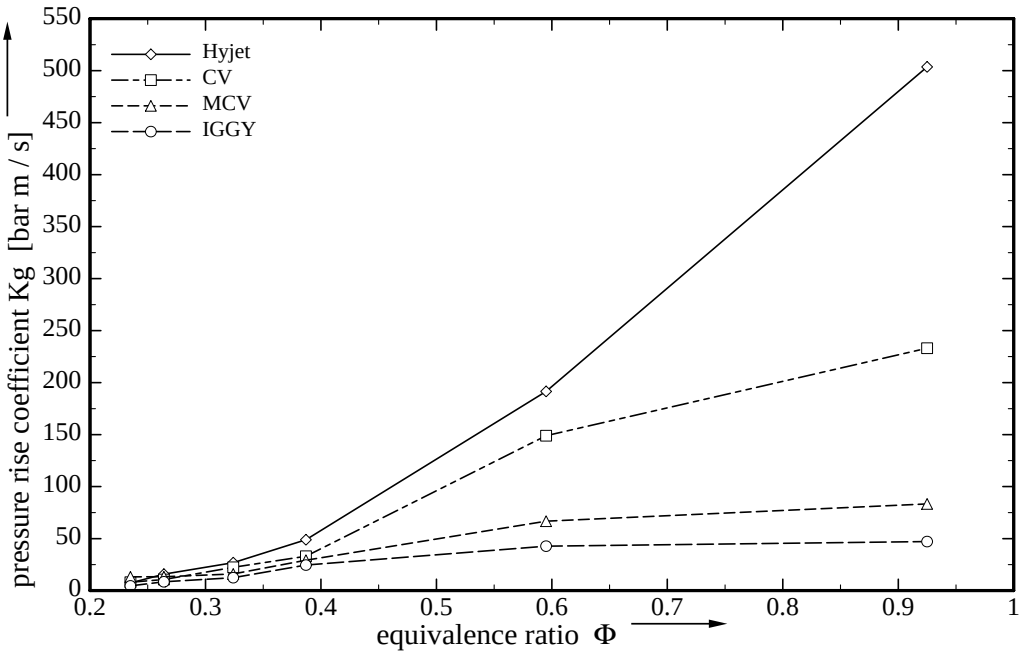

Figure 29: Pressure rise coefficient $K_{g,lmax}$ for hydrogen-air mixtures; initial conditions p = 1 bar, T = 295 K.

The modified K_g-value is thus defined as

$$K_{g,lmax} \equiv \left(\frac{dp}{dt}\right)_{max} \quad l_{max}. \tag{27}$$

The resulting values of the pressure rise coefficient $K_{g,lmax}$ can be seen in Figs. 29-32. The pressure rise coefficient now increases with the vessel volume for all fuels, except propane in IGGY, and all equivalence ratios using this definition of K_g .

Figure 33 compares K_g and $K_{g,lmax}$ values of this study with results from NFPA68 (1994). Only data from the stoichiometric mixture or the mixture nearest to $\phi = 1.0$ are used. The lines are first-order fits to the NFPA68 data points. It can be observed that the variation of K_g-values is rather high in the NFPA68 report. This variation is especially true for the hydrogen data, but is also true for the propane, where for one vessel three K_g-values of 275, 345 and 390 bar m/s are given. Compared to the NFPA68, relatively small vessels are used in the present study. The K_g values in NFPA68 are always larger than those measured in the present study for corresponding fuel type and vessel size. Several things may account for this difference. First, the composition of the mixtures in this study have a maximum equivalence ratio of $\phi = 1$; in NFPA68, slightly

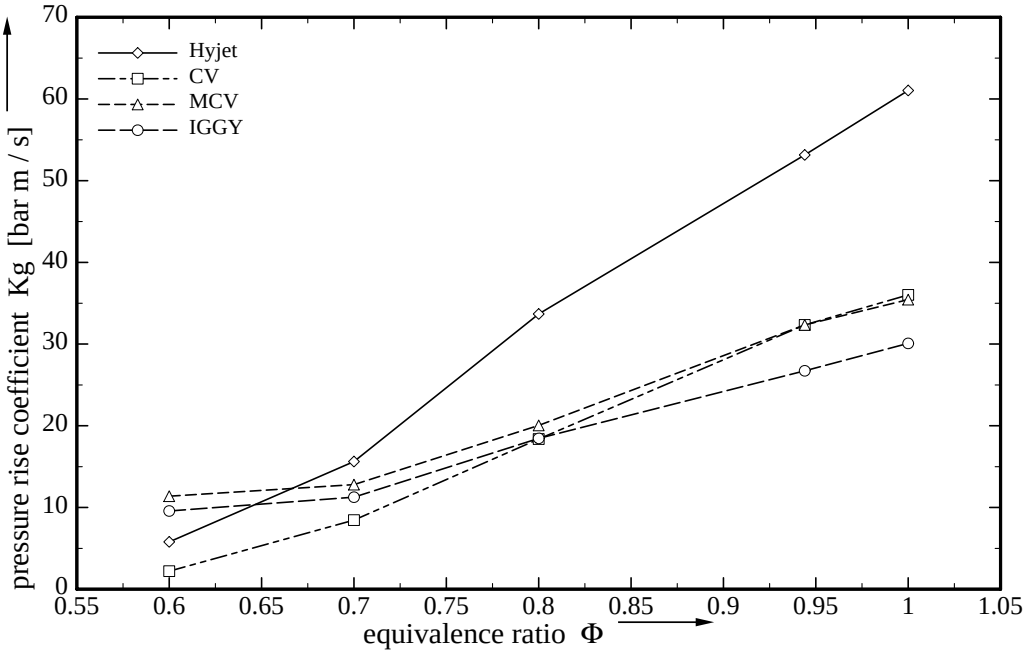

Figure 30: Pressure rise coefficient $K_{g,lmax}$ for methane-air mixtures; initial conditions p = 1 bar, T = 295 K.

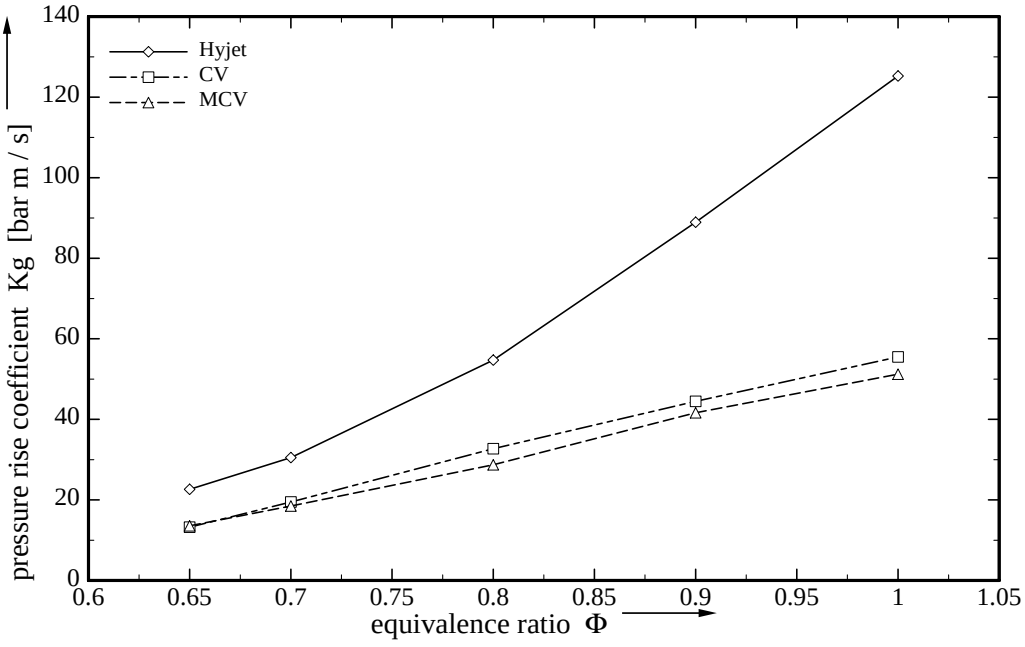

Figure 31: Pressure rise coefficient $K_{g,lmax}$ for ethane-air mixtures; initial conditions p = 1 bar, T = 295 K.

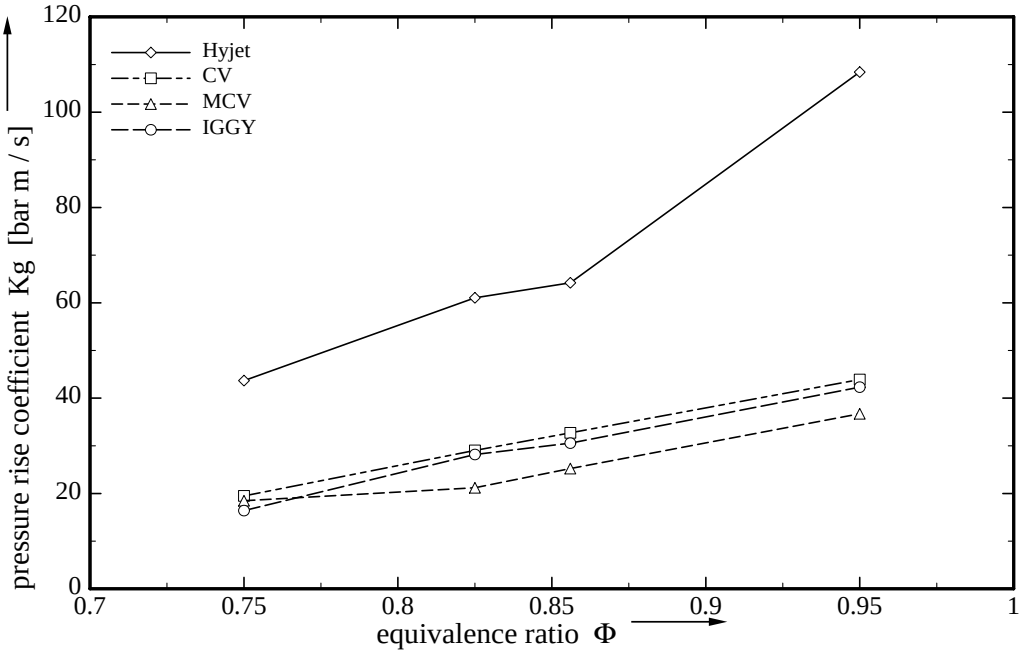

Figure 32: Pressure rise coefficient $K_{g,lmax}$ for propane-air mixtures; initial conditions p = 1 bar, T = 295 K.

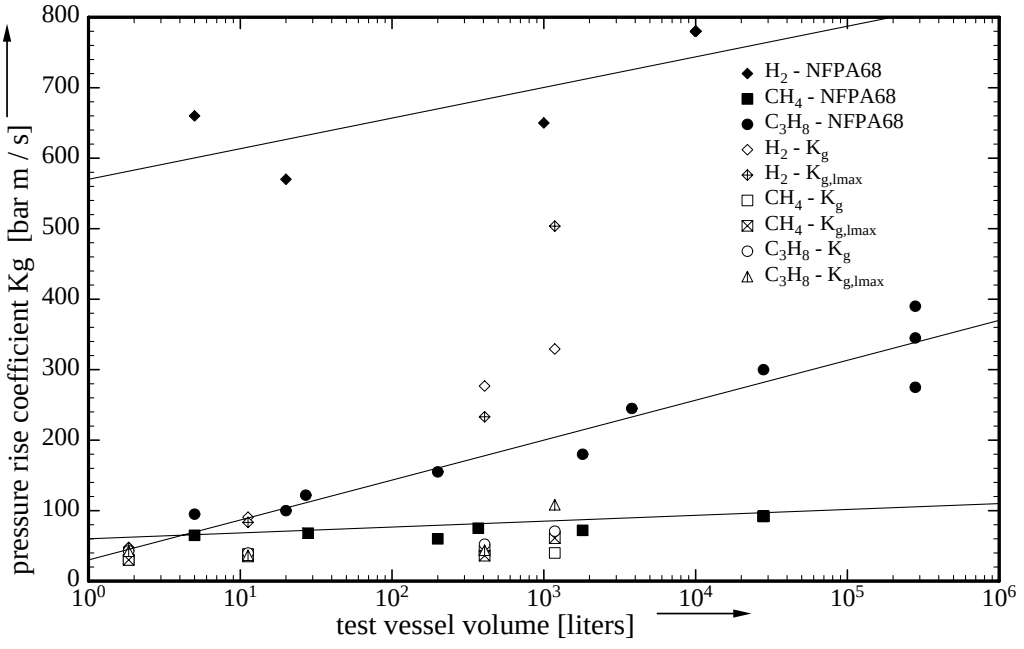

Figure 33: Comparison of stoichiometric pressure rise coefficients K_g from this study with NFPA68 data and a first order fit to the NFPA68 data.

rich mixtures are used. This composition results in higher pressure time derivatives and consequently in higher K_g. Second, the hardware in NFPA68 differs from that used in this investigation. Vessel shape, point of ignition and the related energy losses will influence the results. Third, as described in NFPA68 (1994), K_g measurements should be made in vessels of at least 5 l in volume, preferentially 20 l or larger.

Although the experimental data of this study have lower values due to the reasons mentioned above, it can still be observed that the K_g-values increase with the vessel size. This increase is particularly true for the hydrogen and propane data. For methane the increase of K_g with the volume is smaller, but still observable. Though the numerical values vary, this qualitative statement is true for both this study and the NFPA68 report.

The Reynolds number, Re, is defined in Chapter 2.3.2. As it characterizes the state of a flow, Re is used to compare the differnt combustion phenomena. The Reynolds numbers tend to be small for small vessels and very lean mixtures. Re increases with vessel size and as the mixture composition shifts towards stoichiometric.

Figures 34 to 37 show the K_g-value vs. the Reynolds number. Note that the Reynolds number for one type of fuel changes with the equivalence ratio and with the size of the vessel.

To summarize these figures, the K_g-values of all experiments are shown in Fig. 38 for the conventional definition of K_g, as well as in Fig. 39 for the modified $K_{g,lmax}$ definition. Note that the choice of l_{max} affects both the pressure rise coefficient and the Reynolds number.

It can be observed that all K_g-values increase with increasing Reynolds number. Most of the values are in a region between 10 and 100 bar m/s. To allow more general conclusions, the K_g-value should be modified to a proper scientific parameter, which should be nondimensional and depend on nondimensional parameters. Consequently this coefficient should be independent from type and equivalence ratio of the mixture as well as from the volume of the test vessel. As the results for the $K_{g,lmax}$ do not vary too much from the classical values, from now on only $V^{\frac{1}{3}}$ will be used as characteristic length. After investigating the burning velocities in Chapter 5.1.3, modifications of the pressure rise coefficient will be discussed in Chapter 5.1.4

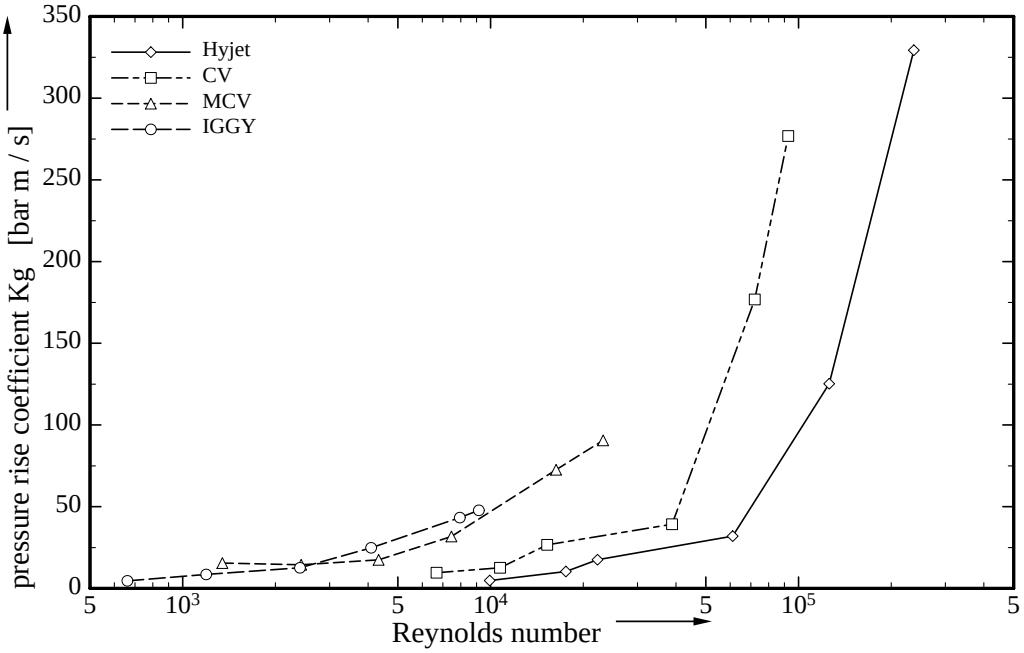

Figure 34: Pressure rise cofficient K_g for hydrogen-air mixtures; initial conditions p = 1 bar, T = 295 K.

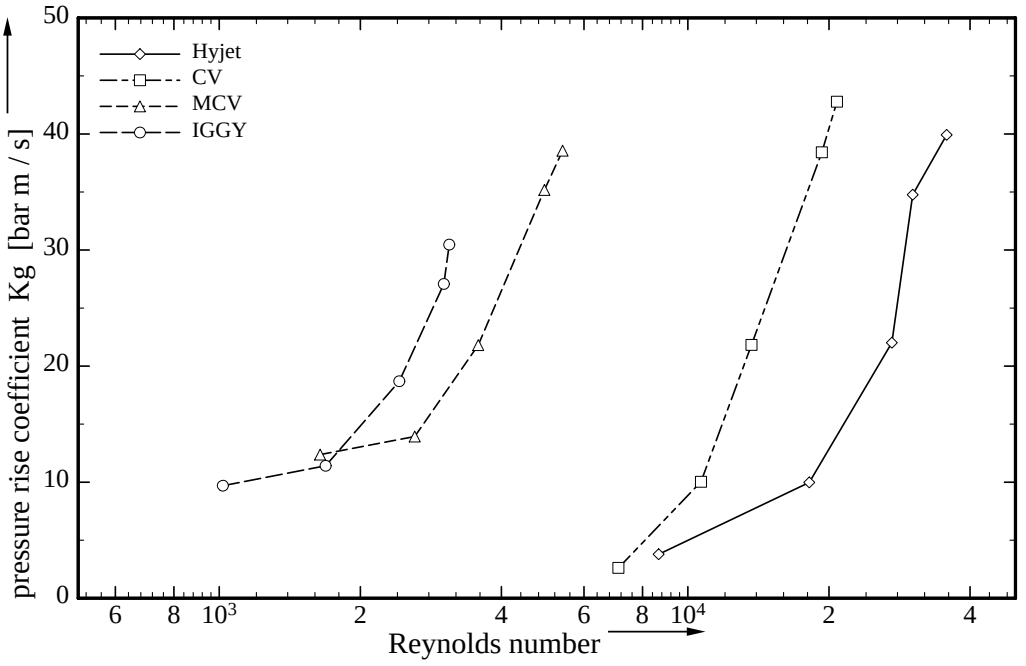

Figure 35: Pressure rise cofficient K_g for methane-air mixtures; initial conditions p = 1 bar, T = 295 K.

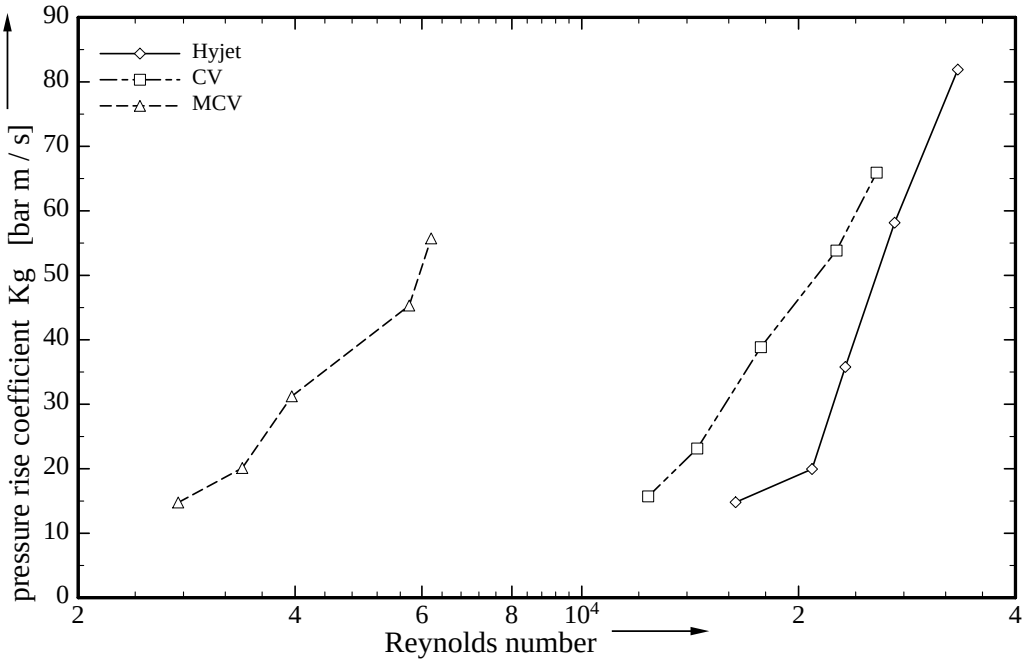

Figure 36: Pressure rise cofficient K_g for ethane-air mixtures; initial conditions p = 1 bar, T = 295 K.

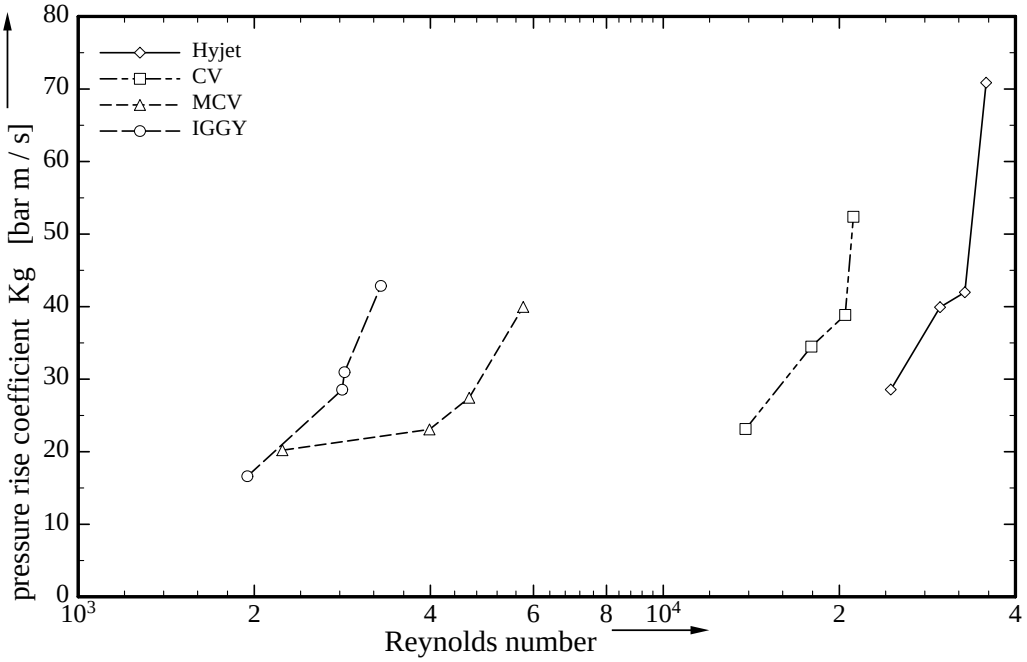

Figure 37: Pressure rise cofficient K_g for propane-air mixtures; initial conditions p = 1 bar, T = 295 K.

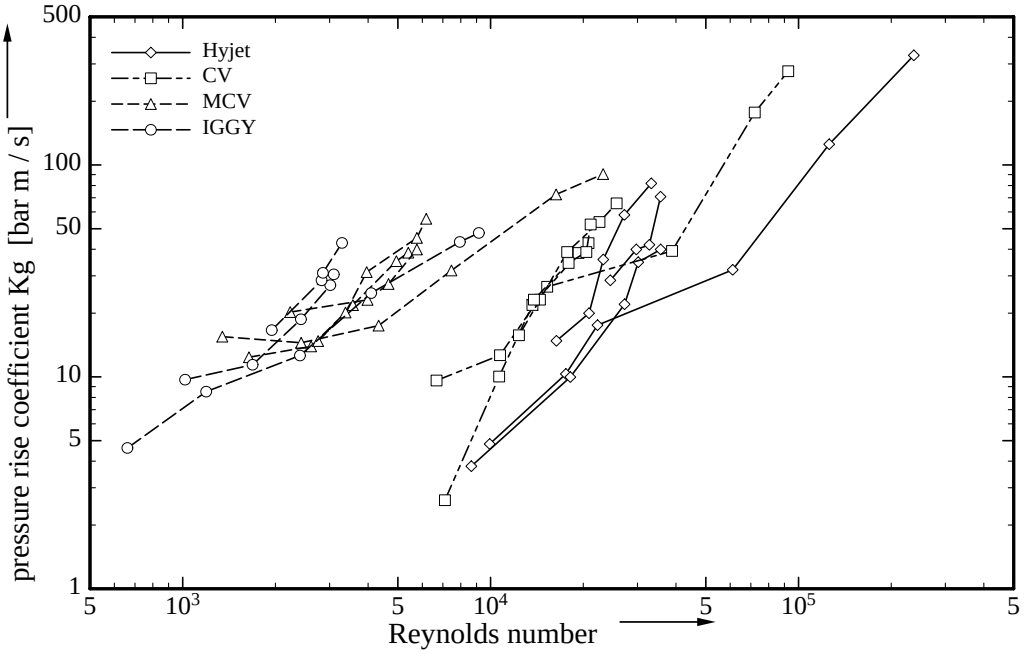

Figure 38: Pressure rise coefficients K_g of all experiments (all fuels, all vessels); initial conditions p = 1 bar, T = 295 K.

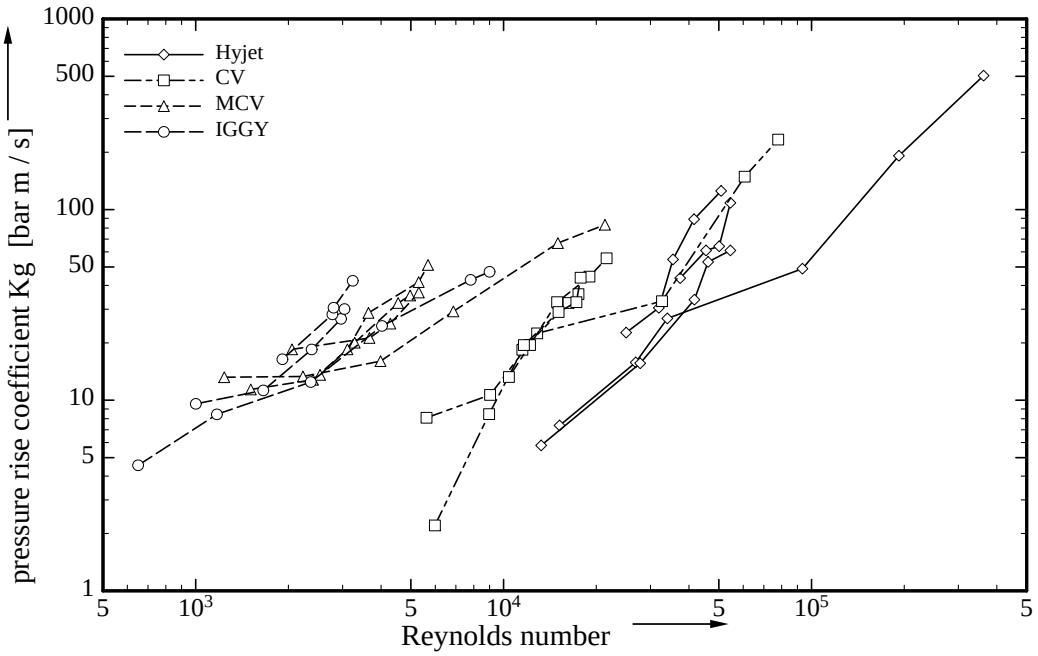

Figure 39: Pressure rise coefficients K_g of all experiments (all fuels, all vessels) based on l_{max}; initial conditions p = 1 bar, T = 295 K.

5.1.3 Burning Speeds

As mentioned in Chapter 2.3.1, the laminar burning speed is a fundamental property of a combustible mixture and is primarily dependent upon the mixture's thermal diffusivity, reaction mechanism, and heat of combustion. Using the method discussed in Chapter 2.5.3, the effective burning speed is calculated for all experiments. The results can be seen in Figs. 40 to 43. Each figure shows the burning speed for one type of fuel vs. the equivalence ratio. The corresponding values from literature are shown as a second-order fit to the original data.

All figures have in common that most of the present values for S_u are higher than the literature values. The difference between measured values and the ones from literature increases with increasing equivalence ratio. This difference is particularly true for larger vessels as well as for experiments with high laminar burning speeds. These burning speeds may be high due to the type of fuel or the concentration used. Consequently, S_u values for stoichiometric hydrogen-air combustion in Hyjet and Convol differ the most from the corresponding literature data. In these two particular cases, measured values differ with a factor of 1.5 and 2.2, respectively. The phenomena can be explained by the fact that the period where the flame is considered to be laminar is very short. Turbulence soon occurs and perturbs the spherical flame front. This perturbation results in an increase of the flame surface and a tremendous increase of effective burning speed. This increase is particularly true for the larger vessels, where the turbulent flame can accelerate longer and thus reach higher speeds. These effects are increased by flame instabilities and the associated cellular flames (especially for hydrogen). Depending on the period of time examined, the results can thus be the laminar burning speed or an effective "turbulent" burning speed. This effective burning speed is an average of the laminar and the turbulent burning speed.

Figure 40 shows the burning speeds for hydrogen-air mixtures. The speeds range from 10 cm/s for $\phi = 0.24$ in IGGY and MiniConvol to up to about 530 cm/s for $\phi = 0.93$ in Hyjet. The burning speed increases with increasing equivalence ratio for all vessels. For $\phi = 0.24$ to $\phi = 0.32$, the experimental data do not vary much from the literature values. The maximum difference is noted in IGGY and is about 10 cm/s. The reason may be small inaccuracies in preparing the gas mixture. For higher equivalence ratios, the measured laminar burning speeds for the two large vessels differ more and more from the literature values. At an equivalence ratio of $\phi = 0.93$, these differences are about 290 cm/s in Hyjet and 130 cm/s in Convol. For the 1.84 l and the 11.25 l vessels, experimental

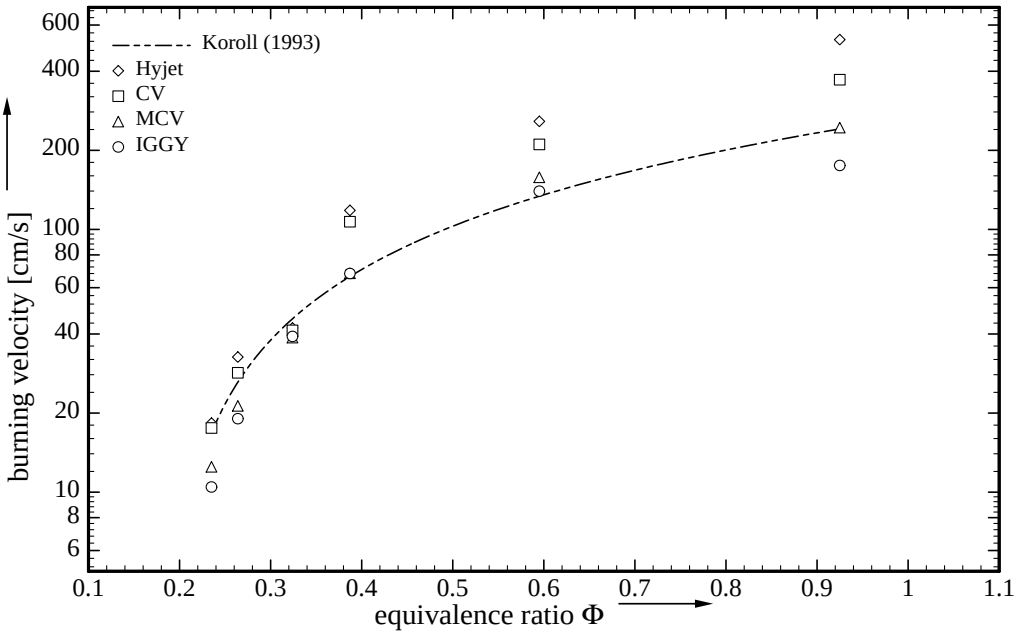

Figure 40: Burning speeds for hydrogen-air mixtures; initial conditions p = 1 bar, T = 295 K.

data are in reasonable agreement with the measurements of Koroll et al. (1993).

The burning speeds of methane-air mixtures are shown in Fig. 41. Values range from 13 cm/s for very lean mixtures in MiniConvol to about 64 cm/s for stoichiometric mixtures in Hyjet. Again, the leaner the mixture, the closer the experimental data are to the literature values. For $\phi = 0.6$, the maximum difference is only 3 cm/s. For ϕ= 1, the differences are 9 cm/s in Convol and 20 cm/s in Hyjet. For equivalence ratios higher than $\phi = 0.7$, burning speeds increase with the vessel size. The rather high values for IGGY are an exception, which is apparently due to systematic differences in flame propagation in very small vessels.

Figure 42 shows the burning speeds for lean to stoichiometric ethane mixtures. The values for S_u range from 22 cm/s for ϕ=0.688 in MCV to about 63 cm/s for the stoichiometric mixture in Convol. The gap between experimental results and literature data increases with increasing equivalence ratio. For Convol, the difference is about 5 cm/s for $\phi = 0.688$ and 17 cm/s for $\phi = 1$. The burning speeds for Convol are higher than for comparable conditions in Hyjet.

The burning speeds of propane-air mixtures are shown in Fig. 43. Literature values range from 25 cm/s for $\phi = 0.75$ to 45 cm/s for $\phi = 0.95$. The corresponding experimental

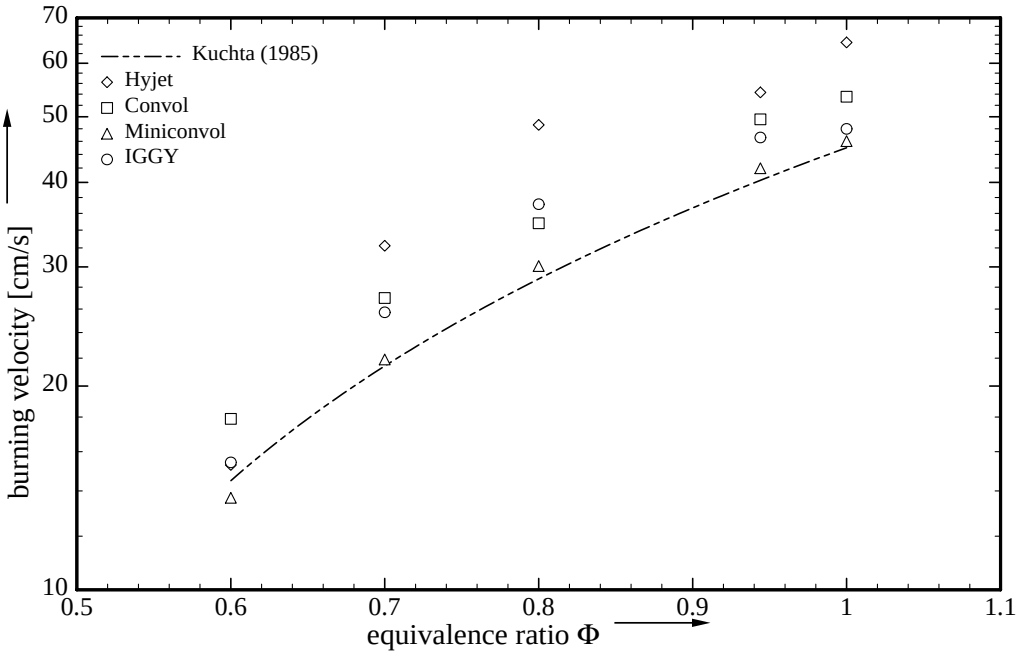

Figure 41: Burning speeds for methane-air mixtures; initial conditions p = 1 bar, T = 295 K.

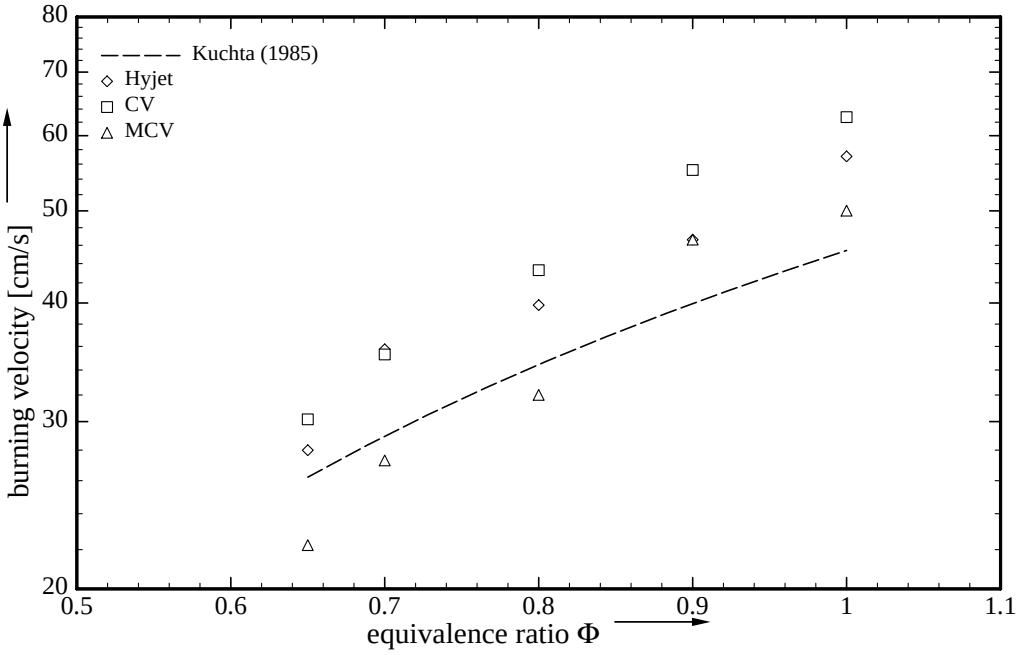

Figure 42: Burning speeds for ethane-air mixtures; initial conditions p = 1 bar, T = 295 K.

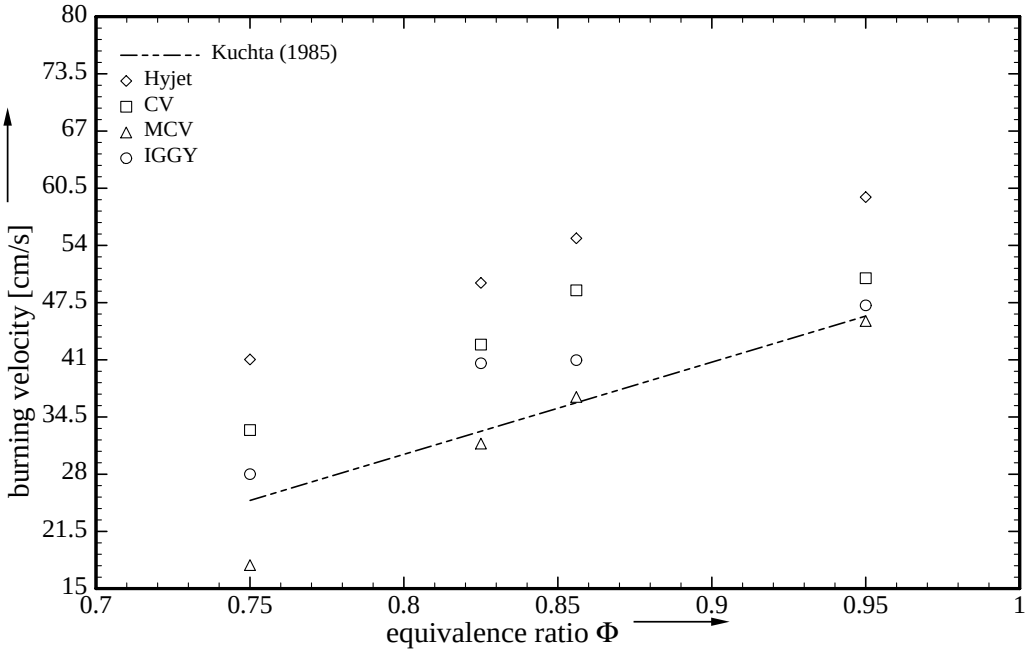

Figure 43: Burning speeds for propane-air mixtures; initial conditions p = 1 bar, T = 295 K.

data vary to some extent from these values. For $\phi = 0.75$, the laminar burning speed for Hyjet measures 41 cm/s, about 65% more than the literature value. For $\phi = 0.95$, the variation for Hyjet decreases to about 30%. Nevertheless, the increase of laminar burning speed with equivalence ratios is similar for all vessels. Except for MiniConvol, all experimental values are higher than the literature values, but traces have similar slopes.

5.1.4 Dimensionless Pressure Rise Coefficient K'_g

The objective is to determine a universal pressure rise coefficient which is independent of type of fuel, concentration of the mixture, and size of the vessel. This parameter would enable the estimation of the maximum rate of pressure increase in any vessel and could serve as an improved guideline for the construction of venting systems (NFPA68 1994). The results of the pressure analysis section 2.5.3 are used as a basis to transform the pressure rise coefficient into a dimensionless parameter. Equation 18 indicates that the appropriate experimental parameters to use are the burning speed $S_{u,exp.}$ and the maximum pressure rise $(\Delta p)_{max}$.

The dimensionless pressure rise coefficient K'_g is defined as

$$K'_g \equiv \left(\frac{dp}{dt}\right)_{max} V^{\frac{1}{3}} \frac{1}{(\Delta p)_{max}} \frac{1}{S_{u,exp.}}, \tag{28}$$

where $(\frac{dp}{dt})_{max}$ is the maximum pressure time derivative, V, the vessel volume, $(\Delta p)_{max}$, the maximum pressure rise coefficient, and $S_{u,exp.}$, the experimentally determined effective burning speed. K'_g is thus a nondimensional parameter and is expected to be associated to other nondimensional parameters as the Reynolds number, the Froude number, Fr, and the Lewis number, Le. Furthermore, the definition of K'_g implies a dependence on the fuel type, the equivalence ratio of the fuel, and the geometry of the vessel.

$$K'_g = (Re, Fr, Le, \text{fuel}, \Phi, \text{geometry})$$

In Fig. 44, K'_g vs. the Reynolds number, Re, is shown for all of the fuels and equivalence ratios. The Reynolds number in this case is defined as

$$Re = \frac{S_{u,exp.}\, V^{\frac{1}{3}}}{\nu}\ , \tag{29}$$

where ν is the kinematic viscosity of the reactants, $S_{u,exp.}$, the effective burning speed, and V, the vessel volume.

Most of the data points are in the range 7 <K'_g < 14. Compared to the classical pressure rise coefficient K_g in Fig. 38 where data points are in the range 20 bar m/s <K'_g < 100 bar m/s, this definition of K'_g results in a much smaller range of scatter. The minimum and maximum values for K_g are 2.6 bar m/s and 239 bar m/s, respectively. For K'_g, these limits range from 4.3 to 48. It can be concluded that the majority of data points for K_g are located in an interval that is 34% of the total range. For K'_g, the data points are located in an interval that is only 16% of the total range.

The scatter of K'_g can be further reduced by removing the data from the leanest fuel-air mixtures for hydrogen and methane. The flame speeds are very low for these mixtures and we expect that these flames will be strongly influenced by buoyancy. As Fig. 44 indicates, these data points are substantially higher than the majority of the other values. Consequently the data points for the 9% hydrogen ($\Phi = 0.24$) and for the 5.93% methane ($\Phi = 0.6$) are eliminated. The results are shown in Fig. 45. 80% of the data points are located in the range 8 <K'_g < 16 . The mean value of K'_g is 12.

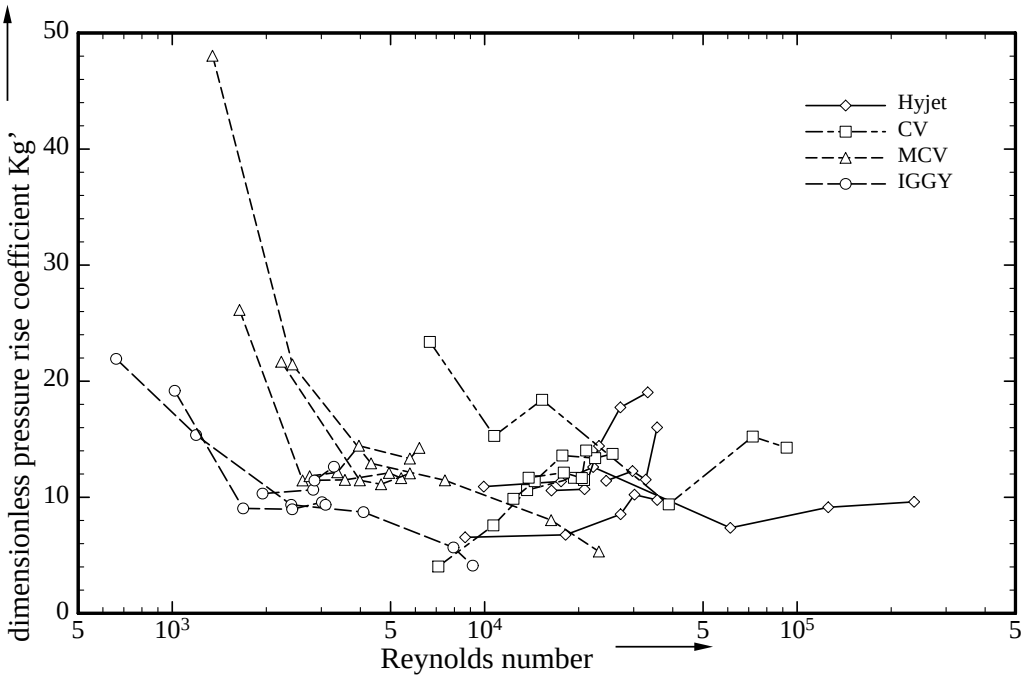

Figure 44: Dimensionless pressure rise coefficient K'_g; initial conditions p = 1 bar, T = 295 K.

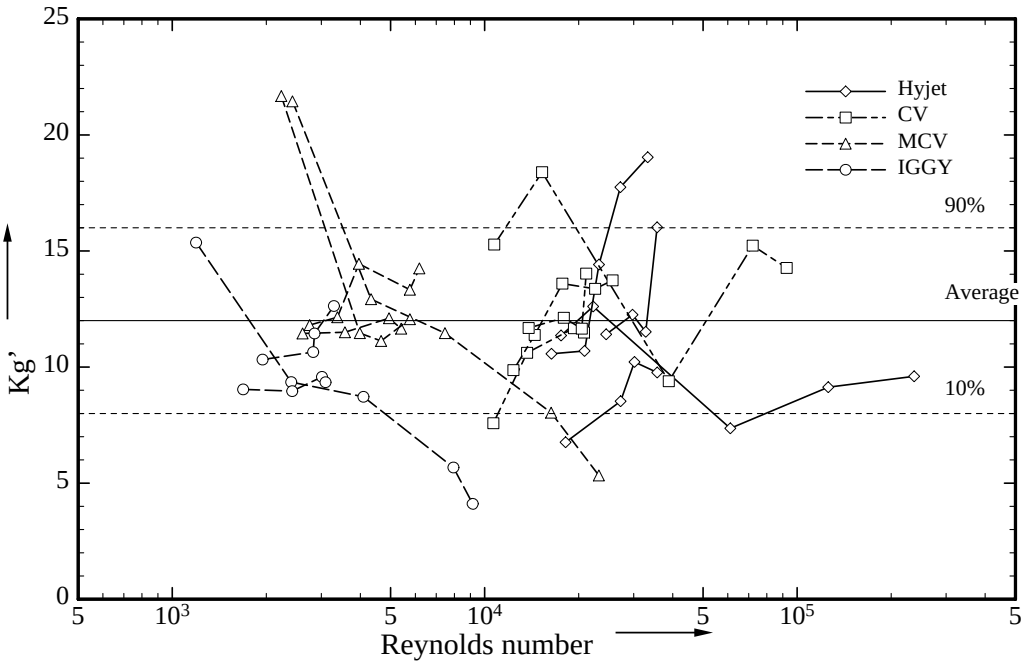

Figure 45: Dimensionless pressure rise coefficient K'_g with very lean mixtures eliminated; initial conditions p = 1 bar, T = 295 K.

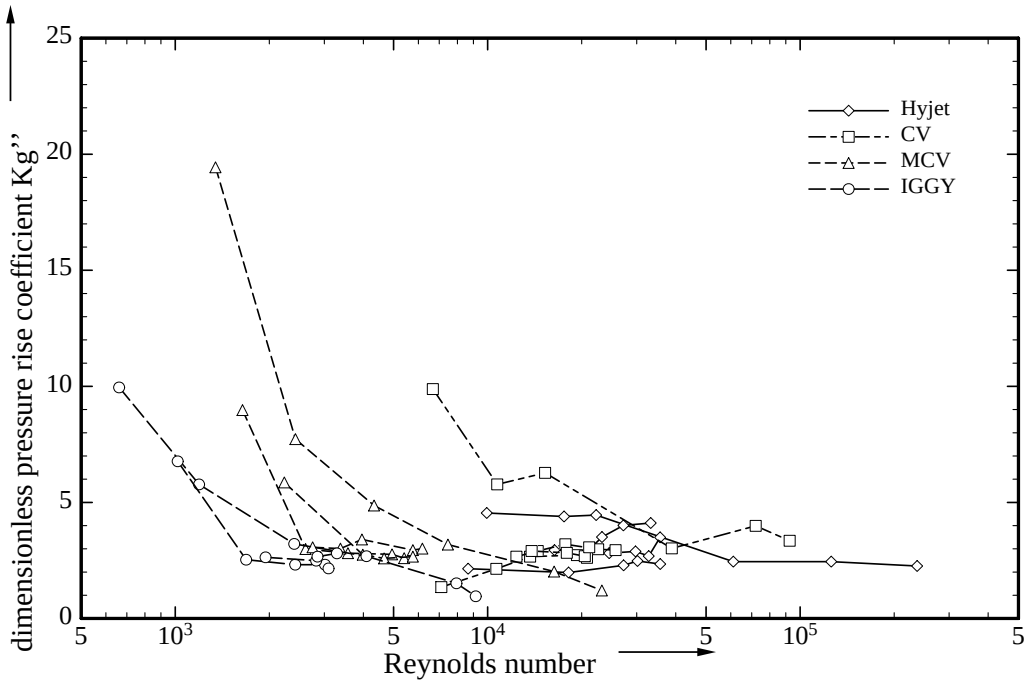

Figure 46: Dimensionless pressure rise coefficient K''_g; initial conditions p = 1 bar, T = 295 K.

An attempt to reduce the scatter even further is shown in Fig. 46. This attempt is based on the pressure analysis presented in Section 2.5.3. The dimensionless pressure rise coefficient K''_g is defined as

$$K''_g \equiv \frac{1}{\left(\frac{p_{max}}{p_\circ}\right)^{\frac{1}{\gamma}}} \quad \left(\frac{dp}{dt}\right)_{max} \quad V^{\frac{1}{3}} \quad \frac{1}{(\Delta p)_{max}} \quad \frac{1}{S_{u,exp.}}. \tag{30}$$

The correction factor $(p_{max}/p_\circ)^{\frac{1}{\gamma}}$ is used due to Eqn. 21, where it is related to maximum of the geometry function F. While Fig. 46 shows all data points, the data from the leanest hydrogen and methane mixtures are removed in Fig. 47. Neglecting these data points, 80% of the remaining data points are located in the range 2 <K''_g < 4.5 . The mean value of K'_g is 3. The scatter is minimized and the new definition of a pressure rise coefficient K''_g delivers a significant reduction of the scatter.

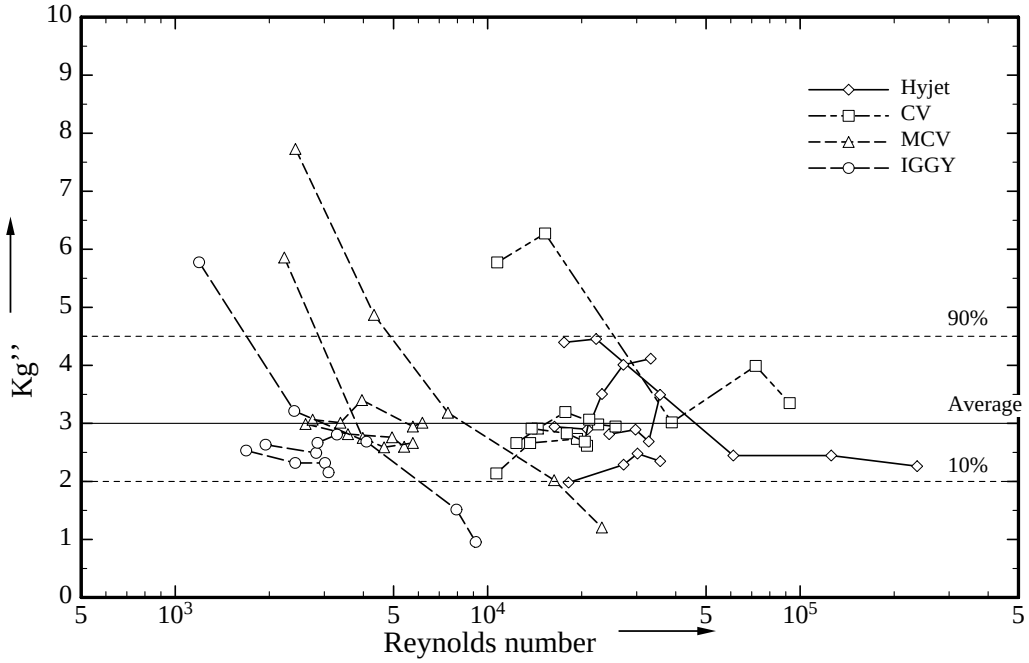

Figure 47: Dimensionless pressure rise coefficient K_g'' with very lean mixtures eliminated; initial conditions p = 1 bar, T = 295 K.

5.2 Ignition Energy Measurements

The results from the ignition energy experiments are discussed in this Chapter. Experiments with hexane, Jet A fuel, Jet A fuel simulant, and 3 specified Jet A samples are carried out at initial temperatures from 20 to 50°C. The ignition energies used range from 1.0 mJ to 100 J. The experiments are performed at initial pressures of 58.5 kPa, 83.5 kPa, and 100 kPa for the four different Jet A fuels, the Jet A fuel simulant and hexane, respectively. The initial pressure of 58.5 kPa corresponds to the atmospheric pressure at a height of 13800 feet, the altitude at which the TWA800 accident occurred. The pressure of 83.4 kPa is chosen to have the same initial conditions as at the experimental test site in Denver, Colorado, where 1/4-scale experiments of the center wing tank were carried out. Hexane experiments are carried out at initial pressures of 100 kPa to correspond to previous work (Shepherd et al. 1998).

Problems of flammability and ignition energy are closely related since the determination of flammability is tied to a specific ignition source and energy. At present there is no firm theoretical basis on which to predict the minimum ignition energy and the primary method is to carry out experiments. The present experiments used two ignition sources: sparks and hot filaments. The electrical circuit used for the ignition energy measurements is similar to the circuit in Fig. 9. The amount of ignition energy is determined by the use of different capacitors. The capacitances range from 0.032 nF to 1300 μF .

The Jet A fuel simulant is a mixture of propane and hydrogen with a volume ratio of 1:5. The advantage of a gaseous simulant is that it enables experiments in unheated vessels and at higher pressures. This fuel simulant was used in the 1/4-scale field tests carried out for the TWA800 accident investigation (Shepherd et al. 1998). Details on the choice of the fuel are given in Chapter 5.2.2.

5.2.1 Vapor Pressure

Jet A is a complex multi-component mixture of several hundred species: n-alkanes, branched alkanes, cyclic alkanes, olefines, and aromatics. It is very time consuming to determine the exact composition of a particular sample of Jet A. The composition may vary, depending on the way the fuel is refined, stored, and handled. The vapor pressure of a complex mixture like Jet A is the sum of the vapor pressures of the pure components, weighted by their individual mole fractions and activity coefficients. The vapor pressure of the fuel strongly depends on the temperature. Flight testing demonstrated that the

temperatures within the CWT ranged between 38 and 60°C, depending on the location of measurement. Consequently, all investigations concerning flammability are based on this temperature range.

5.2.2 Combustion Pressure

The fuel simulant was chosen on the basis of laboratory testing comparing explosions of Jet A vapor in air at a simulated altitude of 14 kft with a propane/hydrogen air mixture at the pressure of the test site (83.4 kPa). After a series of experiments (Shepherd et al. 1997b) in the Explosion Dynamics Laboratory's Hyjet facility, a combination of fuels was found that approximately simulated the pressure-time characteristics of Jet A at 50°C.

A comparison between the simulant mixture of 1.4% propane, 7% hydrogen and 91.6% air and Jet A is shown in Fig. 48. Analysis of these pressure traces indicates that peak pressure rise is slightly larger for the simulant (Δp_{max} = 3.65 bar) than for the Jet A (Δp_{max} = 3.36 bar) However, the simulant has a slightly lower effective burning speed (as determined by the $\Delta p^{1/3}$ analysis discussed in Shepherd et al. 1997a) of 52 cm/s as compared to 60 cm/s for the Jet A. Detailed information on this subject can be found in Shepherd et al. (1997b).

The mixtures studied in this diploma-thesis have fuel concentrations of 6, 7 and 8.4 vol.%. The fuel simulant experiments served as a primary study to see how the fuel-air mixture behaves before tests in the quarter scale tank were performed. Key data of the experiments are tabulated in Appendix B.

Figure 49 shows typical pressure and temperature histories of a 8.4% fuel, 91.6% air-mixture in MiniConvol. The initial conditions are p_0 = 83.4 kPA and T_0 = 295 K. The ignition of the mixture is initiated by a spark with an energy of about 8 Joules. The corresponding Schlieren video segments can be seen in Table 4.

The first picture (a) shows a view through the 117 mm diameter windows of the MiniConvol vessel before ignition. As the optical path of the vessel is aligned with with the one of the Convol vessel, two pairs of electrodes can be seen. Only the lower ones are of interest for this experiment. The run number (lower right corner) and the time (center, bottom line) can be seen.

The time is set to zero and starts with triggering the fire button. The second frame (b) shows the same view about 20 ms after ignition takes place. The flame ball has spherical shape; it propagates undisturbed, symmetrically in all directions. No signs of buoyancy

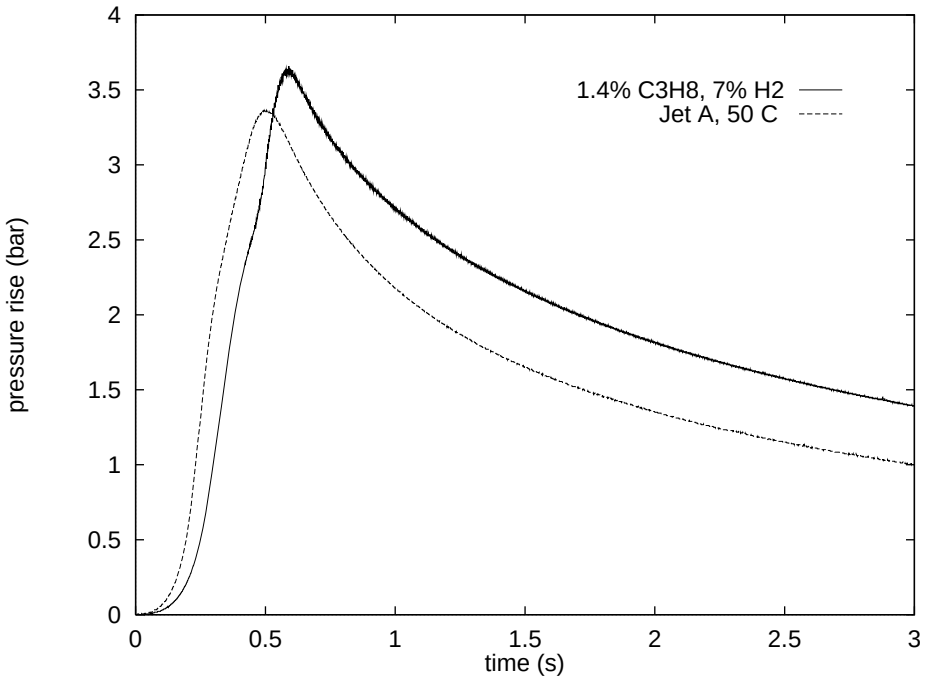

Figure 48: Comparison of combustion tests using LAX Jet A at 50°C, mass loading of 3 kg/m^3 and 0.585 bar, and propane/hydrogen (1.4%/7%) at 25°C and 0.83 bar in the Hyjet Facility (1180 liters), both with spark ignition, Shepherd et al. (1997b).

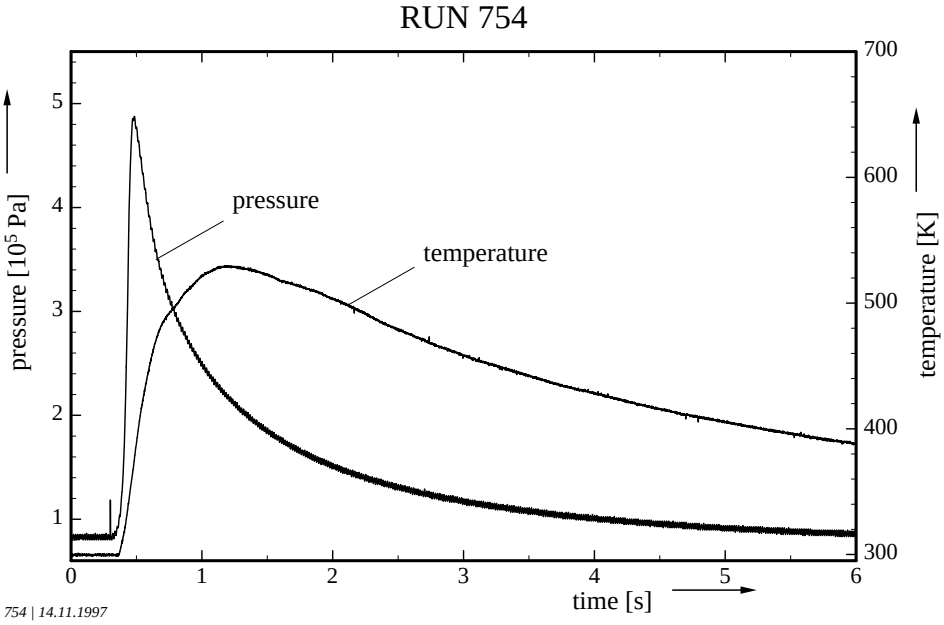

Figure 49: Pressure and temperature vs. time for 1.4% H_2, 7%C_3H_8, 91.6 % air at initial conditions of p_0 = 83.4 kPA, T_0 = 295 K in MiniConvol, ignition energy = 8 J.

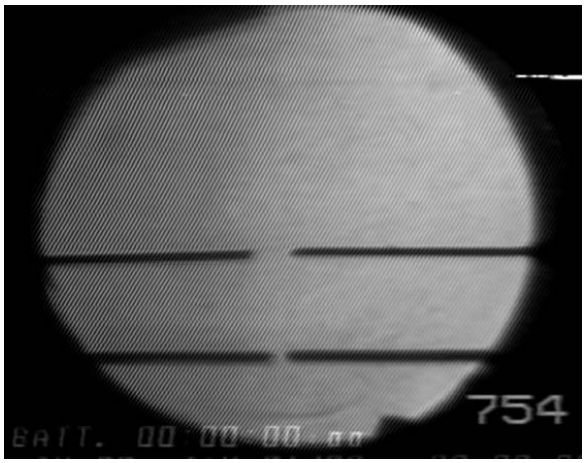

(a)

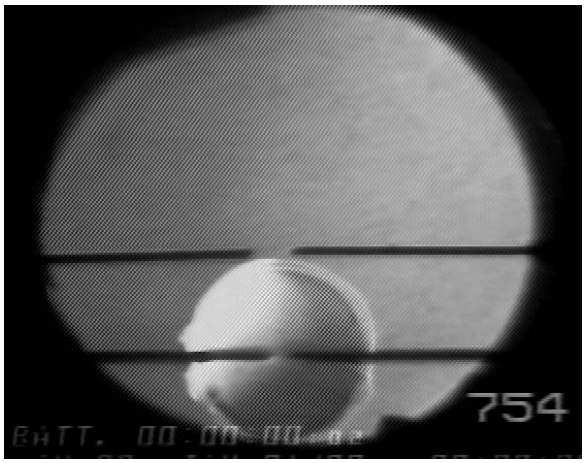

(b)

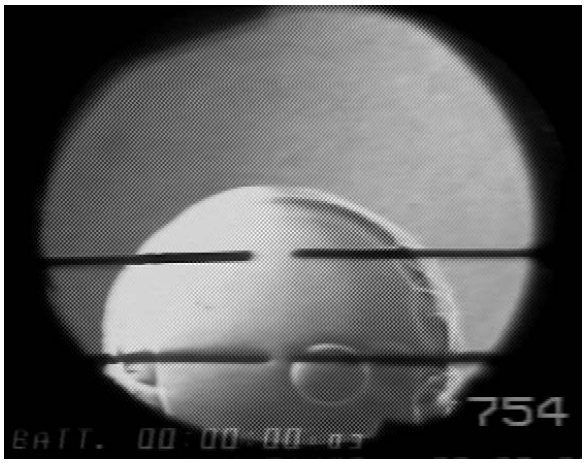

(c)

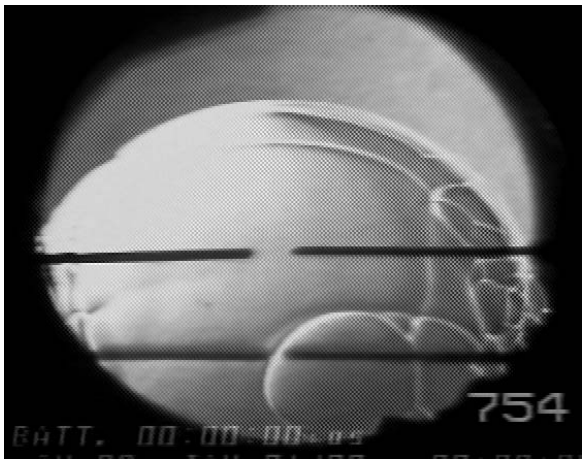

(d)

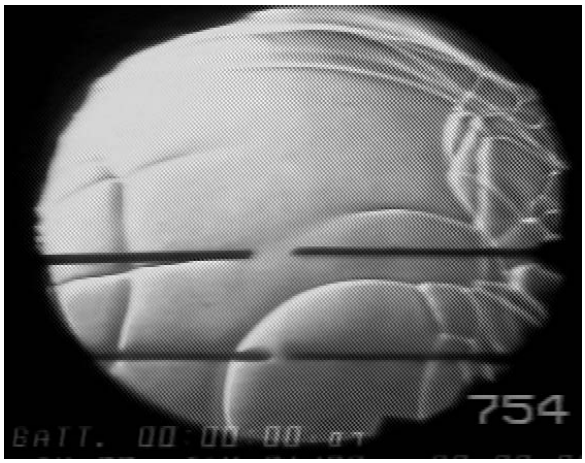

(e)

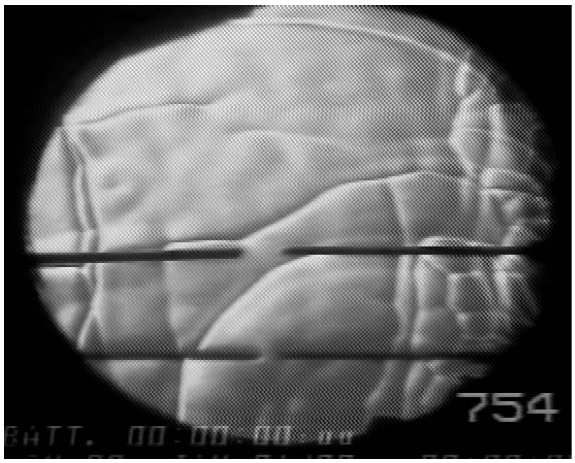

(f)

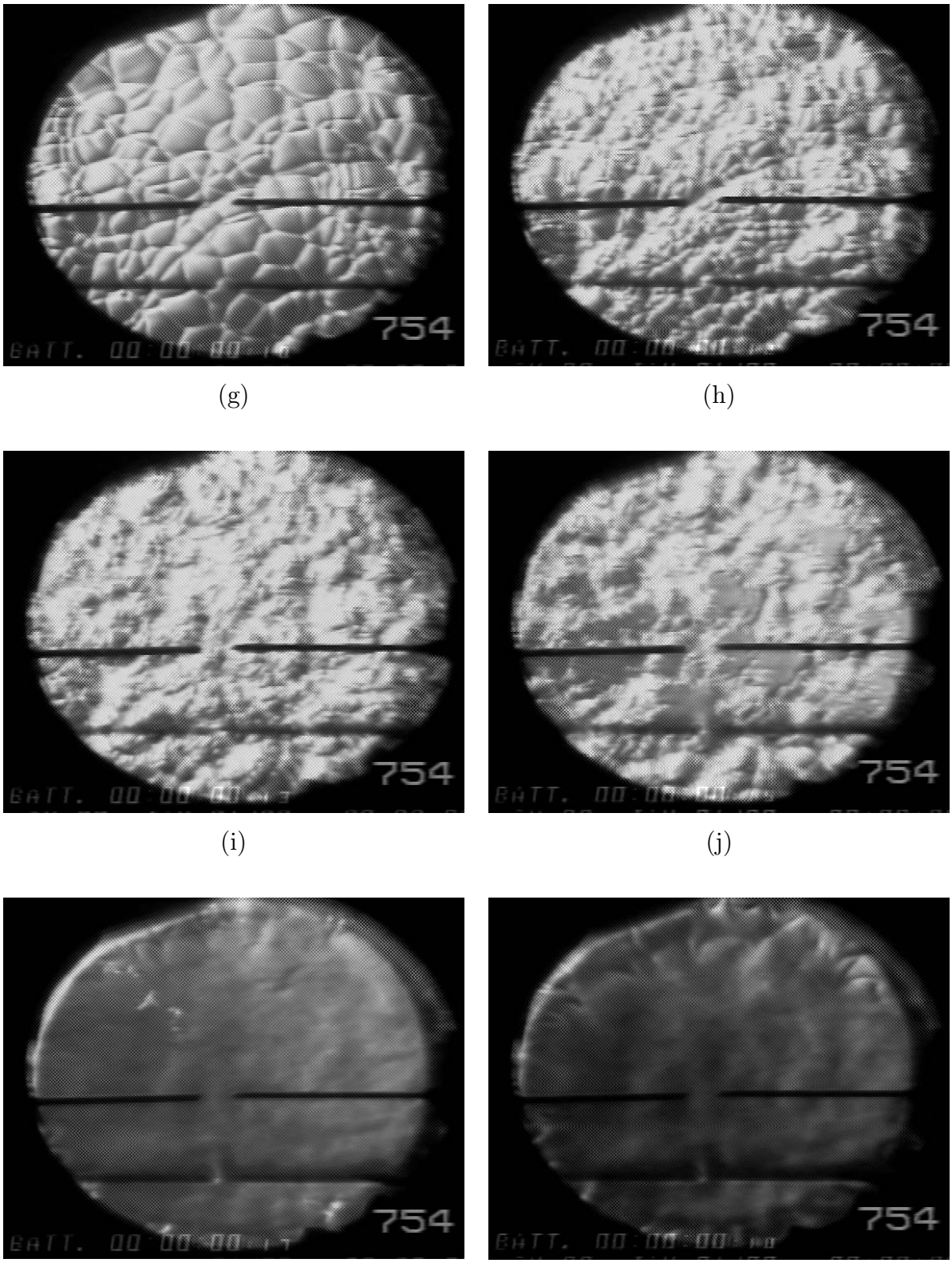

(g) (h)

(i) (j)

(k) (l)

Table 4: Video schlieren pictures of the ignition of a 1.4% H_2, 7% C_3H_8, 91.6% air-mixture in MiniConvol, the time interval between two frames is 17 ms.

can be seen. In picture (c) the flame has expanded uniformly. Small perturbations can be seen at the left and right edge of the picture and on the right side just underneath the gap of the electrodes. The next picture (d) is taken 51 ms after ignition. Both flame and perturbations have grown. Comparing the location of the upper edge of the flame to the location in the previous pictures, one can roughly estimate the burning speed. From the picture (e) on, the size of the flame is bigger than the size of the observation window. In the following pictures (f)-(l), it can be observed that as the perturbations increase, the flame surface is segmented into cells of various sizes and shapes and the flame becomes turbulent. 170 ms after ignition (picture k), the flame reaches the observation windows and the picture begins to darken due to condensation of water and soot particles.

The experiments with the Jet A simulant fuel showed that all cases (6%, 7% and 8.4% fuel) can be ignited with a hot filament. The energy discharged into the filament is about 15 Joules. The peak pressures in Convol for the three fuel concentrations showed large differences. The 8.4% and 7% fuel mixtures had peak pressures of 5.02 bar and 4.09 bar, respectively. The 6% fuel mixture had only a peak pressure of 1.24 bar. The 7% and 8.4% fuel-air mixtures can be ignited by a spark of 40 mJ energy. The 6% fuel-air mixture cannot be ignited with a spark of this energy. The combustion in this case could only be initiated by turning on the mixer and creating turbulent initial conditions.

5.2.3 Ignition Energy

The ignition energy measurement method is validated with hexane-air tests, and comparisons to the previous results from Shepherd et al. (1998). The following experiments are carried out in the 1.84 l IGGY combustion vessel. In every experiment, the amount of fuel is 6.9 ml, and corresponds to a fuel mass to volume ratio of 3 kg/m^3. This mass loading is close to the value in the center wing tank during flight TWA800.

Figure 50 shows ignition energy results from the report by Shepherd et al. (1998). In this figure, the ignition energy vs. the initial temperature is shown. It is obvious that the energy to ignite Jet A-air mixture significantly decreases with increasing initial temperature. The Jet A-air mixture could not be ignited at temperatures below 30°C with ignition energies of 100 Joules. The dashed line roughly marks the borderline between the flammable and the non-flammable areas. Left of the line Jet A-air mixtures are non-flammable; to the right, the mixtures are flammable. Due to the limited number of data points, the division between flammable and nonflammable is uncertain. Nevertheless, this gives a clear indication of how the ignition energy depends on the initial temper-

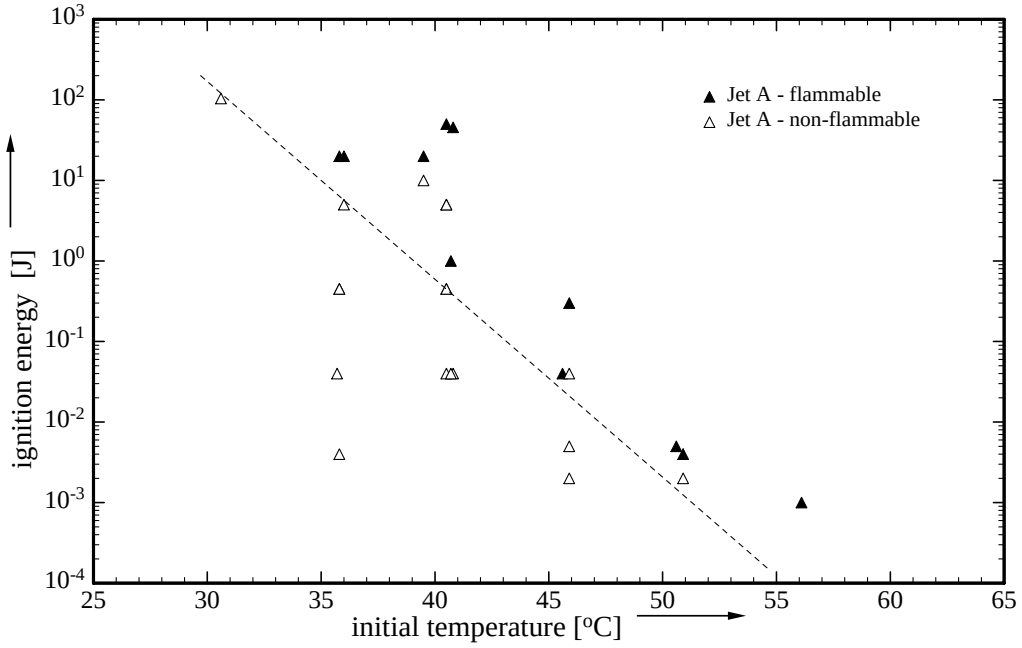

Figure 50: Measured ignition energy for Jet A-air mixtures at a fuel mass to volume ratio of 3 kg/m^3, initial pressure $p_0 = 0.585$ bar (Shepherd et al. (1998).

ature for these specific Jet A-air mixtures. These results can be compared directly to the results of this study, as the only difference is the type of fuel used . Shepherd et al. (1998) used fresh Jet A fuel from Los Angeles International Airport (LAX) and from El Monte Airport. In this study, three different weathered fuels are investigated. The exact description of these fuels follows in Chapter 5.2.4.

5.2.4 Fuel Weathering

Fuel in an airplane is exposed to a range of different conditions during flight. Both, pressure and temperature are functions of the flight altitude. The pressure within the Boeing 747-100 fuel tanks is slightly less than ambient when cruising since the vents are located in a low pressure region on the wing tips. The temperature of the fuel and consequently the vapor pressure in the tanks depends on the rate of heat transfer to the fuel from the surroundings. The fuel temperature is normally not measured in flight, but can be estimated from a heat transfer model or from flight tests. The effect of airplane operation on the fuel is one important aspect that has to be considered when trying to understand the conditions within the center wing tank of TWA800.

The experiments in Shepherd et al. (1998) were done with Jet A fuel from LAX. The fuel was stored at 20°C in a closed container to minimize the effects of fuel weathering. The weathered fuel samples #1, #4, and #5 were all taken from a Boeing 747 aircraft used in flight testing at JFK to simulate the conditions in TWA800. As described in Woodrow and Seiber (1997), the first sample (#1) was taken after filling the center wing tank with 50 gal of fuel brought from Athens, Greece for this purpose. Two initial (6h33min, 17500ft and 4h17min, 35000ft) flights were done to simulate the high altitude flight to JFK, layovers and taxiing. Sample #4 was taken was just before the TWA800 simulation flight. Fuel sample #5 was taken immediately after this test flight.

All three samples where thus exposed to fuel weathering which resulted in the loss of the high-volatility, low-molecular-weight components ($C_5 - C_8$) in the fuel. The low-molecular-weight components have the highest vapor pressures so that weathering results in lower vapor pressure.

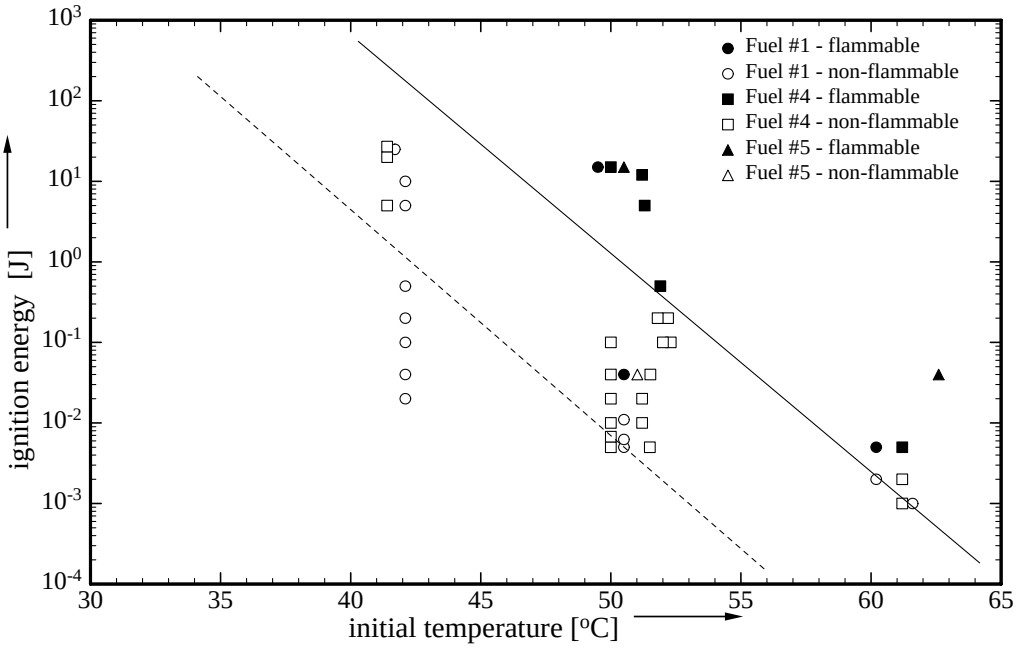

Figure 51: Flammability of different weathered Jet A fuels at initial pressure of $p_0 = 0.585$ bar as a function of ignition energy and initial temperature .

Figure 51 shows the ignition energy results for the weathered fuels. The line approximately separates the results in a non-flammable part to the left and a flammable part to the right of the line. Due to the limited number of data points, the dividing line is uncertain. However a qualitative trend can be seen. The dashed line represents the

flammability limit of fresh Jet A-air mixtures of Fig. 50. Comparing the two lines, it is obvious that the weathered fuels have a higher ignition energy than fresh fuel at the same initial temperature. Thus at the same temperature, it is much more difficult to ignite the weathered fuel than the regular fuel. As far as the different weathered fuels are concerned, comparisons with one another are difficult to draw, since the amount of data is limited. A strong dependence of the ignition energy on the initial temperature is observed. Note that the weathering experienced by these fuels is much more extensive than for the actual fuel on TWA800.

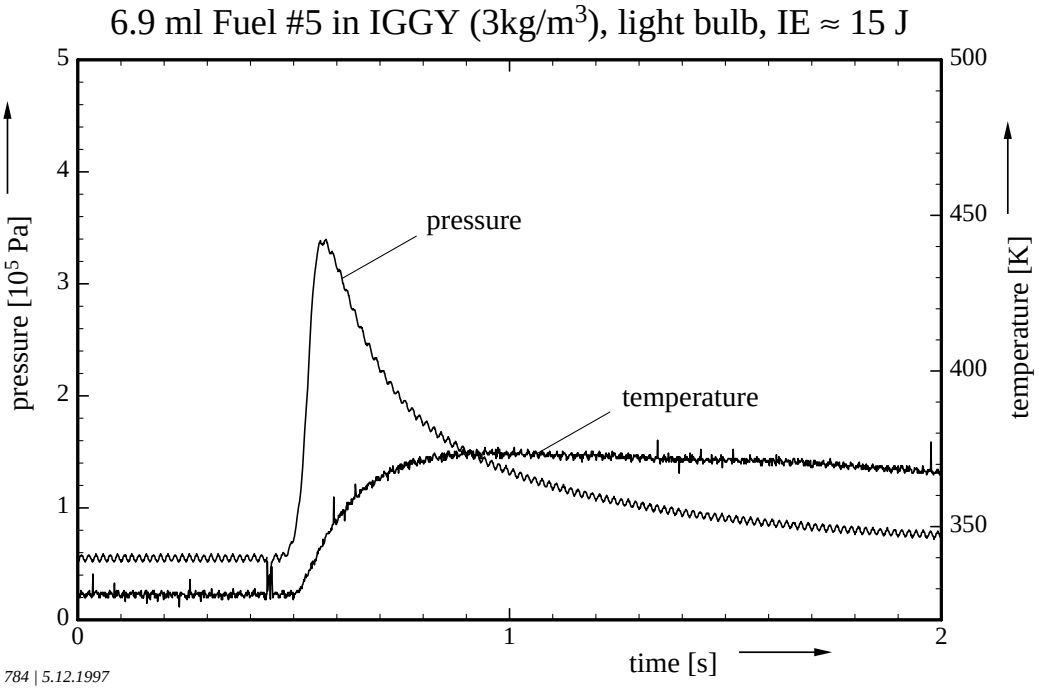

Figure 52: Pressure and temperature vs. time for 6.9 ml Jet A sample #5 with air at initial conditions of $p_0 = 58.5$ kPa, $T_0 = 323$ K, ignition energy = 15 J.

5.2.5 Hot Filament Ignition of Jet A

Tests were carried out to investigate the hot filament ignition of Jet A. Figure 52 shows pressure and temperature traces for 6.9 ml of fuel sample #5 with air at initial conditions of $p_0 = 58.5$ kPa, $T_0 = 323$ K. Table 5 shows the corresponding Schlieren video pictures. Again, the time delay between two frames is 17 ms. The window has a diameter of about 60 mm. In picture (a), the light bulb setup can be seen just before the ignition. The two pairs of electrodes (one behind the other one) belong to the spark ignition systems

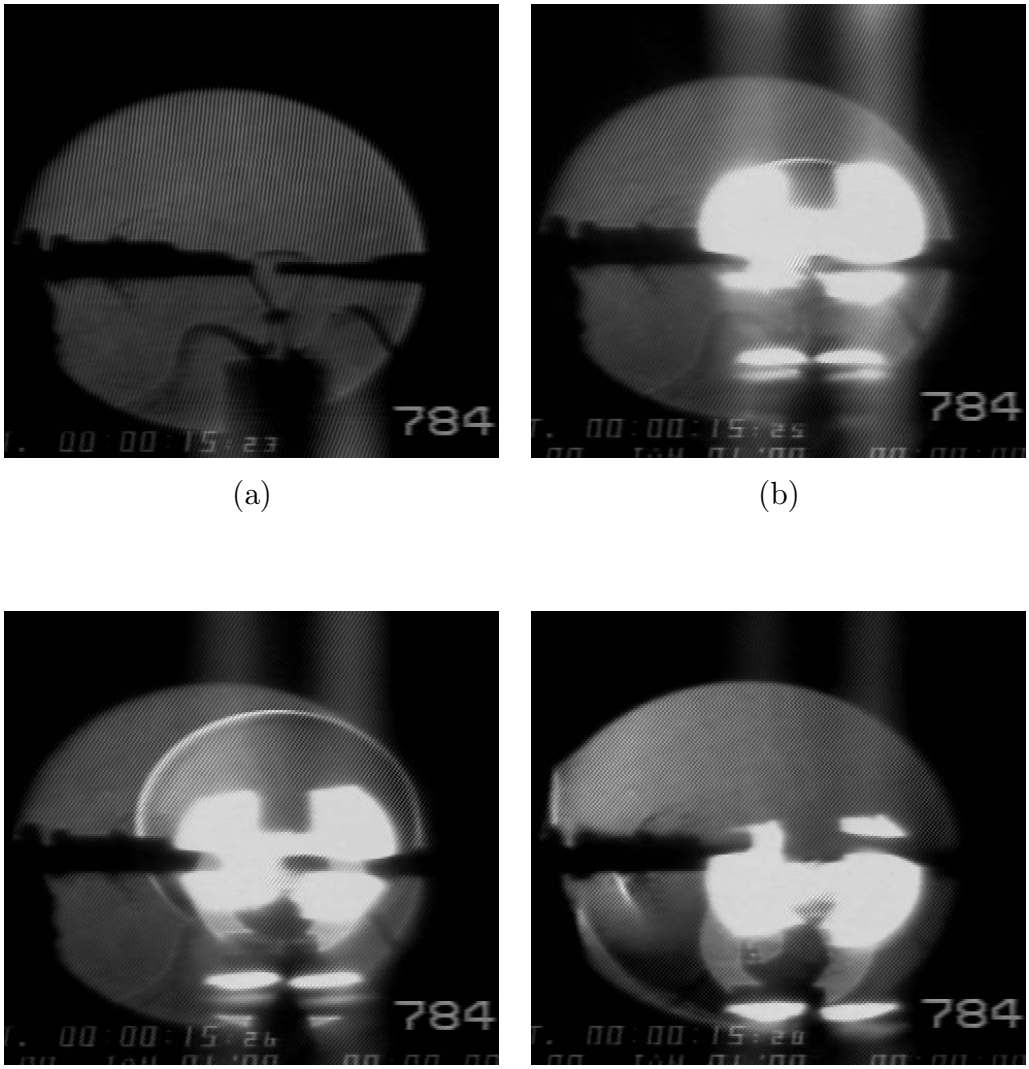

(a) (b)

(c) (d)

Table 5: Video schlieren pictures of the light bulb ignition of Jet A sample #5 in IGGY at initial conditions of $p_0 = 58.5$ kPa, $T_0 = 323$ K, the time interval between two frames is 17 ms.

of IGGY and Convol. They are not used in this experiment. In the lower part of the picture, the socket of the light bulb can be seen. The glass of the bulb is removed. Wires are soldered to the socket to allow connection to the electrical system. The point of ignition is the filament just above the spark gap. The second picture (b) is taken 17 ms after the ignition. The light emission causing the image to "bloom" results from the incandescence of the filament. In the upper middle part of the emission, a small part of the flame surface can be seen. The third picture (c) shows the nearly spherical flame

34 ms after ignition. The influence of buoyancy can be seen as the flame propagates slightly faster in the upward than in the downward direction. In the last picture (d), only a small part of the flame surface can be seen in the lower left corner.

6 Summary and Conclusions

A series of experiments were carried out to investigate combustion characteristics of hydrogen-, and hydrocarbon-air mixtures. The experiments were performed in four combustion vessels of different volume and shape. All vessels were instrumented with similar pressure and temperature gauges. Peak pressures, pressure traces and temperature traces were obtained during the combustion. The process inside the vessel was observed by a color Schlieren video system.

In the first part of the diploma-thesis, hydrogen-air mixtures with equivalence ratios from 0.235 to 0.95 and methane-, ethane-, propane-air mixtures with equivalence ratios from 0.65 to 1.0 were burned. Four combustion tanks with volumes of 1.84, 11.25, 407, and 1180 liters were used. The combustible mixtures were ignited by an electrical spark. The recorded pressure trace was used to determine the pressure time derivative. Based on the maximum pressure rise rate and the vessel volume, the pressure rise coefficient K_g was calculated. A nondimensional pressure rise coefficient, which respects geometrical differences of vessel and point of ignition, was introduced. Effective burning velocities were calculated from the pressure data using a spherical flame model. A dimensionless pressure rise coefficient K'_g was developed in order to minimize the dependence on the size of the vessel and fuel type.

$$K'_g \equiv \left(\frac{dp}{dt}\right)_{max} V^{\frac{1}{3}} \frac{1}{(\Delta p)_{max}} \frac{1}{S_{u,exp.}}.$$

This characteristic value was defined as a function of the characteristic length, the maximum pressure derivative, the laminar burning speed, and the maximum pressure increase during combustion. An attempt was made to improve this dimensionless pressure rise coefficient by introducing a correction factor based on simple models of spherical flames. The resulting modified pressure rise coefficient was defined as

$$K''_g \equiv \frac{1}{\left(\frac{p_{max}}{p_\circ}\right)^{\frac{1}{\gamma}}} \left(\frac{dp}{dt}\right)_{max} V^{\frac{1}{3}} \frac{1}{(\Delta p)_{max}} \frac{1}{S_{u,exp.}}.$$

Key findings of this part of the thesis are

1. The calculated pressure rise coefficients are in reasonable agreement with previous experiments from other authors, taking into consideration the differences in the

facilities and in the gas composition.

2. The calculated burning velocities are in reasonable agreement with literature values of the laminar burning speed. For large vessels and fast burning flames significant differences appear, but can be explained by the turbulent state of the flame.

3. The new-developed dimensionless pressure rise coefficient K'_g provides a means to roughly estimate the maximum pressure rise rate in closed-vessel combustion of hydrogen-air and selected hydrocarbon-air mixtures. Knowing the burning speed and the approximate peak pressure, the maximum pressure rise coefficient can be calculated by using a K'_g value in the proposed range 6 <K'_g < 16. The same can be done with the modified K''_g in the range of 2 <K''_g <4.5. Both parameters K'_g and K''_g can thus be used as an *a priori* construction parameter in vessel venting system design.

4. Further work on a universal pressure rise coefficient is recommended. The objective should be to refine the correlations by including buoyancy and energy loss effects. Investigations should be extended to other fuels and larger vessels.

The second part of the diploma-thesis is related to the studies at Caltech on the TWA800 accident. Jet A-air and simulant-air mixtures were investigated. The Jet A simulant consisted of a mixture of hydrogen and propane. Experiments were carried out for 6%, 7% and 8.4% simulant-air mixtures. The peak pressure and pressure trace for the 8.4% case were similar to that of a Jet A-air mixture at 50°C. The results of this diploma-thesis were used in preparing for field trials in a 1/4-scale simulation of the TWA800 central wing tank explosion. Ignition energy measurements were carried out for three different weathered fuels. These weathered fuels were similar to the fuel in the tanks of TWA800. Experiments were carried out in the heated 1.84 l combustion vessel. The chosen initial conditions of p = 585 mbar and T = 40-60°C correspond to the conditions in the center wing tank of flight TWA800 at an altitude of 13800 feet. Spark and filament ignition systems were used to initiate the combustion. The ignition energies of the weathered fuel-air mixtures were measured and compared to existing data of regular Jet A fuel-air mixtures.

Key findings of this part of the thesis are:

1. The 6%, 7%, and 8.4% simulant fuel-air mixtures are ignitable with a filament ignition system (15 J). Except for the 6% mixture, the mixtures can also be ignited

by an electrical spark of less energy than 4 mJ. For turbulent initial conditions, the 6% mixture is ignitable with an electrical spark.

2. The minimum ignition energies strongly depend on the initial temperature. The investigated weathered fuels cannot be ignited at 40°C with ignition energies below 27 Joules.

3. Weathering has a big influence on the minimum ignition energy of Jet A-air mixtures. Though the amount of available data does not allow precise quantification, a clear trend that ignition energies for the three investigated weathered fuel-air mixtures are higher than for fresh Jet A-air mixtures can be seen. The weathering experienced by these fuels was much more severe than for the fuel present in TWA800 at the time of the explosion.

References

Chatelier, H. L. and O. Boudouard (1898). Limits of Flammability in Gaseous Mixtures. *Bull. Soc. Chim. (Paris)* **19**, 483–488.

Egolfopoulos, F. N. and C. K. Law (1990). An Experimental and Computational Study of the Burning Rates of Ultra-Lean to Moderately-Rich $H_2/O_2/N_2$ Laminar Flames with Pressure Variations. In *Twenty-Third (International) Symposium on Combustion*. The Combustion Institute.

Gaydon, A. G. and H. G. Wolfhard (1970). *Flames: Their structure, radiation and temperature* (3 ed.). Chapman and Hall Ltd, London.

Hirschfelder, J. O., C. F. Curtiss, and R. B. Bird (1954). *Molecular Theory of Gases and Liquids*. Wiley, New York.

Kee, R. E., F. M. Roupley, and J. A. Miller (1989, September). Chemkin-II: A Fortran chemical kinetics package for the analysis of gas-phase chemical kinetics. Sandia Report SAND89-8009, SANDIA National Laboratories, Albuquerque, New Mexico.

Koroll, G. W., R. K. Kumar, and E. M. Bowles (1993). Burning Velocities of Hydrogen-Air Mixtures. *Combustion and Flame* **94**, 330–340.

Kuchta, J. (1985). Investigation of Fire and Explosion Accidents in the Chemical, Mining, and Fuel-Related Industries—A Manual. Bulletin 680, U.S. Bureau of Mines.

Kwon, S., L.-K. Tseng, and G. M. Faeth (1992). Laminar Burning Velocities and Instabilities. *Combustion and Flame* **90**, 230–246.

Lewis, B. and G. von Elbe (1961). Combustion, Flames and Explosions of Gases. Academic Press.

Mallard, E. and L. L. Chatelier (1883). Combustion des mélanges explosifs. Ann. Mines 4.

Metghalchi, M. and J. C. Keck (1980). Burning Velocity at high T and P. *Combustion and Flame* **80**, 143–154.

Nagy, J., E. Seiler, J. Conn, and H. Verakis (1971). Explosion development in closed vessels. Report of Investigations 7507, Bureau of Mines, U.S. Department of the Interior.

NFPA68 (1994). Guide for Venting of Deflagrations. Technical report, National Fire Protection Association, 1 Batterymarch Park, P.O. Box 9101, Quincy, MA, 02269-9101.

Raman, K. S. (1997). Laminar Burning Velocities of Lean Hydrogen-Air Mixtures. Explosion Dynamics Laboratory Report FM97-15, Graduate Aeronautical Laboratories, California Institute of Technology, Pasadena, CA.

Reynolds, W. C. (1986, January). *The Element Potential Method for Chemical Equilibrium Analysis: Implementation in the Interactive Program STANJAN* (3rd ed.). Stanford University, Dept. of Mechanical Engineering, Stanford, CA.

Ronney, P. D. (1985). Effect of gravity on laminar premixed gas combustion II: ignition and extinction phenomena. *Combustion and Flame 62*, 121–133.

Ross, M. C. and J. E. Shepherd (1996, July). Lean Combustion Characteristics of Hydrogen-Nitrous Oxide-Ammonia Mixtures in air. Part I. Explosion Dynamics Lab Report FM96-4, California Institute of Technology, Pasadena, CA.

Semenov, N. N. (1928). Z. Phys. Chem. **48**, 571.

Shepherd, J. E., J. C. Krok, and J. J. Lee (1997a, June). Jet A Explosion Experiments: Laboratory Testing. Explosion Dynamics Laboratory Report FM97-5, California Institute of Technology, Pasadena, CA.

Shepherd, J. E., J. C. Krok, and J. J. Lee (1997b, June). Jet A Explosions - Field Test Plan 1/4-Scale Experiments. Explosion Dynamics Laboratory Report FM97-17, Graduate Aeronautical Laboratories, California Institute of Technology, Pasadena, CA.

Shepherd, J. E., J. C. Krok, and J. J. Lee (1998, January). Spark Ignition Energy Measurements in Jet A. Explosion Dynamics Laboratory Report FM97-9, Graduate Aeronautical Laboratories, California Institute of Technology, Pasadena, CA.

Shepherd, J. E., J. C. Krok, J. J. Lee, L. L. Brown, R. T. Lynch, T. M. Samaras, and M. M. Birky (1998, February). Results of 1/4-Scale Experiments. Vapor Simulant And Liquid Jet A Tests. Explosion Dynamics Laboratory Report FM98-6, Graduate Aeronautical Laboratories, California Institute of Technology, Pasadena, CA. in collaboration with Applied Research Division, Inc. and NTSB.

Shepherd, J. E. and A. C. Ratzel (1985). Heat transfer resulting from premixed combustion. In C. K. Law, Y. Jaluria, W. W. Yuen, and K. Miyasaka (Eds.), *Heat Transfer in Fire and Combustion Systems*, Volume ASME HTD-45, pp. 191–201.

Woodrow, J. E. and J. E. Seiber (1997, November). The Laboratory Characterization of Jet Fuel Vapor under Simulated Flight Conditions. Final report, Center for Environmental Sciences and Engineering, University of Nevada, Reno, NV 89557-0187.

A Runlist: Pressure Analysis Experiments

No	Vessel	Gas Composition:	Φ	P_{AICC}	ν	P_{max}	$\Delta P / P_{AICC}$	$(dP/dt)_{max}$	$S_{u,eff}$	K_g	Re
				[bar]	[m^2/s]	[bar]		[bar/s]	[cm/s]	[bar m/ s]	
hj494	Hyjet	H2: 9.0 kPa, Air: 91.0 kPa	0.24	4.02	1.95E-05	3.41	0.152	4.6	18	4.8	9936
hj495	Hyjet	H2: 10.0 kPa, Air: 90.0 kPa	0.26	4.30	1.97E-05	3.78	0.122	9.8	33	10.3	17566
hj496	Hyjet	H2: 12.0 kPa, Air: 88.0 kPa	0.32	4.85	2.00E-05	4.30	0.113	16.6	42	17.6	22245
hj497	Hyjet	H2: 14.0 kPa, Air: 86.0 kPa	0.39	5.28	2.04E-05	4.68	0.114	30.3	118	32.0	61116
hj498	Hyjet	H2: 20.0 kPa, Air: 80.0 kPa	0.60	6.70	2.17E-05	6.32	0.057	118.5	258	125.3	125750
hj499	Hyjet	H2: 28.0 kPa, Air: 72.0 kPa	0.93	7.97	2.36E-05	7.52	0.068	311.6	528	329.3	236860
827	Convol	H2: 9.0 kPa, Air: 91.0 kPa	0.24	4.02	1.95E-05	3.34	0.169	13.0	18	9.6	6677
829	Convol	H2: 10.0 kPa, Air: 90.0 kPa	0.26	4.30	1.97E-05	3.91	0.092	17.1	28	12.7	10735
828	Convol	H2: 12.0 kPa, Air: 88.0 kPa	0.32	4.85	2.00E-05	4.51	0.069	35.9	41	26.6	15262
830	Convol	H2: 14.0 kPa, Air: 86.0 kPa	0.39	5.28	2.04E-05	4.91	0.076	53.0	107	39.3	38838
831	Convol	H2: 20.0 kPa, Air: 80.0 kPa	0.60	6.70	2.17E-05	6.51	0.028	238.6	211	176.8	72102
869	Convol	H2: 28.0 kPa, Air: 72.0 kPa	0.93	7.97	2.36E-05	7.60	0.047	373.5	371	276.8	92637
840	Miniconvol	H2: 9.0 kPa, Air: 91.0 kPa	0.24	4.02	1.95E-05	3.55	0.117	64.1	12	15.5	1346
839	Miniconvol	H2: 10.0 kPa, Air: 90.0 kPa	0.26	4.30	1.97E-05	4.17	0.031	64.7	21	14.5	2425
838	Miniconvol	H2: 12.0 kPa, Air: 88.0 kPa	0.32	4.85	2.00E-05	4.48	0.076	77.9	39	17.5	4330
841	Miniconvol	H2: 14.0 kPa, Air: 86.0 kPa	0.39	5.28	2.04E-05	5.07	0.040	141.9	68	31.8	7463
842	Miniconvol	H2: 20.0 kPa, Air: 80.0 kPa	0.60	6.70	2.17E-05	6.72	-0.003	324.0	158	72.6	16316
843	Miniconvol	H2: 28.0 kPa, Air: 72.0 kPa	0.93	7.97	2.36E-05	7.96	0.002	404.4	244	90.6	23202
826	IGGY	H2: 9.0 kPa, Air: 91.0 kPa	0.24	4.02	1.95E-05	3.02	0.249	37.7	10	4.6	661
822	IGGY	H2: 10.0 kPa, Air: 90.0 kPa	0.26	4.30	1.97E-05	3.93	0.069	69.7	19	8.5	1192
823	IGGY	H2: 12.0 kPa, Air: 88.0 kPa	0.32	4.85	2.00E-05	4.46	0.080	103.0	39	12.6	2404
824	IGGY	H2: 14.0 kPa, Air: 86.0 kPa	0.39	5.28	2.04E-05	5.21	0.013	202.8	68	24.9	4094
825	IGGY	H2: 20.0 kPa, Air: 80.0 kPa	0.60	6.70	2.17E-05	6.48	0.033	353.5	140	43.3	7946
863	IGGY	H2: 28.0 kPa, Air: 72.0 kPa	0.93	7.97	2.36E-05	7.66	0.039	389.9	175	47.8	9156

Table 6: Hydrogen-Air Mixtures

No	Vessel	Gas Composition:	Φ	P_{AICC}	ν	P_{max}	$\Delta P / P_{AICC}$	$(dP/dt)_{max}$	$S_{u,eff}$	K_g	Re
				[bar]	[m^2/s]	[bar]		[bar/s]	[cm/s]	[bar m/ s]	
hj505	Hyjet	CH4: 5.93 kPa, Air: 94.07 kPa	0.60	6.84	1.87E-05	4.78	0.301	4	15	4	8661
hj507	Hyjet	CH4: 6.85 kPa, Air: 93.15 kPa	0.70	7.50	1.88E-05	5.58	0.256	9	32	10	18158
hj508	Hyjet	CH4: 7.76 kPa, Air: 92.24 kPa	0.80	8.09	1.89E-05	6.31	0.220	21	49	22	27238
hj509	Hyjet	CH4: 9.03 kPa, Air: 90.97 kPa	0.94	8.73	1.90E-05	7.26	0.169	33	54	35	30177
hj510	Hyjet	CH4: 9.51 kPa, Air: 90.49 kPa	1.00	8.90	1.91E-05	7.35	0.174	38	64	40	35657
834	Convol	CH4: 5.93 kPa, Air: 94.07 kPa	0.60	6.84	1.87E-05	4.63	0.323	4	18	3	7108
805	Convol	CH4: 6.85 kPa, Air: 93.15 kPa	0.70	7.50	1.88E-05	5.91	0.212	14	27	10	10662
804	Convol	CH4: 7.76 kPa, Air: 92.24 kPa	0.80	8.09	1.89E-05	6.92	0.145	29	35	22	13669
803	Convol	CH4: 9.03 kPa, Air: 90.97 kPa	0.94	8.73	1.90E-05	7.64	0.125	52	50	38	19316
835	Convol	CH4: 9.51 kPa, Air: 90.49 kPa	1.00	8.90	1.91E-05	7.96	0.105	58	54	43	20796
847	Miniconvol	CH4: 5.93 kPa, Air: 94.07 kPa	0.60	6.84	1.87E-05	4.46	0.348	55	14	12	1641
844	Miniconvol	CH4: 6.85 kPa, Air: 93.15 kPa	0.70	7.50	1.88E-05	6.55	0.127	62	22	14	2613
845	Miniconvol	CH4: 7.76 kPa, Air: 92.24 kPa	0.80	8.09	1.89E-05	7.14	0.118	97	30	22	3570
846	Miniconvol	CH4: 9.03 kPa, Air: 90.97 kPa	0.94	8.73	1.90E-05	7.92	0.093	157	42	35	4940
849	Miniconvol	CH4: 9.51 kPa, Air: 90.49 kPa	1.00	8.90	1.91E-05	8.18	0.081	172	46	39	5402
861	IGGY	CH4: 5.93 kPa, Air: 94.07 kPa	0.60	6.84	1.87E-05	4.29	0.373	79	15	10	1018
808	IGGY	CH4: 6.85 kPa, Air: 93.15 kPa	0.70	7.50	1.88E-05	5.93	0.210	93	26	11	1686
809	IGGY	CH4: 7.76 kPa, Air: 92.24 kPa	0.80	8.09	1.89E-05	6.64	0.179	153	37	19	2421
810	IGGY	CH4: 9.03 kPa, Air: 90.97 kPa	0.94	8.73	1.90E-05	7.27	0.167	221	47	27	3014
860	IGGY	CH4: 9.51 kPa, Air: 90.49 kPa	1.00	8.90	1.91E-05	7.82	0.121	249	48	30	3095

Table 7: Methane-Air Mixtures

No	Vessel	Gas Composition:	Φ	P_{AICC}	ν	P_{max}	$\Delta P / P_{AICC}$	$(dP/dt)_{max}$	$S_{u,eff}$	K_g	Re
				[bar]	[m^2/s]	[bar]		[bar/s]	[cm/s]	[bar m/ s]	
hj500	Hyjet	C2H6: 3.75 kPa, Air: 96.25 kPa	0.69	7.44	1.81E-05	6.00	0.194	14	28	15	16355
hj501	Hyjet	C2H6: 4.03 kPa, Air: 95.97 kPa	0.74	7.79	1.81E-05	6.22	0.202	19	36	20	20879
hj502	Hyjet	C2H6: 4.58 kPa, Air: 95.42 kPa	0.85	8.42	1.81E-05	7.24	0.140	34	40	36	23219
hj503	Hyjet	C2H6: 5.12 kPa, Air: 94.88 kPa	0.95	8.92	1.81E-05	8.03	0.100	55	47	58	27182
hj504	Hyjet	C2H6: 5.66 kPa, Air: 94.34 kPa	1.00	9.29	1.81E-05	8.54	0.083	78	57	82	33266
881	Convol	C2H6: 3.75 kPa, Air: 96.25 kPa	0.69	7.44	1.81E-05	6.28	0.156	21	30	16	12365
880	Convol	C2H6: 4.03 kPa, Air: 95.97 kPa	0.74	7.79	1.81E-05	6.76	0.133	31	35	23	14465
879	Convol	C2H6: 4.58 kPa, Air: 95.42 kPa	0.85	8.42	1.81E-05	7.60	0.097	52	43	39	17727
882	Convol	C2H6: 5.12 kPa, Air: 94.88 kPa	0.95	8.92	1.81E-05	8.16	0.085	71	55	53	22579
878	Convol	C2H6: 5.66 kPa, Air: 94.34 kPa	1.00	9.29	1.81E-05	8.65	0.069	89	63	66	25664
877	Miniconvol	C2H6: 3.75 kPa, Air: 96.25 kPa	0.69	7.44	1.81E-05	6.62	0.111	66	22	15	2753
872	Miniconvol	C2H6: 4.03 kPa, Air: 95.97 kPa	0.74	7.79	1.81E-05	7.06	0.094	90	27	20	3379
873	Miniconvol	C2H6: 4.58 kPa, Air: 95.42 kPa	0.85	8.42	1.81E-05	7.75	0.079	139	32	31	3958
874	Miniconvol	C2H6: 5.12 kPa, Air: 94.88 kPa	0.95	8.92	1.81E-05	8.28	0.072	202	47	45	5762
875	Miniconvol	C2H6: 5.66 kPa, Air: 94.34 kPa	1.00	9.29	1.81E-05	8.81	0.052	249	50	56	6180

Table 8: Ethane-Air Mixtures

No	Vessel	Gas Composition:	Φ	P_{AICC}	ν	P_{max}	$\Delta P / P_{AICC}$	$(dP/dt)_{max}$	$S_{u,eff}$	K_g	Re
				[bar]	[m^2/s]	[bar]		[bar/s]	[cm/s]	[bar m/ s]	
hj513	Hyjet	C3H8: 3.05 kPa, Air: 96.95 kPa	0.75	8.21	1.77E-05	7.10	0.136	27	41	29	24486
hj511	Hyjet	C3H8: 3.35 kPa, Air: 96.65 kPa	0.83	8.67	1.77E-05	7.55	0.129	38	50	40	29728
hj472	Hyjet	C3H8: 3.47 kPa, Air: 96.53 kPa	0.86	8.84	1.77E-05	7.65	0.134	40	55	42	32778
hj512	Hyjet	C3H8: 3.84 kPa, Air: 96.16 kPa	0.95	9.26	1.76E-05	8.44	0.089	67	59	71	35644
865	Convol	C3H8: 3.05 kPa, Air: 96.95 kPa	0.75	8.21	1.77E-05	7.00	0.148	31	33	23	13822
868	Convol	C3H8: 3.35 kPa, Air: 96.65 kPa	0.83	8.67	1.77E-05	7.66	0.117	47	43	34	17913
867	Convol	C3H8: 3.47 kPa, Air: 96.53 kPa	0.86	8.84	1.77E-05	7.82	0.115	52	49	39	20466
866	Convol	C3H8: 3.84 kPa, Air: 96.16 kPa	0.95	9.26	1.76E-05	8.43	0.090	71	50	52	21131
856	Miniconvol	C3H8: 3.05 kPa, Air: 96.95 kPa	0.75	8.21	1.77E-05	6.25	0.239	90	18	20	2234
853	Miniconvol	C3H8: 3.35 kPa, Air: 96.65 kPa	0.83	8.67	1.77E-05	7.39	0.148	103	31	23	3986
854	Miniconvol	C3H8: 3.47 kPa, Air: 96.53 kPa	0.86	8.84	1.77E-05	7.70	0.128	122	37	27	4660
855	Miniconvol	C3H8: 3.84 kPa, Air: 96.16 kPa	0.95	9.26	1.76E-05	8.29	0.105	178	45	40	5764
857	IGGY	C3H8: 3.05 kPa, Air: 96.95 kPa	0.75	8.21	1.77E-05	6.76	0.177	136	28	17	1946
819	IGGY	C3H8: 3.35kPa, Air: 96.65 kPa	0.83	8.67	1.77E-05	7.63	0.120	233	41	29	2826
864	IGGY	C3H8: 3.47kPa, Air: 96.53 kPa	0.86	8.84	1.77E-05	7.69	0.130	253	41	31	2853
858	IGGY	C3H8: 3.84 kPa, Air: 96.16 kPa	0.95	9.26	1.76E-05	8.22	0.113	350	47	43	3292

Table 9: Propane-Air Mixtures

B Runlist: Ignition Energy Experiments

No	Date	Vessel	Fuel	P_o	T_o	E	P_{max}	P_{final}	Ignition	GO	NOGO	Comments
				[kPa]	[C]	[J}	[bar]	[kPa]				
754	11/13/97	MCV	1.4%C3H8, 7%H2, 91.6%air	84.2	21.9	8	4.88	76.1	S(3.3mm)	X		S=Spark
755	11/13/97	MCV	1.4%C3H8, 7%H2, 91.6%air	83.4	21.8	0.04	5.33	75.3	S(3.3mm)	X		
757	11/16/97	MCV	1.4%C3H8, 7%H2, 91.6%air	83.4	22.4	15	3.95	78	LB	X		LB=Light Bulb
758	11/16/97	MCV	1.4%C3H8, 7%H2, 91.6%air	83.4	22.1	15	4.17	77.1	LB	X		
759	11/17/97	MCV	1.4%C3H8, 7%H2, 91.6%air	83.4	22.5		4.53	74.9		X		
760	11/17/97	MCV	1.4%C3H8, 7%H2, 91.6%air	83.4	22.6		4.86	74.3		X		
766	11/20/97	IGGY	Jet A #4, 6.75cc	58.5	50	0.004	3.8	64.5	S(2.0mm)	X		NOGO gap=3mm
767	11/21/97	IGGY	Jet A #4, 6.9cc	58.5	50	0.005			S(2.5mm)		X	
767	11/21/97	IGGY	Jet A #4, 6.9cc	58.5	50	0.00675					X	
767	11/21/97	IGGY	Jet A #4, 6.9cc	58.5	50	0.01					X	
767	11/21/97	IGGY	Jet A #4, 6.9cc	58.5	50	0.02					X	low voltage
767	11/21/97	IGGY	Jet A #4, 6.9cc	58.5	50	0.04					X	
767	11/21/97	IGGY	Jet A #4, 6.9cc	58.5	50	0.1					X	
767	11/21/97	IGGY	Jet A #4, 6.9cc	58.5	50	0.5625					X	
768	11/21/97	IGGY	Hexane, 22cc	98.5	26	0.001			S(3.3mm)		X	
768	11/21/97	IGGY	Hexane, 22cc	98.5	26	0.015			S(3.3mm)		X	
768	11/21/97	IGGY	Hexane, 22cc	98.5	26	0.015			S(2.5mm)		X	
768	11/21/97	IGGY	Hexane, 22cc	98.5	26	0.015	7.8	93.5	S(2.0mm)	X		
769	11/25/97	CV	1.4%C3H8, 7%H2, 91.6%air	83.4	22.5	15	5.02	73.9	LB	X		
770	11/25/97	CV	1%C3H8, 5%H2, 94%air	83.4	21.8	15	1.24	82.2	LB	X		
771	11/25/97	CV	1.2%C3H8, 5.8%H2, 93%air	83.4	21.4	15	4.09	76.4	LB	X		
772	11/25/97	CV	1%C3H8, 5%H2, 94%air	83.4	22.5		3		S(3.3mm)	X		GO with mixer
773	11/25/97	CV	1%C3H8, 5%H2, 94%air	83.4	25.4		1.11				X	
773	11/25/97	CV	1%C3H8, 5%H2, 94%air	83.4	25.4		3.33	77.8		X		GO with mixer
774	11/25/97	CV	1.4%C3H8, 7%H2, 91.6%air	83.4	25.6		4.94	74.8	S(3.3mm)	X		
775	11/25/97	CV	1.2%C3H8, 5.8%H2, 93%air	83.4	25.4		3.98	76.7	S(3.3mm)	X		
776	11/26/97	IGGY	El Monte Jet A, 200cc	58.5	50	0.04	4.2		S(2.0mm)		X	T-11 used
776	11/26/97	IGGY	El Monte Jet A, 200cc	58.5	50	0.04	4.2		S(3.0mm)	X		T-11 used
777	11/26/97	IGGY	El Monte Jet A, 200cc	58.5	50	0.04	4.34	60	S(3.5mm)	X		
779	11/26/97	IGGY	El Monte Jet A, 200cc	58.5	50	15	4.18	60	LB	X		
782	11/30/97	IGGY	Jet A #1, 6.9cc	58.5	50	15	4.2		LB	X		Hand triggered
783	11/30/97	IGGY	Jet A #4, 6.9cc	58.5	50	15	3.4		LB	X		Hand triggered
784	11/30/97	IGGY	Jet A #5, 6.9cc	58.5	50	15	3.4		LB	X		Hand triggered
785	11/30/97	IGGY	Jet A #5, 6.9cc	58.5	50	0.005			S(3.3mm)		X	Hand triggered
785	11/30/97	IGGY	Jet A #5, 6.9cc	58.5	50	0.00625			S(3.3mm)		X	Hand triggered
785	11/30/97	IGGY	Jet A #5, 6.9cc	58.5	50	0.00625			S(4mm)		X	Hand triggered
785	11/30/97	IGGY	Jet A #5, 6.9cc	58.5	50	0.011			S(4.5mm)		X	Hand triggered
785	11/30/97	IGGY	Jet A #5, 6.9cc	58.5	50	0.04	4.2		S(4.5mm)	X		TM-11 used
788	12/1/97	CV	1.3%C3H8, 5.2%C3H8, 93.5% air	83.5	22.5		3.53	77.1	S	X		6.5% fuel

Table 10: Ignition Energy Experiments, part 1

No	Date	Vessel	Fuel	P_o	T_o	E	P_{max}	Ignition	GO	NOGO	Comments
				[kPa]	[C]	[J}	[bar]				
789	12/1/97	IGGY	Jet A #4, 6.9cc	58.5	40	15	< 0.8			X UPF	Hand triggered
790	12/1/97	IGGY	Jet A #5, 6.9cc	58.5	51.2	0.04	N/A	S (3.5mm)		X	
790	12/1/97	IGGY	Jet A #5, 6.9cc	58.5	62.6	0.04	N/A	S (3.5mm)	X		no p- and T-diagr.
791	12/2/97	IGGY	Jet A #4, 6.9cc	58.5	61.2	0.001	N/A	S (3.5mm)		X	
791	12/2/97	IGGY	Jet A #4, 6.9cc	58.5	61.2	0.002	N/A	S (3.5mm)		X	
791	12/2/97	IGGY	Jet A #4, 6.9cc	58.5	61.2	0.005	4.58	S (3.5mm)	X		
792	12/2/97	IGGY	Jet A #4, 6.9cc	58.5	51.5	0.005		S (3.5mm)		X	
792	12/2/97	IGGY	Jet A #4, 6.9cc	58.5	51.5	0.01		S (3.5mm)		X	
792	12/2/97	IGGY	Jet A #4, 6.9cc	58.5	51.5	0.02		S (3.5mm)		X	
792	12/2/97	IGGY	Jet A #4, 6.9cc	58.5	51.2	0.04		S (3.5mm)		X	
792	12/2/97	IGGY	Jet A #4, 6.9cc	58.5	51.2	0.04		S (4.5mm)		X	
792	12/2/97	IGGY	Jet A #4, 6.9cc	58.5	51.2	ca.12	N/A	S (4.5mm)	X		uncontr. ignit.
793	12/2/97	IGGY	Jet A #4, 6.9cc	58.5	41.4	5	N/A	S (4.5mm)		X	small UPF
793	12/2/97	IGGY	Jet A #4, 6.9cc	58.5	41.4	20	N/A	S (4.5mm)		X	
793	12/2/97	IGGY	Jet A #4, 6.9cc	58.5	41.4	20	N/A	S (5.5mm)		X	
793	12/2/97	IGGY	Jet A #4, 6.9cc	58.5	41.4	20	N/A	S (7.0mm)		X	
793	12/2/97	IGGY	Jet A #4, 6.9cc	58.5	41.4	27	N/A	S (10mm)		X	
794	12/2/97	IGGY	Jet A #4, 6.9cc	58.5	51.3	5	3.76	S (3.5mm)	X		
795	12/3/97	IGGY	Jet A #1, 6.9cc	58.5	42.1	0.01	N/A	S (3.5mm)		X	no spark
795	12/3/97	IGGY	Jet A #1, 6.9cc	58.5	42.1	0.02	N/A	S (3.5mm)		X	
795	12/3/97	IGGY	Jet A #1, 6.9cc	58.5	42.1	0.04	N/A	S (3.5mm)		X	
795	12/3/97	IGGY	Jet A #1, 6.9cc	58.5	42.1	0.1	N/A	S (3.5mm)		X	no spark
795	12/3/97	IGGY	Jet A #1, 6.9cc	58.5	42.1	0.2	N/A	S (3.5mm)		X	
795	12/3/97	IGGY	Jet A #1, 6.9cc	58.5	42.1	0.5	N/A	S (3.5mm)		X	
795	12/3/97	IGGY	Jet A #1, 6.9cc	58.5	42.1	5	N/A	S (3.5mm)		X	spark from side
795	12/3/97	IGGY	Jet A #1, 6.9cc	58.5	42.1	10	N/A	S (3.5mm)		X	
795	12/3/97	IGGY	Jet A #1, 6.9cc	58.5	41.7	25	N/A	S (7.0mm)		X	spark when adjust.
796	12/3/97	IGGY	Jet A #4, 6.9cc	58.5	52.5	0.1	N/A	S (3.5mm)		X	no spark
796	12/3/97	IGGY	Jet A #4, 6.9cc	58.5	52.2	0.2	N/A	S (3.5mm)			uncontr ignit.
797	12/3/97	IGGY	Jet A #4, 6.9cc	58.5	52.1	0.1	N/A	S (3.5mm)		X	no spark
797	12/3/97	IGGY	Jet A #4, 6.9cc	58.5	51.8	0.2	N/A	S (3.5mm)		X	
797	12/3/97	IGGY	Jet A #4, 6.9cc	58.5	51.9	0.5	3.86	S (7.0mm)	X		delay : 0.8sec
798	12/4/97	IGGY	Jet A #1, 6.9cc	58.5	61.6	0.001	N/A	S (3.5mm)		X	no spark
798	12/4/97	IGGY	Jet A #1, 6.9cc	58.5	60.2	0.002	N/A	S (3.5mm)		X	no spark
798	12/4/97	IGGY	Jet A #1, 6.9cc	58.5	60.2	0.005	4.52	S (3.5mm)	X		
799	12/4/97	IGGY	Jet A #1, 6.9cc	58.5	41.1	15	N/A	LB		X	UPF

Table 11: Ignition Energy Experiments, part 2